Title
Probing the Cosmic Web with Fast Radio Bursts

Author
Hassan Satish, Sunil Simha

Publication Date
2024

UNIVERSITY OF CALIFORNIA
SANTA CRUZ

PROBING THE COSMIC WEB WITH FAST RADIO BURSTS

A dissertation submitted in partial satisfaction of the
requirements for the degree of

DOCTOR OF PHILOSOPHY

in

ASTRONOMY AND ASTROPHYISCS

by

H. S. Sunil Simha

June 2024

The Dissertation of H. S. Sunil Simha
is approved:

Professor Brant Robertson, Chair

Professor J. Xavier Prochaska

Professor Constance Rockosi

Professor Khee-Gan Lee

Peter Biehl
Vice Provost and Dean of Graduate Studies

Table of Contents

List of Figures

List of Tables

Abstract

Probing the Cosmic Web with Fast Radio Bursts

by

H. S. Sunil Simha

Fast Radio Bursts (FRBs) are enigmatic, millisecond-duration extragalactic transients discovered only in the late 2000s. Though the exact nature of their origin is unknown, their extremely short-duration emission endows several unique qualities that make them uniquely useful as probes of foreground matter. Chief among such properties is their dispersion. As FRB light propagates through plasma, their radio frequencies are dispersed, resulting in higher frequencies arriving before lower frequencies at Earth. The dispersion is directly proportional to the line-of-sight integral of the electron density weighted by the cosmological scale factor, i.e., the Dispersion Measure (DM). The DM of each FRB can be measured extremely precisely ($\sim 1\%$) by radio telescopes during detection. Thus, FRB DMs precisely probe foreground ionized matter, especially the warm, hot intergalactic medium (WHIM), a previously difficult-to-detect phase of matter. In this manuscript, I first describe the detection of the so-called "missing" baryons, a long-standing cosmological conundrum with FRBs. Then, I present work I have led that establishes the technique of foreground mapping, i.e., leveraging optical observations of foreground galaxies to constrain DM contributions from intervening foreground structures such as halos and cosmic-web filaments. Finally, I present the results of the FLIMFLAM survey, a statistical treatment of the foreground observation of several FRB sightlines to produce novel constraints on gas fractions within halos and

filaments. I conclude with prospects for a FLIMFLAM-like analysis with a significantly larger sample of FRB sightlines expected to be detected within the next three years.

To my partner, Prajna Hebbar,

for her support and love

and

To my parents,

for their encouragement and faith in me.

Acknowledgments

Family and friends

I want first to acknowledge the most amazing individuals in my life: my parents. They have constantly motivated and encouraged me to pursue science from a young age, making me who I am today. Next, I would like to thank Usha Keshav (Chikki, my aunt) for being the first person to teach me astrophysics. I still remember her reading to me from a Dorling-Kindersley Atlas about the evolution of the sun when I was 4. It made a lasting impression and has no doubt subconsciously guided my decision to choose astronomy as my field of study. I want to thank my partner, Prajna Hebbar, for her unwavering support, understanding, and patience. Her presence has been a constant source of inspiration and positivity. I am genuinely grateful to have met her during my research journey in Santa Cruz. I would also like to thank all my friends in the UCSC Department of Astronomy, especially the graduate students and the postdoctoral researchers who made me feel like I belonged. Grad school would have been difficult without the Grad retreats, Social Hours, video game nights, Secret Santa gift exchanges, board game sessions, and, most importantly, lunches in front of the CfAO. I would also like to acknowledge all the Santa Cruz Chess Club members, especially Ryan, Aaron, and Jesse, who made me look forward to Saturdays. Last but not least, Fifi, my housemate's cat, for the fuzzy warmth and silent company at night.

Scientific advisors and collaborators

I express my deepest gratitude to my advisor, Prof. J. Xavier Prochaska (X), for his invaluable guidance, support, and mentorship throughout my Ph.D. journey.

His expertise and encouragement have been instrumental in shaping my research and academic growth. I would not have been in UCSC were it not for X taking me under his wing as an undergraduate summer intern in 2017. Also vital to nurturing my interest in astronomy were Prof. Raghunathan Srianand and Prof. Sriramkumar, who advised me during my undergraduate studies and my master's thesis and connected me with X.

Next, I would like to thank Prof. Constance Rockosi for guiding me through a rewarding instrumentation research project and for being an incredibly patient mentor. In addition, I would like to acknowledge my absolute pleasure in working with the engineers and project staff at UCO/Lick Laboratories on the LRIS and KCRM detector projects: Dale Sandford, Maureen Savage, Jerry Cabak, Steve Allen, and William Deich. Additional thanks to Dr. Sherry Yeh and Dr. Percy Gomez for the opportunity to do follow-up instrumentation work on LRIS as a Keck Visiting Scholar while enjoying the beautiful Big Island of Hawaii.

I want to thank Prof. Khee-Gan Lee for allowing me to be part of the FLIMFLAM collaboration and work on cosmic baryon analysis using FRBs. I also want to thank him for the opportunity to visit Japan and work as a JSPS research scholar. I want to acknowledge the support of the FLIMFLAM collaboration, especially Dr. Ilya Khrikin, Yuxin Huang, and Chenze Dong, who have been outstanding scientific collaborators and friends.

I want to thank all the present and past members of the F^4 collaboration for being an exceptionally supportive and fun group of people to work with. Studying FRBs would not have been as enjoyable without them. I especially want to thank Prof. Nicolas Tejos for inviting me to work with him in Chile, Prof. Wen-Fai Fong for supporting me through rough patches in graduate school, and Dr. Charlie Kilpatrick for being a true imaging expert I could always rely on.

I would also like to thank members of the CRAFT collaboration, who were an extremely friendly research group and the most important source of localized FRBs: the foundation on which my thesis was built.

Institutions

I want to thank UCSC and its Department of Astronomy and Astrophysics for accepting me as a graduate student and providing the environment for my growth as a researcher.

Lastly, I thank the W. M. Keck Observatory, the Siding Spring Observatory, and the Gemini Observatory for providing the telescope time to enable my research goals. Special thanks to all my support astronomers and the ground crew at these facilities, without whom life would be impossible as an observational astronomer.

Published Material

The text of this dissertation includes reprints of the following published material led by Simha, with the permission of the listed coauthors.

Chapter 2 was published in the Astrophysical Journal as Simha et al. (2020). I was responsible for producing the work contained within the text, writing the text, and creating the figures, with Xavier Prochaska supervising the work that provides the basis for this dissertation. Joseph Burchett and Oskar Elek contributed substantially by producing the cosmic-web density used in this work with their Monte Carlo Physarum Machine (MCPM) model. Members of the CRAFT collaboration listed as coauthors provided the FRB localization and measurements that allowed the analysis to be performed for the FRB sightline, and the members of the F^4 collaboration contributed to optical observing and obtaining the telescope time required for said observations. All coauthors provided substantial comments on the content of the manuscript.

Chapter 3 was published in the Astrophysical Journal as Simha et al. (2021). I was responsible for producing the work contained within the text, writing the text, and creating the figures, with Xavier Prochaska supervising the work that provides the basis for this dissertation. Nicolas Tejos obtained the MUSE observation key for the analysis presented. Sebastian Cantalupo provided access to the CubEx reduction package for the MUSE datacube. Members of the CRAFT collaboration listed as coauthors provided the FRB localization that allowed the analysis to be performed for the FRB sightline, and the members of the F^4 collaboration contributed to optical observing and obtaining the telescope time required for said observations. All coauthors provided substantial comments on the content of the manuscript.

Chapter 5 was published in the Astrophysical Journal as Simha et al. (2023). I was responsible for producing the work contained within the text, writing the text, and creating the figures, with Xavier Prochaska supervising the work that provides the basis for this dissertation. Khee-Gan Lee, Ilya Khrykin, and Yuxin Huang obtained the AAOmega observations and redshifts key for the analysis presented. Members of the CRAFT collaboration listed as coauthors provided the FRB localization that allowed the analysis to be performed for the FRB sightline, and the members of the FLIMFLAM collaboration contributed to optical observing and obtaining the telescope time required for said observations. All coauthors provided substantial comments on the content of the manuscript.

Sections 6.1 through 6.5 of chapter 6 are paraphrased or reproduced from the work of Khrykin et al. (2024b), which was published in the Astrophysical Journal and from Huang et al. (2024, in prep.) which will be submitted for publication in the following months. I am a coauthor on both works and was responsible for the Keck multi-object spectroscopic observations, data reduction, and analysis of $\mathrm{DM}_{\mathrm{halos}}$. I have also contributed significantly to the texts and figures of both manuscripts. Ilya Khrykin and Yuxin Huang led the study and produced the main body of text and figures. Metin Ata performed the cosmic web density reconstructions using ARGO. Khee-Gan Lee supervised the work, conceived the analysis, and contributed significantly to AAOmega observations. Members of the CRAFT collaboration listed as coauthors provided the FRB localization that allowed the study to be performed for the FRB sightline, and the members of the FLIMFLAM collaboration contributed to optical observing and obtaining the telescope time required for said observations. All coauthors provided substantial comments on the content of the manuscript.

Chapter 1

Introduction: A brief review of FRBs as probes of the Cosmic Web

1.1 The Missing Baryon Problem

Various experiments in the last 25 years have measured anisotropies in the temperature of the Cosmic Microwave Background (CMB) and have effectively weighed the contents of the universe (Mather et al., 1994; Hinshaw et al., 1996; Bennett et al., 2013; Planck Collaboration et al., 2014, 2016a, 2020). Roughly 95% of the energy density budget of the universe is distributed between Dark Energy or the Cosmological Constant (Λ;$\sim$ 70%) and Cold Dark Matter (CDM; $\sim$ 25%). The remaining energy density budget of the universe is accounted for by Baryons ($\sim$ 5%) and Radiation ($<$ 0.1%). While it is yet unclear what these Dark Matter and Dark Energy are at a fundamental particle level, they are the critical determinants of the large-scale structure (LSS) of the universe: the so-called Cosmic Web (see Fig. 1.1). Detailed N-body simulations of the Flat ΛCDM model have rendered the Dark Matter Cosmic Web (e.g. Springel et al., 2006) and shown that the current universe is comprised of overdense regions called "halos": gravitational potential wells into which matter is constantly pouring into. These "halos" are fed by "filaments" which are long, tubular structures that connect halos. The interstitial spaces between halos and filaments are "voids", regions of low density. Baryons essentially trace the underlying cosmic web and interact electromagnetically, rendering them "visible", in principle. Thus, they are the most important tracers for understanding the formation and evolution of the universe.

Thus motivated, Fukugita et al. (1998) performed a baryon census of the universe to identify the distribution of baryons between various phases: stars and their remnants, cold atomic and molecular gas, warm and hot ionized gas. Compared to the

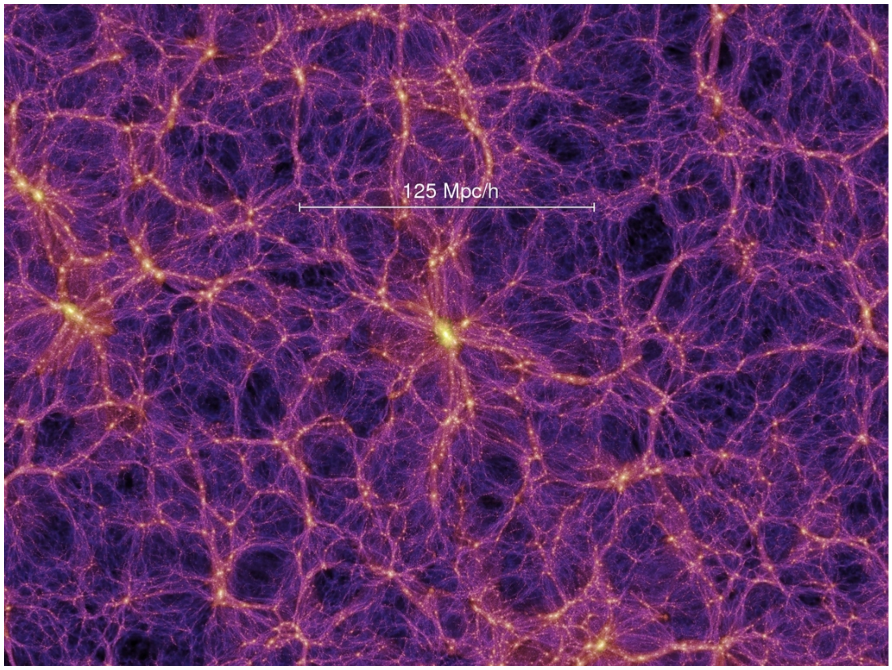

Figure 1.1: The large scale structure of the universe as revealed by the Millenium Simulation (Springel et al., 2006). The figure above shows the dark matter particle density in a slice of the simulation at $z = 0$. The universe on large scales exhibits a web-like structure that consists of overdense nodes called halos (bright yellow), tubular structures called filaments that connect halos (pink), and underdense interstitial regions called voids (black). *Image credit: MPIA: The Millenium Simulation*.

results from the CMB experiments, their best estimate for the total baryonic energy density of the universe was roughly 50% less. However, they did note a high degree of uncertainty in their methods. An updated census by Fukugita (2004) and subsequently, Shull et al. (2012), still estimated that $\sim 40\%$ of the baryons were not observed (see Fig. 1.2) and attributed this fraction of the budget to the diffuse ($\lesssim 10^{-5}$particles cm^{-3}) intergalactic plasma that pervades the cosmic web. Simulations showed that the extremely low density and nearly complete ionization of this phase, the so-called "Warm-Hot Intergalactic Medium" (WHIM; Davé et al., 2001; Cen & Ostriker, 2006), makes its detection extremely challenging through electromagnetic absorption and emission. Since then, various observational campaigns have attempted to detect this diffuse plasma. Most recently, there have been detections of weak X-ray absorption from metals (Nicastro et al., 2018; Nevalainen et al., 2019), X-ray emission from individual filaments (Werner et al., 2008; Eckert et al., 2015) and the statistical detection of the WHIM between galaxies in the cosmic web through stacking analysis of the Sunyaev-Zel'dovich effect (de Graaff et al., 2019; Tanimura et al., 2019) or X-ray emission (Tanimura et al., 2020). Indeed, as of 2019, although the Missing Baryon problem was tentatively resolved, significant uncertainties remained in the detected baryon fraction in the WHIM.

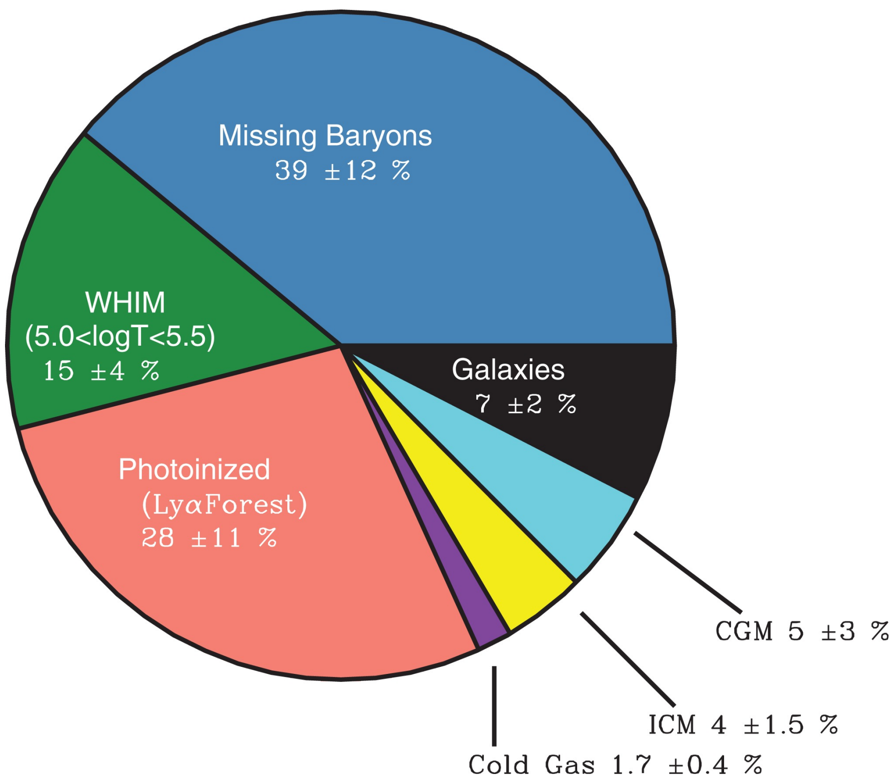

Figure 1.2: The baryon budget of the universe as of 2016. At $z \sim 0$, nearly 40 % of all baryons in the universe remained inaccessible. *Image credit: Nicastro (2016).*

1.2 Fast Radio Bursts: A new probe of the Cosmic Web

Fast Radio Bursts (FRBs) are a relatively new class of transient radio sources first reported by (Lorimer et al., 2007). These are energetic ($\sim 10^{40} erg/s$ emission assuming isotropy) and short-duration (~ 1 ms) radio pulses that are observed mainly at cosmological distances. Indeed, one of the best indications for their cosmological distances is the significant time delay (see Fig. 1.3) between the arrival of the pulse at different radio frequencies, which is consistent with the dispersion from intervening plasma:

$$\Delta t = 4.15s \left(\frac{DM}{1000\text{pc}\,\text{cm}^{-3}}\right)\left(\frac{\nu}{\text{GHz}}\right)^{-2} \tag{1.1}$$

where Δt is the time delay between two frequencies, DM is the dispersion measure and ν is the observing frequency (see Fig. 1.3). The dispersion measure is the integral of the electron density along the line of sight. Although in the non-relativistic regime, it is the same as the free electron column density, when accounting for cosmological distances, two relativistic effects become relevant as noted by Deng & Zhang (2014a). (1) The redshifting of the emission frequencies of the FRB and (2) the dilation of the pulse arrival times between different frequencies. The dispersion measure when is then given by:

$$\begin{aligned} DM &= \int \frac{n_e(z)}{1+z} dl \\ &= \int_0^{z_{FRB}} \frac{n_e(z)}{(1+z)^2} \frac{c}{H_0} \frac{dz}{\sqrt{\Omega_m(1+z)^3 + \Omega_\Lambda}} \end{aligned} \tag{1.2}$$

Here, dl is the distance element along the propagation path. n_e is the free

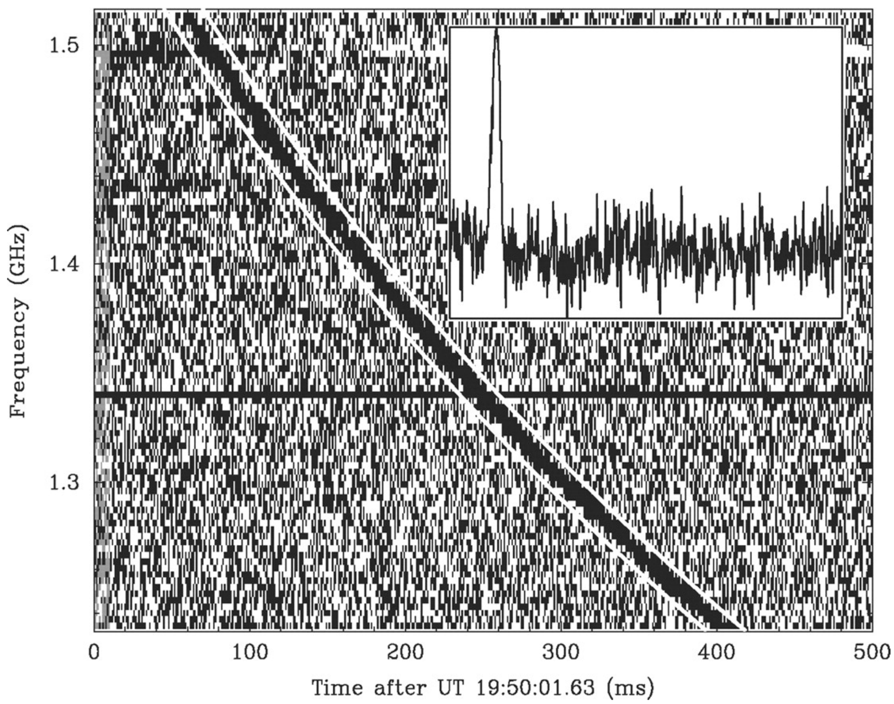

Figure 1.3: FRB dispersion as demonstrated by the first reported event. As the FRB pulse propagates through plasma, its frequencies are dispersed, resulting in a time delay in the arrival of lower frequencies. The dispersion is proportional to the inverse square of the frequency, resulting in the characteristic shape seen above. The figure inset shows the "dedispersed pulse", i.e., the result of removing the delay in the lower frequencies and summing the intensities in all frequency channels. *Image credit: Lorimer et al. (2007).*

electron density along the sightline. c is the speed of light in vacuum, H_0 is the Hubble constant, Ω_m and Ω_Λ are the matter and dark energy densities. It was obvious then that FRBs are sensitive to *all* of the ionized electrons, and hence, plasma, along the sightline and thus can potentially serve as a powerful and direct probe of the WHIM. As the FRB DM is an integrated quantity, one can describe it as a sum of the contributions from the Milky Way, the host galaxy, and the cosmic web. i.e.

$$DM_{\mathrm{FRB}} = DM_{\mathrm{MW}} + \mathrm{DM}_{\mathrm{cosmic}} + DM_{\mathrm{host}}/(1 + z_{\mathrm{FRB}}) \tag{1.3}$$

Here, DM_{MW} is the Milky Way contribution, $\mathrm{DM}_{\mathrm{cosmic}}$ is the cosmic web contribution, and DM_{host} is the host galaxy contribution in the host rest frame at $z = z_{\mathrm{FRB}}$. $\mathrm{DM}_{\mathrm{cosmic}}$ is the quantity of interest as it is probing the WHIM.

1.2.1 The need for precise localization of FRBs

Early detections of FRBs were performed using single-dish radio antennae (Lorimer et al., 2007; Thornton et al., 2013; Spitler et al., 2014; Scholz et al., 2016), which were extremely sensitive but offered poor spatial resolution (several arcminutes) on the sky. Although FRB detections had been steadily increasing since their discovery, locating their host galaxy from their several arcmin-wide localization regions was nearly impossible. Furthermore, the FRB radio detection itself did not offer any estimate of z_{FRB} . Therefore, it was difficult to fulfill their potential as astrophysical probes.

In 2017, the first FRB host galaxy was identified by Chatterjee et al. (2017) using the Karl G. Jansky Very Large Array (VLA) and the Gemini-North telescope. The FRB 20121102B was a source that repeated bursts (Spitler et al., 2014; Scholz et al., 2016) and thus, it was possible to point the VLA in the location of the Arecibo pointings used for previous detections and wait for the source to burst again. The VLA produced a sub-arcsecond precise localization image of the FRB event, allowing for a subsequent deep optical follow-up imaging. The host galaxy was found to be at a redshift of $z = 0.19273$ and was a dwarf star-forming galaxy (Tendulkar et al., 2017). This was a significant discovery as it unambiguously confirmed the cosmological nature of FRBs. Secondly, one could now measure the distance to the FRB by associating a host optically.

Within two years, the first non-repeating FRB host was reported by (Bannister et al., 2019, ; including Simha) using a novel two-step detection and subsequent localization technique on the Australian Square Kilometer Array Pathfinder (ASKAP) telescope. The FRB 20180924C was localized to a galaxy at $z = 0.3214$ and was found to be a massive, quiescent galaxy. [1] This host starkly contrasted with that of FRB20121102B and showed that FRBs were produced in various environments. Localizing one-off events was a significant achievement as it eliminated the need to wait for repeat bursts and an expensive follow-up campaign with a radio interferometer. Furthermore, with the availability of wide-field optical imaging data from surveys, it was also possible to identify brighter hosts ($m_r > 23$) immediately after localization for spectroscopic follow-up. Thus, the floodgates were opened for a new era of FRB research.

[1]On a personal note, this discovery thrust me into the exciting world of FRB research. On the day JXP had invited me to discuss potential projects, he showed me this discovery and introduced me to the Australian team behind the discovery. I am genuinely grateful to have been at the right place and time.

1.2.2 The Macquart relation: Baryons no longer missing

One can further expand eq. 1.2 for an average sightline in the universe by estimating $n_e(z)$. The majority of the baryon content of the universe is made from hydrogen and helium, whose mass fractions are roughly 0.75 and 0.25, respectively. Furthermore, below $z \sim 2$, nearly all baryons in the universe are fully ionized (Fan et al., 2006; McQuinn et al., 2009). Thus, $n_e(z)$ can be written as:

$$n_e(z) = \frac{7}{8} f_d(z) \frac{\rho_b(z)}{m_p} \tag{1.4}$$

Where $f_d(z)$ is the fraction of baryons in the diffuse plasma phase, m_p is the proton mass, and $\rho_b(z)$ is the total baryon density at redshift z (i.e., $\rho_b = \Omega_b \rho_{c,0}(1+z)^3$). The Macquart relation is then given by:

$$\mathrm{DM}_{\mathrm{cosmic}} = \frac{7c\Omega_b \rho_{c,0}}{8 m_p H_0} \int_0^{z_{FRB}} \frac{f_d(z)(1+z)dz}{\sqrt{\Omega_m(1+z)^3 + \Omega_\Lambda}} \tag{1.5}$$

By 2019, ASKAP had localized several FRB galaxies, and optical observations had confirmed their host galaxy redshifts. In their seminal paper, Macquart et al. (2020) plotted the ASKAP FRB sample's dispersion measures against their host galaxy redshifts (see Fig. 1.4). Then, they compared it against the mean $\mathrm{DM}_{\mathrm{cosmic}}$-$z_{\mathrm{FRB}}$ relation (black curve), assuming an average $f_d(z)$ estimated from the baryon census of Fukugita (2004). This simple yet powerful analysis made it clear that the ionized baryon fraction of the universe was indeed consistent with the presence of all the expected baryons: the baryons were found! The Missing Baryon Problem was, therefore, unambiguously resolved.

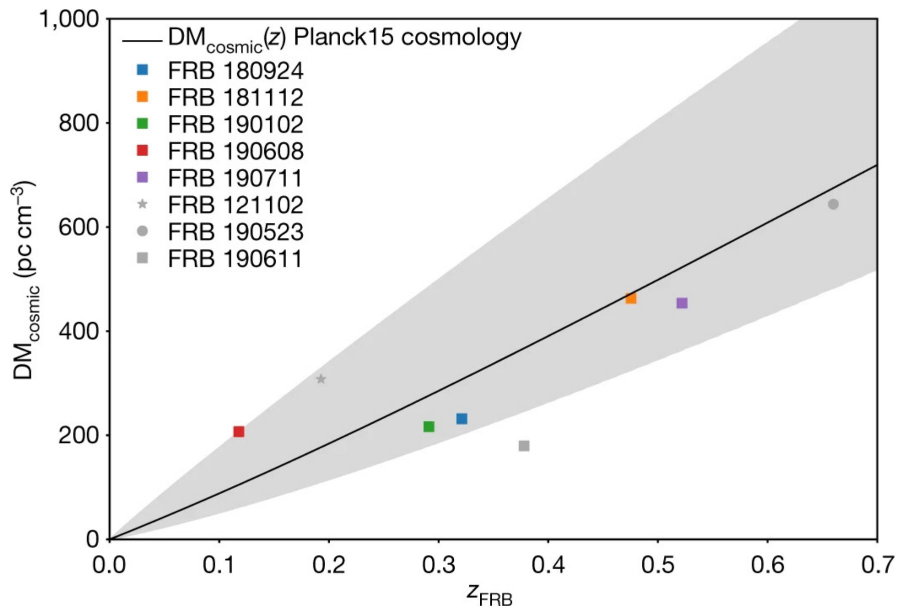

Figure 1.4: The Macquart relation. The black curve is the mean DM$_{\text{cosmic}}$-z_{FRB} relation assuming an average $f_d(z)$ estimated from the baryon census of Fukugita (2004). The colored points are the ASKAP FRB sample. The Macquart relation is consistent with the mean DM$_{\text{cosmic}}$ expected at the redshift of the FRB host galaxies within the 90% uncertainties (grey-shaded regions). An updated version of this plot is presented later in Chapter 5 as Fig. 5.1 with more recent FRB localizations. *Image credit: Macquart et al. (2020)*.

1.3 This thesis: Beyond the Macquart Relation

While the Macquart relation provided definitive observational evidence for the presence of the WHIM, it gave rise to a new question: where are the baryons located? i.e., The mean $\mathrm{DM_{cosmic}}$-z_{FRB} relation is agnostic to the location of the foreground baryons: within individual halos or the diffuse filaments cosmic web filaments. This information is encoded within the scatter around the Macquart relation (grey shading in Fig. 1.4). Individual sightlines in the universe are subject to Poissonian random intersections of halos and filaments, and thus, their $\mathrm{DM_{cosmic}}$ can vary significantly from the mean value at z_{FRB}. Macquart et al. (2020) modeled the PDF of $\mathrm{DM_{cosmic}}$ at a given redshift as:

$$p(\Delta) = A\Delta^{-\beta} \exp\left[-\frac{(\Delta^{-\alpha} - C_0)^2}{2\alpha^2\sigma_{DM}^2}\right] \tag{1.6}$$

Where $\Delta = \mathrm{DM_{cosmic}}/\langle\mathrm{DM_{cosmic}}\rangle$, $\langle\mathrm{DM_{cosmic}}\rangle$ is the mean $\mathrm{DM_{cosmic}}$ at a given redshift, α and β are the shape parameters of the power-law tail and C_0 is the mean value of the log-normal distribution. σ_{DM} is the scatter in the $\mathrm{DM_{cosmic}}$ at a given redshift. σ_{DM} is modeled as $Fz^{-0.5}$, where F is the "feedback" or the "fluctuation" parameter. Two key features of the distribution are important to note: (1) at low Δ, $p(\Delta) \approx 0$, and there is a sharp DM cut-off above which the PDF becomes non-negligible. Such a low $\mathrm{DM_{cosmic}}$ value can arise within sightlines that only intersect voids. (2) At high Δ values, the PDF has an exponential tail, which reflects the possibility of intersecting massive overdensities such as clusters of galaxies. Indeed, at a typical ASKAP FRB redshift of 0.5, the scatter is roughly 50% of the mean value.

The work described in the following chapters is a systematic attempt to resolve the variation in the DMs along individual FRB sightlines. It leverages foreground optical data to infer the baryon distribution in the cosmic web. I have led three journal publications on foreground matter along individual sightlines using spectroscopic and photometric surveys to identify intervening halos and filaments. Thus informed, one can synthesize independent estimates of the $\mathrm{DM}_{\mathrm{cosmic}}$ along each sightline with models of gas distribution within intersecting halos and the diffuse IGM. Chapter 2 describes the case study of an individual sightline, FRB20190608B, enabled by the availability of foreground spectroscopic data. Chapter 3 further expands upon this framework to include photometric redshifts in the foreground DM analysis. Chapter 5 is the first work I have led as part of the FLIMFLAM survey team that analyzes four sightlines with a significant excess in $\mathrm{DM}_{\mathrm{cosmic}}$ compared to the Macquart relation. In addition to my work on FRBs, in Chapter 4, I will describe the instrument upgrade project I have undertaken for the optical detector of the Low-Resolution Imaging Spectrograph (LRIS) on board the Keck I telescope. LRIS, among other instruments, was used to gather the spectroscopic data for a subset of the FRB sightlines in the FLIMFLAM survey. In Chapter 6, I will conclude by describing the ongoing FLIMFLAM survey and the prospects for FRBs as probes of the large-scale structure in the near future.

Chapter 2

Disentangling the Cosmic Web Towards FRB 190608

Abstract

Probing the Cosmic Web with Fast Radio Bursts

by

H. S. Sunil Simha

The Fast Radio Burst (FRB) 190608 was detected by the Australian Square-Kilometer Array Pathfinder (ASKAP) and localized to a spiral galaxy at $z_{\rm host} = z_{\rm FRB}$ in the Sloan Digital Sky Survey (SDSS) footprint. The burst has a large dispersion measure ($\rm DM_{FRB} = 362.16\ pc\,cm^{-3}$) compared to the expected cosmic average at its redshift. It also has a large rotation measure ($\rm RM_{FRB} = 353\ rad\ m^{-2}$) and scattering timescale ($\tau =$ 3.3 ms at 1.28 GHz). Chittidi et al. (2020) perform a detailed analysis of the ultraviolet and optical emission of the host galaxy and estimate the host DM contribution to be $110 \pm 37\ \rm pc\,cm^{-3}$. This work complements theirs and reports the analysis of the optical data of galaxies in the foreground of FRB 190608 in order to explore their contributions to the FRB signal. Together, the two studies delineate an observationally driven, end-to-end study of matter distribution along an FRB sightline; the first study of its kind. Combining our Keck Cosmic Web Imager (KCWI) observations and public SDSS data, we estimate the expected cosmic dispersion measure $\rm DM_{cosmic}$ along the sightline to FRB 190608. We first estimate the contribution of hot, ionized gas in intervening virialized halos ($\rm DM_{halos} \approx 7 - 28\ pc\,cm^{-3}$). Then, using the Monte Carlo Physarum Machine (MCPM) methodology, we produce a 3D map of ionized gas in cosmic web filaments and compute the DM contribution from matter outside halos ($\rm DM_{IGM} \approx 91 - 126\ pc\,cm^{-3}$). This implies a greater fraction of ionized gas along this

sightline is extant outside virialized halos. We also investigate whether the intervening halos can account for the large FRB rotation measure and pulse width and conclude that it is implausible. Both the pulse broadening and the large Faraday rotation likely arise from the progenitor environment or the host galaxy.

2.1 Introduction

Galaxies are the result of gravitational accretion of baryons onto dark matter halos, i.e. the dense gas that has cooled and condensed to form dust, stars, and planets. The dark matter halos, according to simulations, are embedded in the cosmic web, a filamentous structure of matter (e.g. Springel et al., 2005). The accretion process of galaxies is further predicted, at least for halo masses $M_{\rm halo} \gtrsim 10^{12}$ $\mathrm{M}_\odot$, to generate a halo of baryons, most likely dominated by gas shock-heated to the virial temperature of the potential well (White & Rees, 1978; White & Frenk, 1991; Kauffmann et al., 1993; Somerville & Primack, 1999; Cole et al., 2000). At $T \gtrsim 10^6$ K and $n_e \sim 10^{-4}\,\mathrm{cm}^{-3}$, however, this halo gas is very difficult to detect in emission (Kuntz & Snowden, 2000; Yoshino et al., 2009; Henley & Shelton, 2013) and similarly challenging to observe in absorption (e.g. Burchett et al., 2019). And while experiments leveraging the Sunyaev-Zeldovich effect are promising (Planck Collaboration et al., 2016b), these are currently limited to massive halos and are subject to significant systematic effects (Lim et al., 2020).

Therefore, there has been a wide range of predictions for the mass fraction of baryons in massive halos that range from $\approx 10\%$ to nearly the full complement relative to the cosmic mean Ω_b/Ω_m (Pillepich et al., 2018). Here, Ω_b and Ω_m are the average cosmic densities of baryons and matter respectively. Underlying this order-of-magnitude spread in predictions are uncertain physical processes that eject gas from galaxies and can greatly shape them and their environments (e.g. Suresh et al., 2015).

Fast radio bursts (FRBs) are dispersed by intervening ionized matter such that the pulse arrival delay, with respect to a reference frequency, scales as the inverse square of frequency times the DM. The DM is the path integral of the electron density, n_e, weighted by the scale factor $(1+z)^{-1}$, i.e. $\mathrm{DM} \equiv \int n_e \, ds/(1+z)$. These FRB measurements are sensitive to all of the ionized gas along the sightline. Therefore, they have the potential to trace the otherwise invisible plasma surrounding and in-between galaxy halos (Macquart et al., 2020). The Fast and Fortunate for FRB Follow-up (F^4) team[1] has initiated a program to disentangle the cosmic web by correlating the dispersion measure (DM) of fast radio bursts (FRBs) with the distributions of foreground galaxy halos (McQuinn, 2014a; Prochaska & Zheng, 2019). This manuscript marks our first effort.

Since the DM is an additive quantity, it may be split into individual contributions of intervening, ionized gas reservoirs:

$$\mathrm{DM_{FRB}} = \mathrm{DM_{MW}} + \mathrm{DM_{cosmic}} + \mathrm{DM_{host}} \tag{2.1}$$

Here, $\mathrm{DM_{MW}}$ refers to the contribution from the Milky Way which is further split into its ISM and halo gas contributions ($\mathrm{DM_{MW,ISM}}$ and $\mathrm{DM_{MW,halo}}$ respectively). Additionally, $\mathrm{DM_{host}}$ is the net contribution from the host galaxy and its halo, including any contribution from the immediate environment of the FRB progenitor. Meanwhile, $\mathrm{DM_{cosmic}}$ is the sum of contributions from gas in the circumgalactic medium (CGM) of intervening halos ($\mathrm{DM_{halos}}$) and the intergalactic medium (IGM; $\mathrm{DM_{IGM}}$). Here, CGM refers to the gas found within dark matter halos including the intracluster medium of galaxy clusters, and the IGM refers to gas between galaxy halos.

Macquart et al. (2020) have demonstrated that the FRB population defines a

[1]http://www.ucolick.org/f-4

cosmic DM-z relation that closely tracks the prediction of modern cosmology (Inoue, 2004; Prochaska & Zheng, 2019; Deng & Zhang, 2014b), i.e., the average cosmic DM is

$$\langle \mathrm{DM_{cosmic}} \rangle = \int_0^{z_{\mathrm{host}}} \bar{n}_e(z) \frac{c dz}{H(z)(1+z)^2} \tag{2.2}$$

with $\bar{n}_e = f_d(z)\rho_b(z)/m_p(1 - Y_{\mathrm{He}}/2)$, which is the mean density of electrons at redshift z. Here, m_p is the proton mass, $Y_{\mathrm{He}} = 0.25$ is the mass fraction of Helium (assumed doubly ionized in this gas), $f_d(z)$ is the fraction of cosmic baryons in diffuse ionized gas, i.e. excluding dense baryonic phases such as stars and neutral gas (see Macquart et al., 2020, and Appendix .1). $\rho_b(z) = \Omega_{b,0}\rho_{c,0}(1+z)^3$, $\rho_{c,0}$ is the critical density at $z = 0$, and $\Omega_{b,0}$ is the baryon energy density today relative to $\rho_{c,0}$. c is the speed of light in vacuum and $H(z)$ is the Hubble parameter. Immediately relevant to the study at hand, for FRB 190608, $\langle \mathrm{DM_{cosmic}} \rangle \approx 100$ pc cm^{-3} at $z_{\mathrm{host}} = z_{\mathrm{FRB}}$.

Of the five FRBs in the Macquart et al. (2020) 'gold' sample, FRB 190608 exhibits a $\mathrm{DM_{cosmic}}$ value well in excess of the average estimate for its redshift: $\mathrm{DM_{cosmic}}/\langle \mathrm{DM_{cosmic}} \rangle \approx 2$ based on the estimated contributions of $\mathrm{DM_{MW,halo}}$ and $\mathrm{DM_{host}}$. This is illustrated in Fig. 2.1, which compares the measured $\mathrm{DM_{FRB}} = 362.16$ pc cm^{-3} (Day et al., 2020) with the cumulative contributions from the Galactic ISM (taken as $\mathrm{DM_{MW,ISM}} = 38$ pc cm^{-3}; Cordes & Lazio, 2003a), the Galactic halo (taken as $\mathrm{DM_{MW,halo}} = 40$ pc cm^{-3}; Prochaska & Zheng, 2019), and the average cosmic web (Equation 2.2). These fall ≈ 160 pc cm^{-3} short of the observed value. Chittidi et al. (2020) estimate the host galaxy ISM contributes $\mathrm{DM_{host,ISM}} = 82 \pm 35$ pc cm^{-3} based on the observed Hβ emission measure and $\mathrm{DM_{host,halo}} = 28 \pm 13$ pc cm^{-3} for the host galaxy's halo, thus nearly accounting for the deficit. The net $\mathrm{DM_{host}}$ is therefore taken here to be 110 ± 37 pc cm^{-3}.

While these estimates almost fully account for the large $\mathrm{DM_{FRB}}$, several of them bear significant uncertainties (e.g., $\mathrm{DM_{MW,halo}}$ and $\mathrm{DM_{host}}$). Furthermore, we have assumed the average $\mathrm{DM_{cosmic}}$ value, a quantity predicted to exhibit significant variance from sightline to sightline (McQuinn, 2014a; Prochaska & Zheng, 2019; Macquart et al., 2020). Therefore, in this work we examine the galaxies and large-scale structure foreground to FRB 190608 to analyze whether $\mathrm{DM_{cosmic}} \approx \langle \mathrm{DM_{cosmic}} \rangle$ or whether there is significant deviation from the cosmic average. These analyses constrain several theoretical expectations related to $\langle \mathrm{DM_{cosmic}} \rangle$ (e.g. McQuinn, 2014a; Prochaska & Zheng, 2019). In addition, FRB 190608 exhibits a relatively large rotation measure (RM = 353 rad m^{-2}) and a large, frequency dependent exponential tail ($\tau_{1.4\mathrm{Ghz}} = 2.9$ ms) in its temporal pulse profile that corresponds to scatter-broadening (Day et al., 2020). We explore the possibility that these arise from foreground matter overdensities and/or galactic halos (similar to the analysis by Prochaska et al., 2019).

This paper is organized as follows. In Section 2, we present our data on the host and foreground galaxies and our spectral energy distribution (SED) fitting method for determining galaxy properties. In Section 3, we describe our methods and models in estimating the separate $\mathrm{DM_{cosmic}}$ contributions from intervening halos and the diffuse IGM. Section 4 explores the possibility of a foreground structure accounting for the FRB rotation measure and pulse width. Finally, in Section 5, we summarise and discuss our results. Throughout our analysis, we use cosmological parameters derived from the results of Planck Collaboration et al. (2016a).

2.2 Foreground Galaxies

2.2.1 The Dataset

FRB 190608 was detected and localized by the Australian Square Kilometre Array Pathfinder (ASKAP) to RA = 21h44m25.25s, Dec = $-40°54'0.1''$(Day et al., 2020), placing it in the outer disk of the galaxy J214425.25−405400.81 at $z = z_{\rm FRB}$ (hereafter HG 180924) cataloged by the Sloan Digital Sky Survey (SDSS).

To search for nearby foreground galaxies, we obtained six $33'' \times 20''$ integral field unit (IFU) exposures (1800 s each) using the Keck Cosmic Web Imager (KCWI; Morrissey et al., 2018a) in a mosaic centered at the host galaxy centroid. The IFU was used in the "large" slicer position with the "BL" grating, resulting in a spectral resolution, $R_0 \sim 900$. The six exposures cover an approximately $1' \times 1'$ field around the FRB host. They were reduced using the standard KCWI reduction pipeline (Morrissey et al., 2018a) with sky subtraction (see Chittidi et al., 2020, for additional details).

From the reduced cubes, we extracted the spectra of sources identified in the white-light images using the Source Extractor and Photometry (SEP) package (Barbary, 2016; Bertin & Arnouts, 1996). We set the detection threshold to 1.5 times the estimated RMS intensity after background subtraction and specified a minimum source area of 10 pixels ($\sim$ 5 kpc at $z = 0.05$) to be a valid detection. Thirty sources were identified this way across the six fields; none have SDSS spectra. SEP determines the spatial light profiles of the sources and for each source outputs major and minor axis values of a Gaussian fit. Using elliptical apertures with twice those linear dimensions, we extracted source spectra. We then determined their redshifts using the Manual and Automatic Redshifting Software (MARZ, Hinton et al., 2016). MARZ fits each spectrum with a template spectrum and determines the redshift corresponding to the maximum cross-correlation. Seven objects had unambiguous redshift estimates, whereas the rest did not show any identifiable line emission. Five of the seven objects with secure redshifts are at $z > z_{\mathrm{host}}$ and are not discussed further. We observed two objects (RA = $22^{\mathrm{h}}16^{\mathrm{m}}4.86^{\mathrm{s}}$, Dec = $-7°53'44.16''$ eq. J2000) with a single strong emission feature at 4407 Å for one and 3908 Å for the other. MARZ reported high cross-correlations with its templates for when this feature was associated with either the [O II]3727-3729 Å doublet (corresponding to $z < z_{\mathrm{FRB}}$) or Lyα (corresponding to $z > 2$). There are no other discernible emission lines in the spectra. If we assume the emission line is indeed [O II], we can then measure the the peak intensity of Hβ. Thus, in both spectra, the Hβ peak would be less than 0.02 times the [O II] peak intensity, which would imply an impossible metallicity. Thus we conclude that the features are likely Lyα and place these as galaxies at $z > 2.6$.

In the remaining 23 spectra, we detect no identifiable emission lines. Since we measure only weak continua (per-pixel SNR < 1), if any, from the remaining 23 objects, we find it difficult to estimate the likelihood of their being foreground objects from synthetic colors.

We experimented with decreasing the minimum detection area threshold to 5 pixels. This increases the number of detected sources, but the additional sources, assuming they are actually astrophysical, do not have any identifiable emission lines. These sources are most likely fluctuations in the background.

To summarize, we found no foreground galaxy in the 1 arcmin sq. KCWI field.

Assuming the halo mass function derived from the Aemulus project (McClintock et al., 2019), the average number of foreground halos (i.e., for $z < z_{\mathrm{host}}$ and in a $1' \times 1'$ field) between 2×10^{10} $\mathrm{M}_{\odot}$ and 10^{16} $\mathrm{M}_{\odot}$ is 0.23; therefore, the absence of objects can be attributed to Poisson variance. This general conclusion remains valid even when we refine the expected number of foreground halos based on the inferred overdensities along the line of sight (see Section 2.3.2.2).

To expand the sample, we then queried the SDSS-DR16 database for all spectroscopically confirmed galaxies with impact parameters $b < 5\,\mathrm{Mpc}$ (physical units) to the FRB sightline and $z < z_{\mathrm{host}}$. This impact parameter threshold was chosen to encompass any galaxy or large-scale structure that might contribute to $\mathrm{DM}_{\mathrm{cosmic}}$ along the FRB sightline. As the FRB location lies in one of the narrow strips in the SDSS footprint, the query is spatially truncated in the north-eastern direction. Effectively no object with $b \gtrsim 2.5$ Mpc in that direction was present in the query results due to this selection effect.

We further queried the SDSS database for all galaxies with photometric redshift estimates such that $z_{\mathrm{phot}} - 2\delta z_{\mathrm{phot}} < z_{\mathrm{host}}$ and $z_{\mathrm{phot}}/\delta z_{\mathrm{phot}} > 1$. Here δz_{phot} is the error in z_{phot} reported in the database. We rejected objects that were flagged as cosmic rays or were suspected cosmic rays or CCD ghosts. None of these recovered galaxies lie within 250 kpc of the sightline as estimated from z_{phot}. However, several galaxies were found with $z_{\mathrm{phot}} > z_{\mathrm{host}}$ and $z_{\mathrm{phot}} - 2\delta z_{\mathrm{phot}} < z_{\mathrm{host}}$ that can be within 250 kpc if their actual redshifts were closer to $z_{\mathrm{phot}} - 2\delta z_{\mathrm{phot}}$.

2.2.2 Derived Galaxy Properties

For each galaxy in the spectroscopic sample, we have estimated its stellar mass, M_*, by fitting the SDSS *ugriz* photometry with an SED using CIGALE (Noll et al., 2009). We assumed, for simplicity, a delayed-exponential star-formation history with no burst population, a synthetic stellar population prescribed by Bruzual & Charlot (2003), the Chabrier (2003) initial mass function (IMF), dust attenuation models from Calzetti (2001), and dust emission templates from Dale et al. (2014), where the AGN fraction was capped at 20%. The models typically report a $\lesssim 0.1$ dex statistical uncertainty on M_* and star formation rate from the SED fitting, but we estimate systematic uncertainties are $\approx 2\times$ larger. Table 2.1 lists the observed and derived properties for the galaxies.

Central to our estimates of the contribution of halos to the DM is an estimate of the halo mass, $M_{\rm halo}$. A commonly adopted procedure is to estimate $M_{\rm halo}$ from the derived stellar mass, M_*, by using the abundance matching technique. Here, we adopt the stellar-to-halo-mass ratio (SHMR) of Moster et al. (2013), which also assumes the Chabrier IMF. Estimated halo masses of the foreground galaxies range from 10^{11} M$_\odot$ to $\gtrsim 10^{12}$ M$_\odot$.

2.2.3 Redshift distribution of foreground galaxies

Fig. 2.2 shows the distribution of impact parameters and spectroscopic redshifts for the foreground galaxies. There is a clear excess of galaxies at $z \sim 0.08$. Empirically, there are 50 galaxies within a redshift range $\Delta z = 0.005$ of $z = 0.0845$. A review of group and cluster catalogs of the SDSS (Yang et al., 2007; Rykoff et al., 2014), however, shows no massive collapsed structure ($M_{\rm halo} > 10^{13}$M$_\odot$) at this redshift and

Table 2.1: Observed and derived properties of the spectroscopic foreground galaxies from SDSS.

RA deg	Dec deg	u mag	g mag	r mag	i mag	z mag	Redshift	b kpc	$\log(M_*/M_\odot)$	$\log(M_{halo}/M_\odot)$
334.00914	-7.87554	18.73	17.54	16.98	16.63	16.37	0.09122	158	10.36	11.81
333.97368	-7.87678	19.28	17.87	16.95	16.50	16.20	0.08544	300	10.59	12.09
333.88476	-8.01812	18.48	17.39	16.92	16.72	16.59	0.02732	367	9.06	11.04
334.01930	-8.02294	18.31	16.58	15.74	15.38	15.13	0.06038	541	10.63	12.17
334.04856	-7.79251	19.89	17.99	17.05	16.63	16.19	0.07745	597	10.54	12.01

within $b = 2.5\,\mathrm{Mpc}$ of the sightline. The closest redMaPPer cluster at this redshift is at a transverse distance of 8.7 Mpc. However, we must keep in mind that the survey is spatially truncated in the north-eastern direction and therefore we cannot conclusively rule out the presence of a nearby galaxy group or cluster. Nevertheless, the distribution suggests an overdensity of galaxies tracing some form of large-scale structure, e.g. a filament connecting this distant cluster to another (see Section 2.3.2.2).

To empirically assess the statistical significance of FRB 190608 exhibiting an excess of foreground galaxies (which would suggest an excess $\mathrm{DM_{cosmic}}$), we performed the following analysis. First, we defined a grouping[1] of galaxies using a Mean-Shift clustering algorithm on the galaxy redshifts in the field adopting a bandwidth Δz of 0.005 ($\approx 3100\ \mathrm{km\,s^{-1}}$). This generates a redshift centroid and the number of galaxies in a series of groupings for the field. For the apparent overdensity, we recover $z = 0.0843$ and $N = 62$ galaxies; this is the grouping with the highest cardinality in the field. We then generated 1000 random sightlines in the SDSS footprint and obtained the redshifts of galaxies with $z < z_{\mathrm{host}}$ and with impact parameters $b < 5$ Mpc, restricting the sample to galaxies with $z > 0.02$ for computational expediency. We also restricted the stellar masses to lie above $10^{9.3}\ \mathrm{M_\odot}$ to account for survey completeness near z = 0.08. This provides a control sample for comparison with the FRB 190608 field.

Fig. 2.3 shows the cumulative distribution of the number of galaxies in the most populous groupings in each field. We find that the FRB field's largest grouping is at the 63$^{\mathrm{rd}}$ percentile, and therefore conclude that it is not a rare overdensity. It might, however, make a significant contribution to $\mathrm{DM_{cosmic}}$, a hypothesis that we explore in

[1]We avoid the use of group or cluster to minimize confusion with those oft used terms in astronomy.

the next section.

2.3 DM Contributions

This section estimates $\mathrm{DM_{halos}}$, and $\mathrm{DM_{IGM}}$. For the sake of clarity, we make a distinction in the terminology we use to refer to the cosmic contribution to the dispersion measure estimated in two different ways. First, we name the difference between $\mathrm{DM_{FRB}}$ and the estimated host and Milky Way contributions $\mathrm{DM_{FRB,C}}$ i.e. $\mathrm{DM_{FRB,C}} = \mathrm{DM_{FRB}} - \mathrm{DM_{MW}} - \mathrm{DM_{host}} \approx 152\,\mathrm{pc\,cm^{-3}}$. Second, we shall henceforth use the term $\mathrm{DM_{cosmic}}$ to refer to the sum of $\mathrm{DM_{halos}}$ and $\mathrm{DM_{IGM}}$ semi-empirically estimated from the foreground galaxies.

2.3.1 Foreground halo contribution to $\mathrm{DM_{cosmic}}$

We first consider the DM contribution from halo gas surrounding foreground galaxies, $\mathrm{DM_{halos}}$. For the four galaxies with $b < 550\,\mathrm{kpc}$, all have estimated halo masses $M_{\rm halo} \leq 10^{12.2}\ \mathrm{M_\odot}$. We adopt the definition of r_{vir} using the formula for average virial density from Bryan & Norman (1998), i.e. the average halo density enclosed within r_{vir} is:

$$\begin{aligned} \rho_{vir} &= (18\pi^2 - 82q - 39q^2)\rho_c \\ q &= \frac{\Omega_{\Lambda,0}}{\Omega_{m,0}(1+z)^3 + \Omega_{\Lambda,0}} \end{aligned} \tag{2.3}$$

Here ρ_c is the critical density of the universe at redshift z and $\Omega_{\Lambda,0}$ is the dark energy density relative to $\rho_{c,0}$. Computing r_{vir} from the estimated halo masses we find that only the halo with the smallest impact parameter at $z = 0.09122$ (i.e. first entry in

Table 2.1) is intersected by the sightline. In the following, however, we will allow for uncertainties in $M_{\rm halo}$ and also consider gas out to $2r_{vir}$. Nevertheless, we proceed with the expectation that $\rm DM_{halos}$ is small.

To derive the DM contribution from each halo, we must adopt a gas density profile and the total mass of baryons in the halo. For the former, we assume a modified Navarro-Frenk-White (NFW) baryon profile as described in Prochaska & Zheng (2019), with profile parameters $\alpha = 2$ and $y_0 = 2$. We terminate the profile at a radius $r_{\rm max}$, given in units of r_{vir} (i.e., $r_{\rm max}$=1 corresponds to r_{vir}). The gas composition is assumed to be primordial, i.e., 75% hydrogen and 25% helium by mass. For the halo gas mass, we define $M^b_{\rm halo} \equiv f_{\rm hot}(\Omega_b/\Omega_m)M_{\rm halo}$, with $f_{\rm hot}$ parametrizing the fraction of the total baryonic budget present within the halo as hot gas. For a halo that has effectively retained all of its baryons, a canonical value is $f_{\rm hot} = 0.75$, which allows for $\approx 25\%$ of the baryons to reside in stars, remnants, and neutral gas of the galaxy at its center (e.g. Fukugita et al., 1998). If feedback processes have effectively removed gas from the halo, then $f_{\rm hot} \ll 0.75$. For simplicity, we do not vary $f_{\rm hot}$ with halo mass but this fraction might well be a function of halo properties (e.g. Behroozi et al., 2010).

At present, we have only weak constraints on $f_{\rm hot}$, α, and y_0, and we emphasize that our fiducial values are likely to maximize the DM estimate for a given halo (unless the impact parameter is $\ll r_{vir}$). We therefore consider the estimated $\rm DM_{halos}$ to be an upper bound. However, we further note that the choice of $r_{\rm max}$, which effectively sets the size of the gaseous halo is largely arbitrary. In the following, we consider $r_{\rm max} = 1$ and 2.

The DM contribution of each foreground halo was computed by estimating the column density of free electrons intersecting the FRB sightline. Fig. 2.4a shows the estimate of $\mathrm{DM_{halos}}$ for $r_{\mathrm{max}} = 1$. When $r_{\mathrm{max}} = 2$ (Fig. 2.4b), the halo at $z = 0.09122$ (Table 2.1) contributes an additional ~ 10 pc cm^{-3} to the $\mathrm{DM_{halos}}$ estimate from the extended profile. Furthermore, the halo at $z = 0.08544$ contributes ~ 10 pc cm^{-3} and the halo at $z = 0.06038$ contributes ~ 2 pc cm^{-3}.

In addition to the spectroscopic sample, we performed a similar analysis on the sample of galaxies with z_{phot} only. As mentioned earlier, no galaxy in this sample was found within 250 kpc if their redshift was assumed to be z_{phot} and therefore, their estimated contribution to $\mathrm{DM_{halos}}$ was null. However, if we assumed their redshifts were $z_{\mathrm{phot}} - 2\delta z_{\mathrm{phot}}$, we estimate a net DM contribution of ~ 30 pc cm^{-3} from four galaxies (Table 2.2). Their contribution decreases with increasing assumed redshift. At z_{host}, only the first two galaxies contribute and their net contribution is estimated to be ~ 13 pc cm^{-3}. A spectroscopic follow-up is necessary to pin down the galaxies' redshifts and therefore their DM contribution as they lie outside our the field of view of our KCWI data.

Using the aforementioned assumptions for the halo gas profile, we can compute the average contribution to $\langle \mathrm{DM_{cosmic}} \rangle$, i.e. $\langle \mathrm{DM_{halos}} \rangle$, by estimating the fraction of cosmic electrons enclosed in halos, $f_{\mathrm{e,halos}}(z)$. $\langle \mathrm{DM_{halos}} \rangle$ provides a benchmark that we may compare against $\mathrm{DM_{halos}}$. First, we find the average density of baryons found in halos between $10^{10.3}$ $\mathrm{M_\odot}$ and 10^{16} $\mathrm{M_\odot}$ using the Aemulus halo mass function (McClintock et al., 2019), i.e. $\rho_{b,\mathrm{halos}}(z)$. The ratio of this density to the cosmic matter

Table 2.2: SDSS galaxies with photometric redshifts that potentially contribute to $\mathrm{DM_{halos}}$

RA deg	Dec deg	Separation from FRB arcmin	u mag	g mag	r mag	i mag	z mag	z_{phot}	δz_{phot}
334.01251	-7.88616	0.84	22.09	20.41	19.56	19.34	18.94	0.21	0.06
334.03281	-7.90426	0.86	23.62	22.18	21.25	20.94	20.22	0.27	0.12
334.03590	-7.88558	1.22	22.89	22.33	21.31	21.08	19.63	0.34	0.13
334.00943	-7.87979	1.26	21.00	20.04	19.40	19.16	18.95	0.15	0.04

density $\rho_b(z)$ is termed f_{halos}. Then, according to our halo gas model, $f_{\text{e,halos}}(z)$ is:

$$\begin{aligned} f_{\text{e,halos}}(z) &= \frac{\bar{n}_{e,\text{halos}}(z)}{\bar{n}_e(z)} = \frac{\rho_{b,\text{halos}}(z) f_{\text{hot}}}{\rho_b(z) f_d(z)} \\ &= f_{\text{halos}}(z) \frac{f_{\text{hot}}}{f_d(z)} \end{aligned} \tag{2.4}$$

Lastly, we relate $\langle \text{DM}_{\text{halos}} \rangle = f_{e,\text{halos}} \times \langle \text{DM}_{\text{cosmic}} \rangle$. The dashed lines in Fig. 2.4 represent $\langle \text{DM}_{\text{halos}} \rangle$, and we note that the DM_{halos} for the FRB sightline is well below this value at all redshifts.

There are two major sources of uncertainty in estimating DM_{halos}. First, stellar masses are obtained from SED fitting and have uncertainties of the order of 0.1 dex. In terms of halo masses, this translates to an uncertainty of ~ 0.15 dex if the mean SHMR is used. Second, there is scatter in the SHMR which is also a function of the stellar mass. Note that the intervening halos have stellar masses $\sim 10^{10.6}$ $\text{M}_\odot$. This corresponds to an uncertainty in the halo mass of ~ 0.25 dex (Moster et al., 2013). In Fig. 2.4, we have varied stellar masses by 0.1 dex and have depicted the variation in DM_{halos} through the shaded regions. If instead, we varied the stellar masses by 0.16 dex, thus mimicking a variation in halo masses by nearly 0.25 dex, the scatter increases by roughly 10 $\text{pc}\,\text{cm}^{-3}$ in Fig. 2.4a. and about 20 $\text{pc}\,\text{cm}^{-3}$ in Fig. 2.4b at $z = z_{\text{FRB}}$.

For the remainder of our analysis, we shall use the estimate for DM_{halos} corresponding to $r_{\text{max}} = 1$, i.e. DM_{halos}= 12 $\text{pc}\,\text{cm}^{-3}$ and is bounded between 7 $\text{pc}\,\text{cm}^{-3}$ and 28 $\text{pc}\,\text{cm}^{-3}$, while bearing in mind that it may be roughly two times larger if the radial extent of halo gas exceeds r_{vir}. For the galaxies with photometric redshifts only, we shall adopt z_{phot} and thus estimate no contribution to DM_{halos}.

2.3.2 $\mathrm{DM_{IGM}}$ and $\mathrm{DM_{cosmic}}$

We now proceed to estimate the other component of $\mathrm{DM_{cosmic}}$, $\mathrm{DM_{IGM}}$, the contribution from diffuse gas outside halos. In this section, we discuss two approaches to estimating $\mathrm{DM_{IGM}}$.

1. The diffuse IGM is assumed to be uniform and isotropic. This implies its DM contribution is completely determined by cosmology and our assumptions for $\mathrm{DM_{halos}}$. This is equivalent to estimating the cosmic average of the IGM contribution, $\langle \mathrm{DM_{IGM}} \rangle$.

2. Owing to structure in the cosmic web, the IGM is not assumed to be uniform. We infer the 3D distribution of the cosmic web using the galaxy distribution and then use this to compute $\mathrm{DM_{IGM}}$.

We consider each of these in turn.

2.3.2.1 $\langle \mathrm{DM_{IGM}} \rangle$

Approach 1 is an approximation of $\mathrm{DM_{IGM}}$. We define:

$$\langle \mathrm{DM_{IGM}} \rangle = \langle \mathrm{DM_{cosmic}} \rangle - \langle \mathrm{DM_{halos}} \rangle \tag{2.5}$$

Naturally, $\langle \mathrm{DM_{IGM}} \rangle$ is redshift dependent and depends on our parameterization of $\langle \mathrm{DM_{halos}} \rangle$, i.e., on f_{hot} and r_{max}. At $z = z_{\mathrm{host}}$ for f_{hot}=0.75 and r_{max}=1, $\langle \mathrm{DM_{IGM}} \rangle \approx$ 54 $\mathrm{pc\,cm^{-3}}$, i.e. about 54% of $\langle \mathrm{DM_{cosmic}} \rangle$.

Adopting this value of $\langle \mathrm{DM_{IGM}} \rangle$ we can estimate $\mathrm{DM_{cosmic}}$ towards FRB190608 by combining it with our estimate of $\mathrm{DM_{halos}}$ (Fig. 2.1). This is presented as the blue, shaded curve in Fig. 2.5 using our fiducial estimate for $\mathrm{DM_{halos}}$ ($f_{\mathrm{hot}} = 0.75$, $r_{\mathrm{max}} = 1$). This $\mathrm{DM_{cosmic}}$ estimate is roughly 90 $\mathrm{pc\,cm^{-3}}$ less than $\mathrm{DM_{FRB,C}}$, and the discrepancy would be larger if one adopted a smaller $\mathrm{DM_{MW,halo}}$ value than $40\,\mathrm{pc\,cm^{-3}}$ (e.g. Keating & Pen, 2020). We have also computed $\mathrm{DM_{cosmic}}$ for different combinations of f_{hot} and r_{max} and show the results in Fig. 2.6.

First, we note that the $\mathrm{DM_{cosmic}}$ estimate is always lower than $\mathrm{DM_{FRB,C}}$. Second, it is not intuitive that the estimate is closer to $\mathrm{DM_{FRB,C}}$ when $f_{\mathrm{hot}} \approx 0$ (i.e., $\mathrm{DM_{halos}} \approx 0$). This arises from our definition of $\langle\mathrm{DM_{IGM}}\rangle$, i.e. $f_{\mathrm{hot}} = 0$ implies $\langle\mathrm{DM_{halos}}\rangle = 0$ or $\langle\mathrm{DM_{IGM}}\rangle = \langle\mathrm{DM_{cosmic}}\rangle$. As $\langle\mathrm{DM_{cosmic}}\rangle = 100\ \mathrm{pc\,cm^{-3}}$ is independent of f_{hot} and r_{max}, the estimate is close to $\mathrm{DM_{FRB,C}}$. For all higher f_{hot}, $\langle\mathrm{DM_{IGM}}\rangle$ is smaller and $\mathrm{DM_{halos}}$ is insufficient to add up to $\mathrm{DM_{FRB,C}}$. In summary, $\mathrm{DM_{halos}}$ is consistently lower than $\langle\mathrm{DM_{halos}}\rangle$ for the parameter range we explored. This results in the $\mathrm{DM_{cosmic}}$ thus estimated being systematically lower than $\mathrm{DM_{FRB,C}}$.

2.3.2.2 Cosmic web reconstruction

As described in Sec. 2.3.1, the localization of FRB 190608 to a region with SDSS coverage enables modeling of the DM contribution from individual halos along the line of sight. It also invites the opportunity to consider cosmic gas residing within the underlying, large-scale structure. Theoretical models predict shock-heated gas within the cosmic web as a natural consequence of structure formation (Cen & Ostriker, 1999; Davé et al., 2001), and indeed, FRBs offer one of the most promising paths forward in detecting this elusive material (Macquart et al., 2020).

Using the SDSS galaxy distribution within $400'$ of the FRB sightline, we employed the Monte Carlo Physarum Machine (MCPM) cosmic web reconstruction methodology introduced by Burchett et al. (2020) to map the large-scale structure intercepted by the FRB sightline. Briefly, the slime mold-inspired MCPM algorithm finds optimized network pathways between galaxies (analogous to food sources for the Physarum slime mold) in a statistical sense to predict the putative filaments in which they reside. The galaxies themselves occupy points in a three-dimensional (3D) space determined by their sky coordinates and the luminosity distances indicated by their redshifts. At each galaxy location, a simulated chemo-attractant weighted by the galaxy mass is emitted at every time step. Released into the volume are millions of simulated slime mold 'agents', which move at each time step in directions preferentially toward the emitted attractants. Thus, the agents eventually reach an equilibrium pathway network producing a connected 3D structure representing the putative filaments of the cosmic web. The trajectories of the agents are aggregated over hundreds of time steps to yield a 'trace', which in turn acts as a proxy for the local density at each point in the volume (see Burchett et al. 2020 for further details).

Our reconstruction of the structure intercepted by our FRB sightline is visualized in Fig. 2.7. The MCPM methodology simultaneously offers the features of 1) producing a continuous 3D density field defined even relatively far away from galaxies on Mpc scales and 2) tracing anisotropic filamentary structures on both large and small scales.

With the localization of FRB 190608 both in redshift and projected sky coordinates, we retrieved the local density as a function of redshift along the FRB sightline from the MCPM-fitted volume. The SDSS survey is approximately complete to galaxies with $M_* \geq 10^{10.0}\mathrm{M}_\odot$, which translates via abundance matching (Moster et al., 2013) to $M_{\mathrm{halo}} \geq 10^{11.5}\mathrm{M}_\odot$. Therefore, we only used galaxies and halos above these respective mass limits in our MCPM fits for the SDSS and Bolshoi-Planck datasets. This prevents us from extending the redshift range of our analysis beyond 0.1, as going further would require a higher mass cutoff and therefore a much sparser sample of galaxies on which to perform the analysis. On the lower end of the redshift scale, there are fewer galaxies more massive than $10^{10.0}\mathrm{M}_\odot$ (see Fig. 2.2) and therefore the MCPM fits are limited to $z > 0.018$. To translate the MCPM density metric ρ_{Phys} to a physical overdensity $\delta\rho/\rho_m$, we applied MCPM to the dark matter-only Bolshoi cosmological simulation, where the matter density ρ_m is known at each point. Rather than galaxies, we fed the MCPM locations and masses of dark matter halos (Behroozi et al., 2013). We then calibrated ρ_{Phys} to ρ/ρ_m as detailed by Burchett et al. (2020). This produces a mapping to physical overdensity, albeit less tightly constrained than that of Burchett et al. (2020) due to the sparser dataset we employ here. For densities $\rho \gtrsim \rho_m$, we estimate a roughly order of magnitude uncertainty in ρ/ρ_m derived along the line of sight. Fig. 2.8 shows the density relative to the average matter density as a function of redshift.

The electron number density $n_e(z)$ is obtained by multiplying $\bar{n}_e(z)$ from equation 2.2 with the MCPM estimate for ρ/ρ_{m}. Last, we integrate n_e to estimate $\mathrm{DM}_{\mathrm{IGM}}^{\mathrm{slime}}$ and recover $\mathrm{DM}_{\mathrm{IGM}}^{\mathrm{slime}} = 78\ \mathrm{pc\,cm^{-3}}$ for the redshift interval $z = [0.018, 0.1]$ (see Fig. 2.9a). $\mathrm{DM}_{\mathrm{IGM}}^{\mathrm{slime}}$ is nearly double the value of $\langle \mathrm{DM}_{\mathrm{IGM}} \rangle$ at $z = 0.1$ assuming $f_{\mathrm{hot}} = 0.75$ and $r_{\mathrm{max}} = 1$.

The Bolshoi-Planck mapping from the trace densities to physical overdensity includes an uncertainty of ~ 0.5 dex in each trace density bin. To estimate the uncertainty in $\mathrm{DM}_{\mathrm{IGM}}^{\mathrm{slime}}$, we first identify the peaks in Fig. 2.8. For all pixels within the full-width at half-maximum (FWHM) of each peak, we vary the relative density by a factor that does not exceed 0.5 dex. This factor is drawn from a uniform distribution in log space. Each peak was assumed to be independent and thus varied by different factors, and $\mathrm{DM}_{\mathrm{IGM}}^{\mathrm{slime}}$ was recomputed. From 100,000 such realizations of $\mathrm{DM}_{\mathrm{IGM}}^{\mathrm{slime}}$, we estimated a probability density function (PDF) (Fig. 2.9b). The 25th and 75th percentiles of this distribution are 75 $\mathrm{pc\,cm^{-3}}$ and 110 $\mathrm{pc\,cm^{-3}}$, respectively and the median value is 91 $\mathrm{pc\,cm^{-3}}$. For the redshift intervals excluded, we assume $n_e = \bar{n}_e$ and estimate an additional 16 $\mathrm{pc\,cm^{-3}}$ to $\mathrm{DM}_{\mathrm{IGM}}$ (8 $\mathrm{pc\,cm^{-3}}$ for $z < 0.018$ and 8 $\mathrm{pc\,cm^{-3}}$ for $z > 0.1$), increasing $\mathrm{DM}_{\mathrm{IGM}}$ to 94 $\mathrm{pc\,cm^{-3}}$. This is justified by comparing Fig. 2.2 and Fig. 2.8 to assess that there are no excluded overdensities that can contribute more than a few $\mathrm{pc\,cm^{-3}}$ over the average value. In conclusion, we estimate $\mathrm{DM}_{\mathrm{IGM}} = 94$ $\mathrm{pc\,cm^{-3}}$ with the 25th and 75th percentile bounds being 91 $\mathrm{pc\,cm^{-3}}$ and 126 $\mathrm{pc\,cm^{-3}}$.

With detailed knowledge of the IGM matter density, one can consider defining the boundary of a halo more precisely. A natural definition for the halo radius would be where the halo gas density and the IGM density are identical. Therefore, we tested whether the r_{max} obtained would significantly differ from the chosen value of unity, and thus produce substantially different $\mathrm{DM}_{\mathrm{halos}}$, for the intervening halos. We estimated r_{max} using this condition by setting the IGM density as the value obtained from the MCPM model at each halo redshift, yielding $r_{\mathrm{max}} \approx 1.3-2.2$ for the halos. $\mathrm{DM}_{\mathrm{halos}}$ estimated using these r_{max} values for the halos is ≈ 30 $\mathrm{pc\,cm^{-3}}$ as only the first two halos in Table 2.1 contribute. This is only slightly higher than the upper bound obtained previously for $r_{\mathrm{max}} = 1$ and therefore, we we choose to continue with the $\mathrm{DM}_{\mathrm{halos}}$ value initially estimated using $r_{\max} = 1$. Finally, our cosmic web reconstruction from the MCPM algorithm also allows us to refine our estimate of expected intervening galaxy halos in the KCWI FoV, $\langle n_{\rm halos}^{\rm KCWI} \rangle = 0.23$, presented in Section 2.2.1. Given the inferred overdensity as a function of redshift along the line of sight, $\rho/\rho_m(z)$, and the co-moving volume element given by the KCWI FoV as a function of redshift, $dV(z)$, we can then just scale $\langle n_{\rm halos}^{\rm KCWI} \rangle$ by $\alpha \equiv \frac{\int \rho/\rho_m(z) dV(z)\, dz}{\int dV(z)\, dz}$. In our case, we have obtained $\alpha = 1.66$, and then our refined $\langle n_{\rm halos}^{\rm KCWI} \rangle = 0.38$. This number is still small and, thus, fully consistent with a lack of intervening halos found in the KCWI FoV.

2.4 Cosmic contributions to the Rotation Measure and Temporal Broadening

We briefly consider the potential contributions of foreground galaxies to FRB 190608's observed temporal broadening and rotation measure. As evident in Table 2.1, there is only a single halo within 200 kpc of the sightline with $z \leq z_{\rm host}$. It has redshift $z = 0.09122$ and an estimated halo mass $M_{\rm halo} = 10^{12} {\rm M}_\odot$.

FRB 190608 exhibits a large, frequency-dependent pulse width $\tau = 3.3$ ms at 1.28 GHz (Day et al., 2020), which exceeds the majority of previously reported pulse widths (Petroff et al., 2016). Pulses are broadened when interacting with turbulent media. While we expect a scattering pulse width much smaller than a few milliseconds from the diffuse IGM alone (Macquart & Koay, 2013), we consider the possibility that the denser halo gas at $z = 0.09122$ contributes significantly to FRB 190608's intrinsic pulse profile. Here, we estimate the extent of such an effect, emphasizing that the geometric dependence of scattering greatly favors gas in intervening halos as opposed to the host galaxy.

Assuming the density profile as described

in Section 2.3.1 (extending to $r_{\rm max}$=1), the maximum electron density ascribed to the halo is at its impact parameter $b = 158\,{\rm kpc}$: $n_e \sim 10^{-4}\,{\rm cm}^{-3}$. Note that b is much greater than the impact parameter of the foreground galaxy of FRB 181112 (29 kpc, Prochaska et al., 2019) and indeed that of the host or the Milky Way with FRB 190608's sightline. The entire intervening halo can be thought of effectively as a "screen" whose thickness is the length the FRB sightline intersects with the halo, $\Delta L = 265$ kpc. We assume the turbulence is described by a Kolmogorov distribution of density fluctuations with an outer scale $L_0 = 1$ pc. This choice of L_0 arises from assuming stellar activity is the primary driving mechanism. To get an upper bound on the pulse width produced, we also assume the electron density is equal to 10^{-4} cm^{-3} for the entire length of the intersected sightline. Following the scaling relation in equation 1 from Prochaska et al. 2019, we obtain:

$$\begin{aligned}\tau_{1.4\ \rm GHz} <\ & 0.028\ {\rm ms}\ \alpha^{12/5}\left(\frac{\rm n_e}{10^{-4}\ {\rm cm^{-3}}}\right)^{12/5} \\ & \times\left(\frac{\Delta L}{265\ {\rm kpc}}\right)^{6/5}\left(\frac{L_0}{1\ {\rm pc}}\right)^{-4/5}\end{aligned} \tag{2.6}$$

Here, α is a dimensionless number that encapsulates the root mean-squared amplitude of the density fluctuations and the volume-filling fraction of the turbulence. It is typically of order unity. We note that our chosen value of L_0 presents an upper limit on the scattering timescale. Were $L_0 \gg 1$ pc (e.g. if driven by AGN jets), $\tau \ll 0.03$ ms. The observed scattering timescale exceeds our conservative upper bound by two orders of magnitude. One would require $n_e > 6 \times 10^{-4}$ cm^{-3} to produce the observed pulse width. This exceeds the maximum density estimation through the halo, even for the relatively flat and high $f_{\rm hot}$ assumed. We thus conclude that the pulse broadening for FRB 190608 is not dominated by intervening halo gas.

FRB 190608 also has a large estimated $\mathrm{RM_{FRB}} = 353 \pm 2\,\mathrm{rad\ m^{-2}}$ (Day et al., 2020). We may estimate the RM contributed by the intervening halo, under the assumption that its magnetic field is characterized by the equipartition strength magnetic fields in galaxies ($\sim 10\ \mu G$) (Basu & Roy, 2013). We note that this exceeds the upper limit imposed on gas in the halo intervening FRB 181112 (Prochaska et al., 2019).

We estimate:

$$\begin{aligned} \mathrm{RM_{halos}} = 0.14\ \mathrm{rad\ m^{-2}} \left(\frac{\mathrm{B}_{\parallel}}{10\ \mu\mathrm{G}}\right) \left(\frac{\Delta L}{265\ \mathrm{kpc}}\right) \\ \times \left(\frac{n_e}{10^{-4}\ \mathrm{cm^{-3}}}\right) \end{aligned} \tag{2.7}$$

and conclude that it is highly unlikely that the RM contribution from intervening halos dominates the observed quantity.

2.5 Concluding Remarks

To summarize, we have created a semi-empirical model of the matter distribution in the foreground universe of FRB 190608 using spectroscopic and photometric data from the SDSS database and our own KCWI observations. We modeled the virialized gas in intervening halos using a modified NFW profile and used the MCPM approach to estimate the ionized gas density in the IGM. Table 2.3 summarizes the estimated DM contributions from each of the individual foreground components. Adding $\langle \mathrm{DM_{halos}} \rangle$ and $\mathrm{DM_{IGM}}$ for this sightline, we infer $\mathrm{DM_{cosmic}} = 98 - 154\mathrm{pc\,cm^{-3}}$, which is comparable

Table 2.3: Contributions to DM_{FRB} from foreground components

Component	Sub component	Notation	Value ($pc\,cm^{-3}$)	Comments
Host Galaxy	ISM	$DM_{host,ISM}$	47-117	From Chittidi et al. (2020)
	Halo	$DM_{host,halo}$	15-41	From Chittidi et al. (2020)
Foreground cosmos	Intervening halos	DM_{halos}	7-28	Using SDSS spectroscopic galaxies and 0.16 dex scatter in M*
		$\langle DM_{halos} \rangle$	45	Average assuming the Aemulus HMF and Planck 15 cosmology
	Diffuse IGM	DM_{IGM}	91-126	25th and 75th percentiles using the MCPM method
		$\langle DM_{IGM} \rangle$	54	Average assuming the Aemulus HMF and Planck 15 cosmology
Milky Way	ISM	$DM_{MW,ISM}$	38	From Cordes & Lazio (2003a)
	Halo	$DM_{MW,halo}$	40	From Prochaska & Zheng (2019)

to $\langle \mathrm{DM_{cosmic}} \rangle = 100\ \mathrm{pc\,cm^{-3}}$. The majority of $\mathrm{DM_{cosmic}}$ is accounted for by the diffuse IGM, implying that most of the ionized matter along this sightline is not in virialized halos. We found only 4 galactic halos within 550 kpc of the FRB sightline and only 1 halo within 200 kpc. We found no foreground object in emission from our ~ 1 sq. arcmin KCWI coverage and no galaxy group or cluster having an impact parameter of less than its virial radius with our FRB sightline.

We also find it implausible that the foreground structures are dense enough to account for either the pulse broadening or the large rotation measure of the FRB. We expect the progenitor environment and the host galaxy together are the likely origins of both Faraday rotation and turbulent scattering of the pulse (discussed in further detail by Chittidi et al., 2020).

The results presented here are not the first attempt to measure $\mathrm{DM_{cosmic}}$ along FRB sightlines by accounting for density structures. Li et al. (2019) estimated $\mathrm{DM_{cosmic}}$ (termed $\mathrm{DM_{IGM}}$ in their paper) for five FRB sightlines, making use of the 2MASS Redshift Survey group catalog (Lim et al., 2017) to infer the matter density field along their lines of sight. They assumed NFW profiles around each identified group. This enabled them to estimate the DM contribution from intervening matter for low DM ($\mathrm{DM_{cosmic}} + \mathrm{DM_{host}} < 100\ \mathrm{pc\,cm^{-3}}$) FRBs. Our approach differs in the methods used to estimate $\mathrm{DM_{cosmic}}$. The precise localization of FRB 190608 allows us to estimate $\mathrm{DM_{halos}}$ and $\mathrm{DM_{IGM}}$ separately. Li et al. (2019) were limited by the large uncertainties ($\sim 10'$) in the FRB position and therefore their estimates of $\langle \mathrm{DM_{cosmic}} \rangle$ depended on the assumed host galaxy within the localization regions. Furthermore, the MCPM model estimates the cosmic density field, and thus the ionized gas density of the IGM, due to filamentary large-scale structure. We note that our estimates of n_e from the MCPM model in overdense regions is similar to their reported values ($10^{-6} - 10^{-5}$ cm^{-3}). This naturally implies our $\mathrm{DM}_{\mathrm{cosmic}}$ estimates are of the same order of magnitude around $z = 0.1$ as their estimate. Together with the results presented by Chittidi et al. (2020), our study represents a first of its kind: an observationally driven, detailed DM budgeting along a well-localized FRB sightline. We have presented a framework for using FRBs as quantitative probes of foreground ionized matter. Although aspects of this framework carry large uncertainties at this juncture, the methodology should become increasingly precise as this nascent field of study matures. For instance, our analysis required spectroscopic data across a wide area (i.e. a few square degrees) around the FRB, which enabled us to constrain the individual contributions of halos and also to model the cosmic structure of the foreground IGM. An increase in sky coverage and depth of spectroscopic surveys would enable the use of cosmic web mapping tools like the MCPM estimator with higher precision and on more FRB sightlines. Upcoming spectroscopic instruments such as DESI and 4MOST will map out cosmic structure in greater detail and will, no doubt, aid in the use of FRBs as cosmological probes of matter.

We expect FRBs to be localized more frequently in the future, thanks to thanks to continued improvements in high-time resolution backends and real-time detection systems for radio interferometers. One can turn the analysis around and use the larger set of localized FRBs to constrain models of the cosmic web in a region and possibly perform tomographic reconstructions of filamentary structure. Alternatively, by accounting for the DM contributions of galactic halos and diffuse gas, one may constrain the density and ionization state of matter present in intervening galactic clusters or groups. Understanding the cosmic contribution to the FRB dispersion measures can also help constrain progenitor theories by setting upper limits on the amount of dispersion measure arising from the region within a few parsecs of the FRB. We are at the brink of a new era of cosmology with new discoveries and constraints coming from FRBs.

Acknowledgments: Authors S.S., J.X.P., N.T., J.S.C. and R.A.J., as members of the Fast and Fortunate for FRB Follow-up team, acknowledge support from NSF grants AST-1911140 and AST-1910471. J.N.B. is supported by NASA through grant number HST-AR15009 from the Space Telescope Science Institute, which is operated by AURA, Inc., under NASA contract NAS5-26555. This work is supported by the Nantucket Maria Mitchell Association. R.A.J. and J.S.C. gratefully acknowledge the support of the Theodore Dunham, Jr. Grant of the Fund for Astrophysical Research. K.W.B., J.P.M, and R.M.S. acknowledge Australian Research Council (ARC) grant DP180100857. N.T. acknowledges support by FONDECYT grant 11191217. The Australian Square Kilometre Array Pathfinder is part of the Australia Telescope National Facility which is managed by CSIRO. Operation of ASKAP is funded by the Australian Government with support from the National Collaborative Research Infrastructure Strategy. ASKAP uses the resources of the Pawsey Supercomputing Centre. Establishment of ASKAP, the Murchison Radio-astronomy Observatory and the Pawsey Supercomputing Centre are initiatives of the Australian Government, with support from the Government of Western Australia and the Science and Industry Endowment Fund. We acknowledge the Wajarri Yamatji as the traditional owners of the Murchison Radio-astronomy Observatory site. Spectra were obtained at the W. M. Keck Observatory, which is operated as a scientific partnership among Caltech, the University of California, and the National Aeronautics and Space Administration (NASA). The Keck Observatory was made possible by the generous financial support of the W. M. Keck Foundation. The authors recognize and acknowledge the very significant cultural role and reverence that the summit of Mauna Kea has always had within the indigenous Hawaiian community. We are most fortunate to have the opportunity to conduct observations from this mountain.

.1 Cosmic diffuse gas fraction

Central to an estimate of $\mathrm{DM}_{\mathrm{cosmic}}$ is the fraction of baryons that are diffuse and ionized in the universe f_d. We have presented a brief discussion of f_d in previous works (Prochaska & Zheng, 2019; Macquart et al., 2020) and provide additional details and an update here.

To estimate $f_d(z)$, we work backwards by defining and estimating the cosmic components that do not contribute to $\mathrm{DM}_{\mathrm{cosmic}}$. These are:

1. Baryons in stars, ρ_{stars}. This quantity is estimated from galaxy surveys and inferences of the stellar initial mass function (Madau & Dickinson, 2014).

2. Baryons in stellar remnants and brown dwarfs, ρ_{remnants}. This quantity was estimated by Fukugita (2004) to be $\approx 0.3\rho_{\mathrm{stars}}$ at $z = 0$. We adopt this fraction for all cosmic time.

3. Baryons in neutral atomic gas, ρ_{HI}. This is estimated from 21 cm surveys.

4. Baryons in molecular gas, ρ_{H_2}. This is estimated from CO surveys.

One could also include the small contributions from heavy elements, but we ignore this because it is a value smaller than the uncertainty in the dominant components.

Altogether, we define

$$f_d \equiv 1 - \frac{\rho_{\mathrm{stars}}(z) + \rho_{\mathrm{remnants}}(z) + \rho_{\mathrm{ISM}}(z)}{\rho_b(z)} \tag{.8}$$

where we have defined $\rho_{\mathrm{ISM}} \equiv \rho_{\mathrm{HI}} + \rho_{\mathrm{H}_2}$. Fukugita (2004) has estimated $\rho_{\mathrm{ISM}}/\rho_{\mathrm{stars}} \approx 0.38$ at $z = 0$ and galaxy researchers assert that this ratio increases to unity by $z = 1$ (e.g. Tacconi et al., 2020). For our formulation of f_d, we assume $\rho_{\mathrm{ISM}}(z)/\rho_{\mathrm{stars}}(z)$ increases as a quadratic function with time having values 0.38 and 1 at $z = 0$ and 1 respectively, and 0.58 at the half-way time. The quantity is then taken to be unity at $z > 1$. Figure .10a shows plots of ρ_{stars} and ρ_{ISM} versus redshift, and Figure .10b presents f_d. Code that incorporates this formalism is available in the FRB repository[2].

f_d, therefore, does not have a simple analytical expression describing it as a function of redshift. One can always approximate f_d as a polynomial expansion in z. For $z < 1$, one can obtain a reasonable approximation (relative error $< 5\%$) by truncating up to the fourth order in z:

$$f_d(z) \approx 0.843 + 0.007z - 0.046z^2 + 0.106z^3 - 0.043z^4 \tag{.9}$$

[2]https://github.com/FRBs/FRB

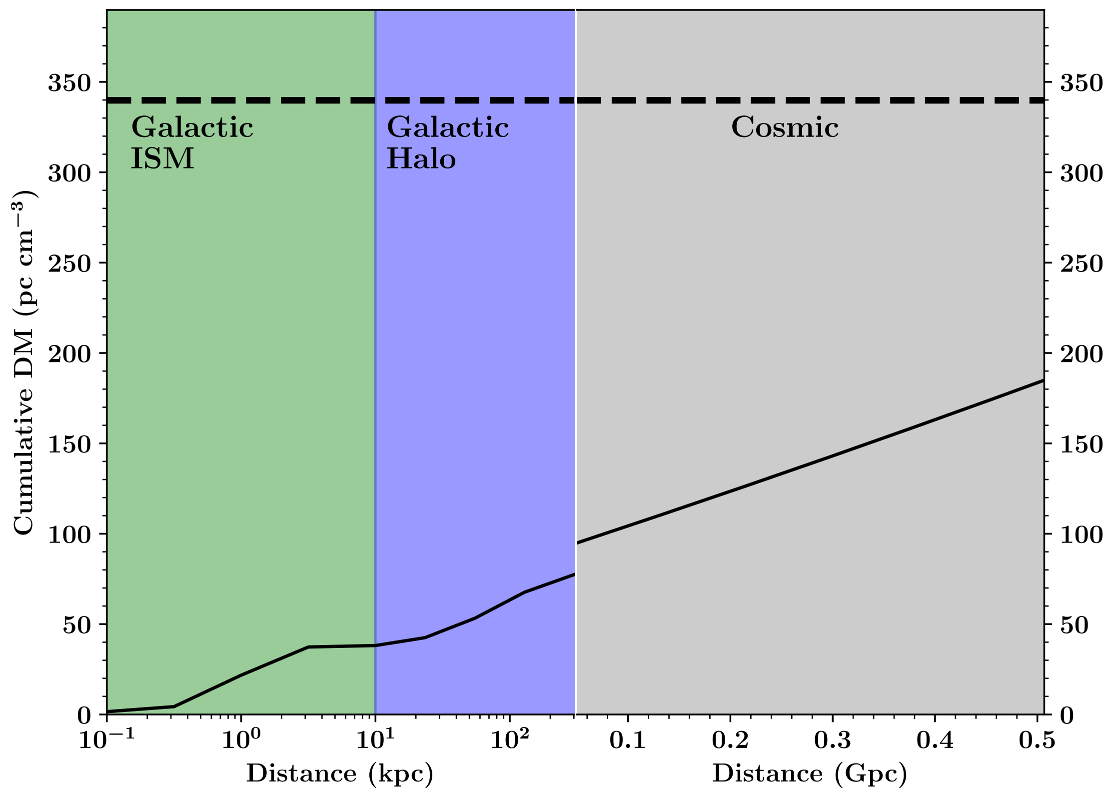

Figure 2.1: **The cumulative FRB dispersion measure for FRB 190608**. The dashed line corresponds to the $\mathrm{DM_{FRB}} = 362.16\,\mathrm{pc\,cm^{-3}}$ reported for the FRB (Day et al., 2020), which is at the highest distance shown ($\approx 0.5\,\mathrm{Gpc}$). The solid curve is an estimate of the cumulative DM moving out from Earth towards the FRB. The Milky Way's ISM (green; model of Cordes & Lazio, 2003a) and halo (blue; model of Prochaska & Zheng, 2019) together may contribute $\approx 100\ \mathrm{pc\,cm^{-3}}$. If the foreground cosmic web (grey) contributes the expected average (Equation 2.2), this adds an additional $\approx 100\ \mathrm{pc\,cm^{-3}}$ as modeled. Note that the horizontal axis is discontinuous at the Halo-Cosmic interface and this is the reason for a discontinuous cumulative DM. The difference between the solid and dashed lines at the FRB is $\approx 160\ \mathrm{pc\,cm^{-3}}$ and is expected to be attributed to the host galaxy and/or an above average contribution from the cosmic web (e.g. overdensities in the host galaxy foreground).

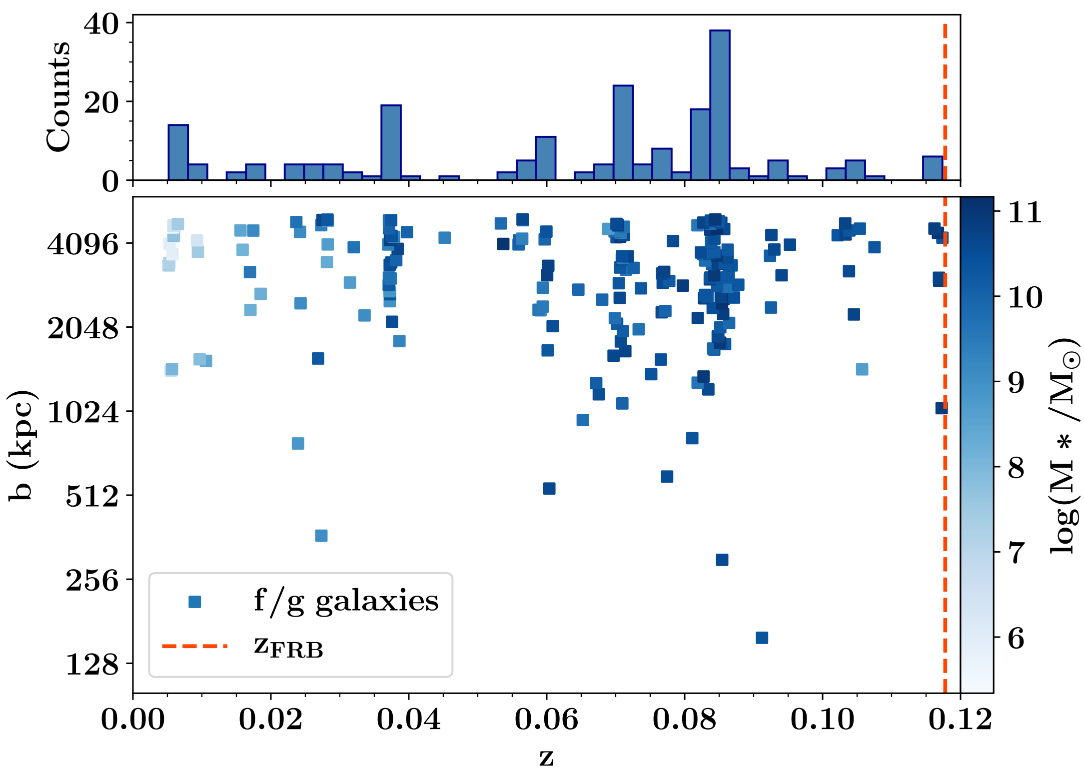

Figure 2.2: **The spatial distribution of foreground galaxies**. *(Bottom)* A scatter plot of foreground galaxy redshifts, z, and impact parameters, b. The points are colored according to the estimated stellar masses. The red dashed-line indicates the FRB host redshift. *(Top)* A histogram of the redshifts. The 'spikes' in the distribution, e.g. at $z \sim 0.08$, indicate overdensities in the underlying cosmic web structure.

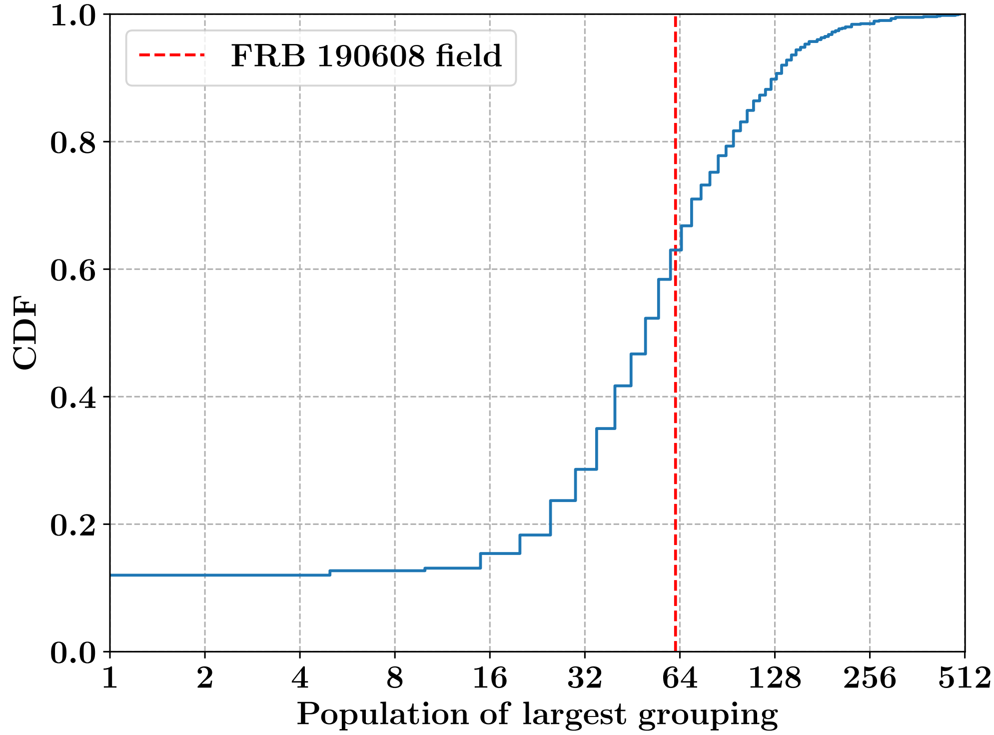

Figure 2.3: **Grouping population sizes in SDSS fields**. A cumulative histogram of the sizes of the most populous redshift groupings in 1000 random SDSS fields. Each field was searched for galaxies more massive than $10^{9.3}$ $M_{\odot}$ with spectra within 5 Mpc of a sightline passing through the center. The groupings are computed using a Mean-Shift algorithm with bandwidth Δz =0.005. Their centroids all lie between z = 0.02 and $z_{\rm host}$. The most populous redshift grouping found in the FRB field at $z \sim 0.08$ is indicated by the dashed, red line. At the 63$^{\rm rd}$ percentile, the FRB field does not have rare overdensities in its foreground.

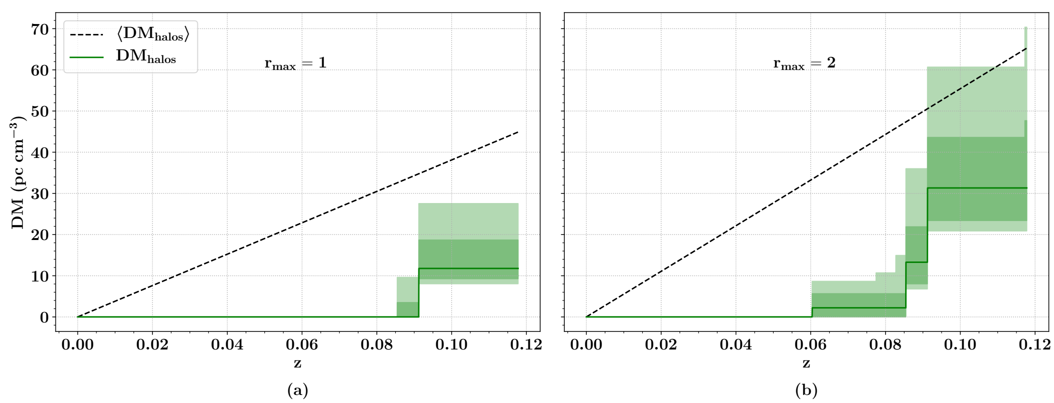

Figure 2.4: DM_{halos} **vs redshift**. The black line represents $\langle DM_{halos} \rangle$, i.e., the average DM from halos using the Aemulus halo mass function (ignoring the IGM). The solid green line is our estimate of DM_{halos}, the DM contribution from intervening halos of galaxies found in SDSS and assuming a hot gas fraction $f_{hot} = 0.75$. The dark green shaded region is obtained by varying the stellar masses of each of the intervening halos by 0.1 dex, which modulates the adopted halo mass. This is representative of the uncertainty in DM propagated from stellar mass estimation. The lighter green shaded region is obtained by similarly varying the stellar masses by 0.16 dex and it is representative of the uncertainty in DM propagated from the scatter in the SHMR. This calculation was performed for two values of the dimensionless radial extent of the halo's matter distribution, r_{max}: 1 (*left*) and 2 (*right*). Using the central measures of stellar mass and the SHMR, the intervening galaxies contribute DM_{halos} less than the expected cosmic average, $\langle DM_{halos} \rangle$, and do not exceed 50 $\mathrm{pc\,cm^{-3}}$.

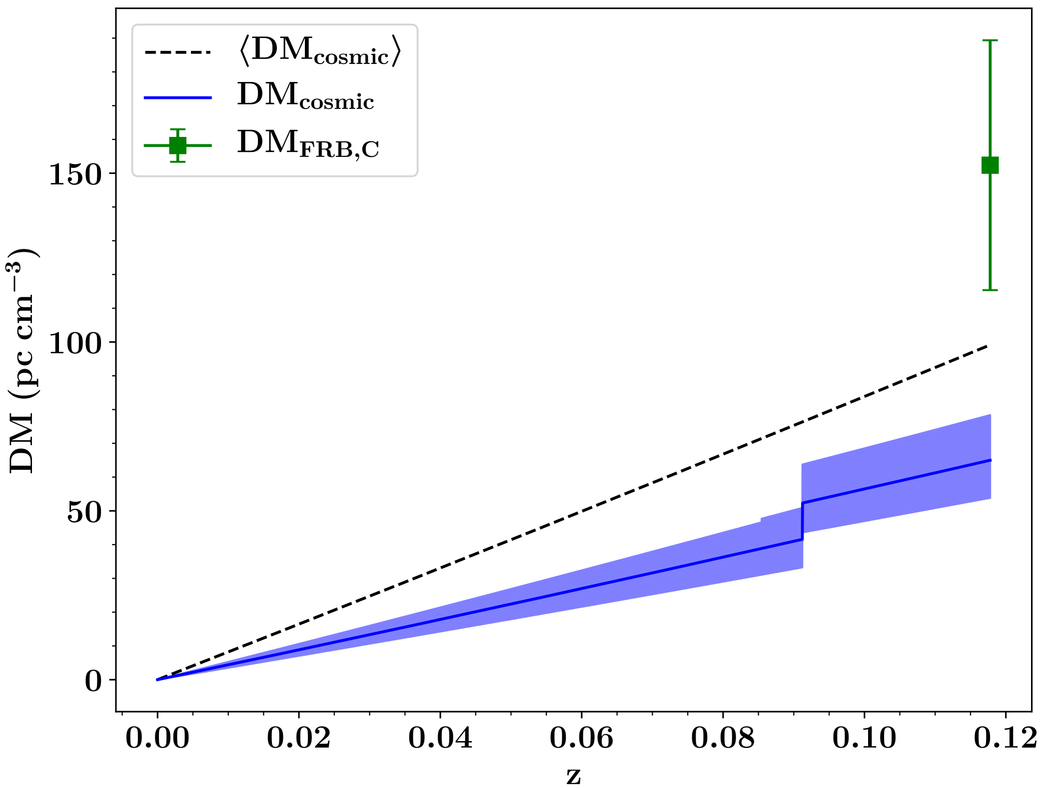

Figure 2.5: $\mathrm{DM_{cosmic}}$ **vs redshift**. The solid blue line corresponds to $\mathrm{DM_{cosmic}} = \mathrm{DM_{halos}} + \langle \mathrm{DM_{IGM}} \rangle$ with $f_{\rm hot} = 0.75$ and $r_{\rm max} = 1$. The shaded region represents the quadrature sum of uncertainties in $\mathrm{DM_{halos}}$ (allowing for 0.1 dex variation in stellar mass) and the IGM (taken to be 20% of $\mathrm{DM_{IGM}}$). The green point is $\mathrm{DM_{FRB,C}}$ (i.e. $\mathrm{DM_{FRB}} - \mathrm{DM_{MW}} - \mathrm{DM_{host}}$). The errorbars correspond to the uncertainty in $\mathrm{DM_{host}}$, which is 37 $\mathrm{pc\,cm^{-3}}$. The black line represents $\langle \mathrm{DM_{cosmic}} \rangle$.

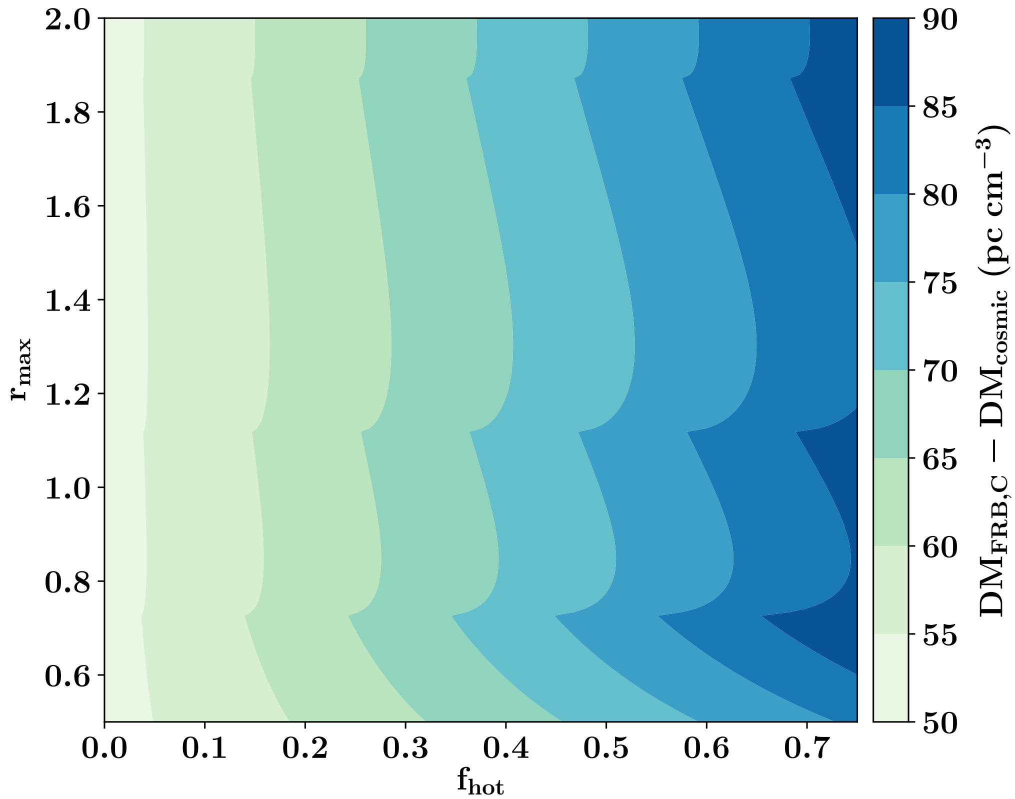

Figure 2.6: $\mathrm{DM_{cosmic}}$ **compared to** $\mathrm{DM_{FRB,C}}$ **as a function of halo model parameters**. Here, $\mathrm{DM_{cosmic}}$ is defined as $\mathrm{DM_{halos}}+\langle\mathrm{DM_{IGM}}\rangle$ and depends on two key parameters, $f_{\rm hot}$ and $r_{\rm max}$. $f_{\rm hot}$ is the fraction of baryonic matter present as hot gas in halos, and $r_{\rm max}$ is the radial extent in units of r_{vir} up to which baryons are present in the halo. At low $f_{\rm hot}$ and $r_{\rm max}$ values, $\mathrm{DM_{halos}}$ is small and $\mathrm{DM_{cosmic}} \approx \langle\mathrm{DM_{IGM}}\rangle \approx \langle\mathrm{DM_{cosmic}}\rangle$. Towards higher $f_{\rm hot}$ and $r_{\rm max}$ values, $\langle\mathrm{DM_{IGM}}\rangle$ decreases and $\mathrm{DM_{halos}}$ increases. However, $\mathrm{DM_{halos}} < \langle\mathrm{DM_{halos}}\rangle$. Thus $\mathrm{DM_{cosmic}}$ decreases further compared to $\mathrm{DM_{FRB,C}}$. In summary, $\mathrm{DM_{cosmic}}$ estimated this way being small is a reflection of the lower than average contribution from $\mathrm{DM_{halos}}$.

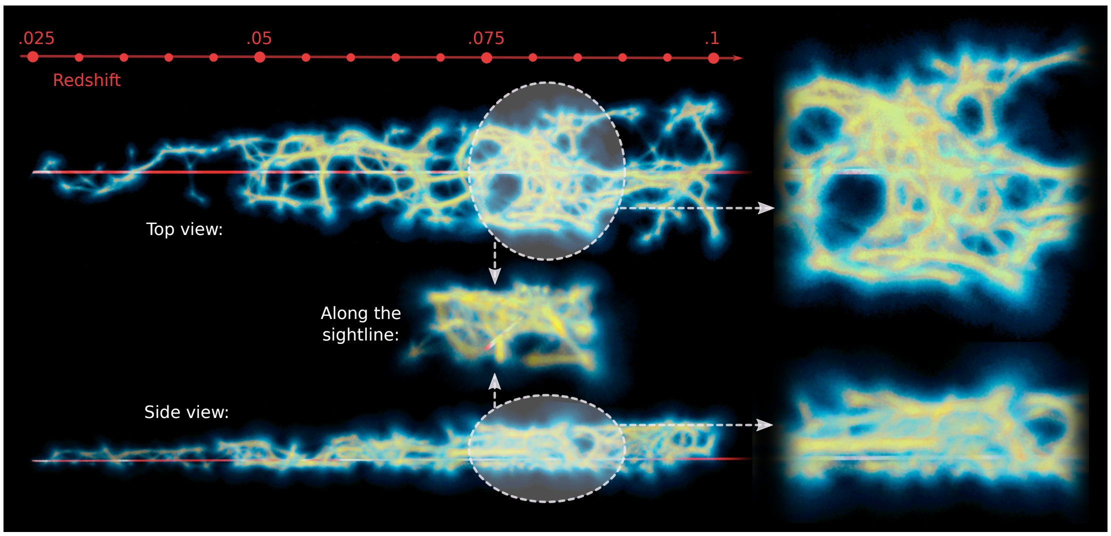

Figure 2.7: **A 3D model of the cosmic web in physical coordinates reconstructed using the MCPM** *Left, top*: The red line passing through the web represents the FRB sightline where light is assumed to travel from right to left. The cosmic web reconstruction (Elek et al., 2021) is shown color-coded by the steady-state Physarum particle trace density (yellow being high and black being low). The red line with ticks along the top shows the horizontal scale of the reconstruction in redshift. In the vertical direction, the reconstructed region of the web spans an angular diameter of $800'$ on the sky. *Left, bottom*: A rotated view of the reconstruction. The FRB sightline falls within a narrow strip of the SDSS footprint, and the vertical size in the side view is smaller than that in the top view. *Left, center*: A view along the sightline (which is again visible in red) of a high-density region enclosed by the translucent circles in the top and side views. *Right*: Two close-up views of the locations indicated by the circles on the left.

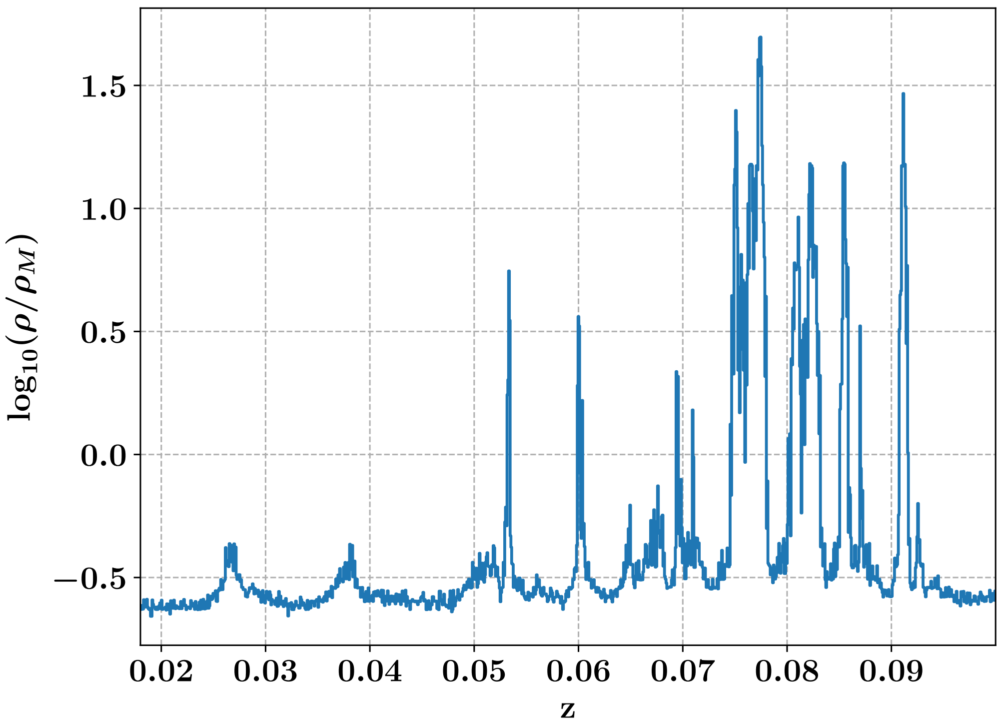

Figure 2.8: **Cosmic web density estimate from MCPM.** We show the MCPM-derived cosmic overdensity as a function of redshift along the line of sight to FRB 190608. We first produced our cosmic web reconstruction from SDSS galaxies within 400 arcmin of the sightline and then calibrated the MCPM trace (see text) with the cosmic matter density from the Bolshoi-Planck simulation. Note that there are apparently no galaxy halos ($\rho > 100\rho_{\rm m}$) captured here, although several density peaks arise from large-scale structure filaments. We in turn use the 3D map from MCPM to model the diffuse IGM gas and produce $\mathrm{DM_{IGM}}$ estimates.

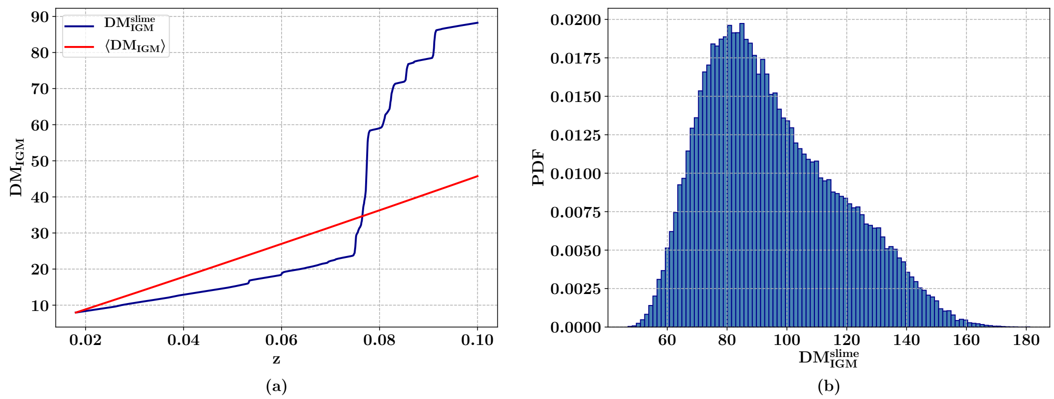

Figure 2.9: DM_{IGM}^{slime} **from MCPM density estimate.** *(Left)* A comparison of DM_{IGM} obtained from the MCPM analysis (blue) and $\langle DM_{IGM} \rangle$ (red) assuming $f_{hot} = 0.75$ and $r_{max} = 1$. Below z = 0.018, where the MCPM density estimate is not available, DM_{IGM}^{slime} is assumed to be equal to $\langle DM_{IGM} \rangle$. At z = 0.1, DM_{IGM}^{slime} is nearly twice $\langle DM_{IGM} \rangle$. *(Right)* The DM_{IGM}^{slime} PDF estimated from accounting for the uncertainties in the Bolshoi-Planck mapping from particle trace densities to physical overdensities. The full-width at half-maximum (FWHM) of each density peak is independently varied by a factor within 0.5 dex and a cumulative DM is computed. This estimate of the PDF is obtained from 100,000 realizations of DM_{IGM}^{slime}. $DM_{IGM}^{slime} = 88$ pc cm^{-3} for $z \leq 0.1$, and its distribution is asymmetric with a standard deviation of ~ 15 pc cm^{-3}.

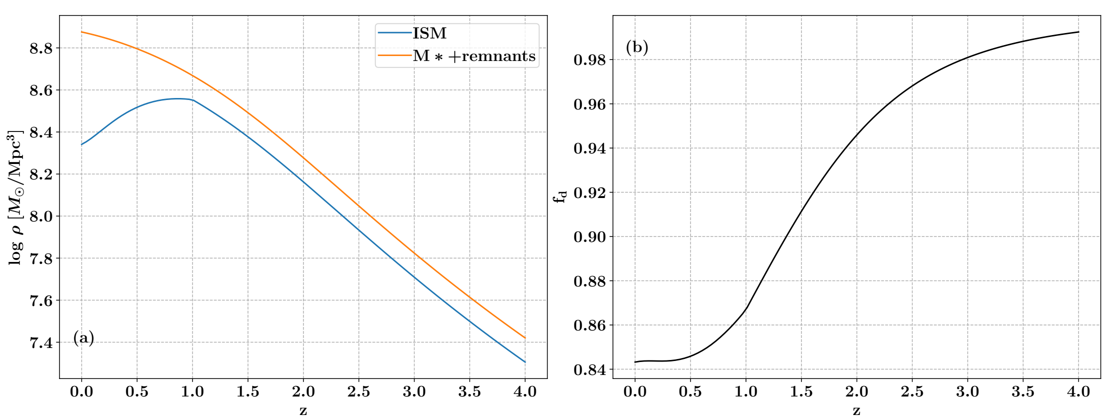

Figure .10: (a) Estimates of the stellar and ISM mass densities in galaxies versus redshift. (b) Estimate of f_d versus redshift.

Chapter 3

Estimating the contribution of foreground halos to the FRB 180924 dispersion measure

Abstract

Probing the Cosmic Web with Fast Radio Bursts

by

H. S. Sunil Simha

Fast Radio Burst (FRB) dispersion measures (DMs) record the presence of ionized baryons that are otherwise invisible to other techniques enabling resolution of the matter distribution in the cosmic web. In this work, we aim to estimate the contribution to FRB 180924 DM from foreground galactic halos. Localized by ASKAP to a massive galaxy, this sightline is notable for an estimated cosmic web contribution to the DM ($\mathrm{DM_{cosmic}}$= 220 $\mathrm{pc\,cm^{-3}}$), which is less than the average value at the host redshift (z = z_{FRB}) estimated from the Macquart relation (280 $\mathrm{pc\,cm^{-3}}$). In the favored models of the cosmic web, this suggests few intersections with foreground halos at small impact parameters ($\lesssim$ 100 kpc). To test this hypothesis, we carried out spectroscopic observations of the field galaxies within ∼1 arcmin of the sightline with VLT/MUSE and Keck/LRIS. Furthermore, we developed a probabilistic methodology that leverages photometric redshifts derived from wide-field DES and WISE imaging. We conclude that there is no galactic halo that closely intersects the sightline and also that the net DM contribution from halos, $\mathrm{DM_{halos}} < 45$ $\mathrm{pc\,cm^{-3}}$ (95 % c.l.). This value is lower than the $\mathrm{DM_{halos}}$ estimated from an "average" sightline (121 $\mathrm{pc\,cm^{-3}}$) using the Planck ΛCDM model and the Aemulus halo mass function and reasonably explains its low $\mathrm{DM_{cosmic}}$ value. We conclude that FRB 180924 represents the predicted majority of sightlines in the universe with no proximate foreground galactic halos. Our framework

lays the foundation for a comprehensive analysis of FRB fields in the near future.

3.1 Introduction

Fast Radio Bursts (FRBs) are millisecond-duration, energetic ($\sim 10^{44}$ erg) radio transient events. In recent years, numerous FRBs have been localized and most FRBs are confirmed to be extragalactic (e.g. Lorimer et al., 2007; Bannister et al., 2019; Tendulkar et al., 2017; Law et al., 2020). Although their generation mechanism is yet unknown, FRBs represent a new tool in the repertoire of an observational cosmologist to probe matter and cosmological structure in the universe. Astronomers have used quasar absoprtion lines to study neutral gas in the circumgalactic medium (e.g. Bahcall & Spitzer, 1969; Chen & Tinker, 2008; Prochaska et al., 2011; Tumlinson et al., 2013; Werk et al., 2014; Wilde et al., 2021) for the last several decades. Now, with their unique transient signal, FRBs enable us to capture information about all ionized matter along their lines-of-sight, thus unlocking an opportunity to study previously invisible gas in the universe. One of the measurable properties of FRBs is their dispersion measure (DM), which is the cosmological-scale-factor-weighted line of sight integral of electron density. Even with a handful of localized FRBs, Macquart et al. (2020) were able to show that the observed FRB DMs are consistent with the expected matter distribution in a ΛCDM universe, thus conclusively resolving the Missing Baryon Problem. While their work "found" the Missing Baryons, the next phase of research is to precisely locate them within the cosmic web. Specifically, we aim to develop the framework to utilize these data and reconstruct the distribution of matter along the sightlines.

Being an integral, one can split the FRB DM into disjoint summative parts corresponding to each "electron reservoir" along the line of sight, namely the host galaxy and its halo; intervening foreground halos and cosmic web filaments; and the Milky Way including its gaseous halo, i.e.

$$\mathrm{DM_{FRB}} = \mathrm{DM_{host}} + \mathrm{DM_{cosmic}} + \mathrm{DM_{MW}} \tag{3.1}$$

A full characterization of $\mathrm{DM_{FRB}}$ requires detailed information on the host (e.g. Chittidi et al., 2020) and the intervening cosmic web structures. Simha et al. (2020) performed such an analysis on the sightline of FRB 190608 owing to the favorable location of the FRB in the SDSS spectroscopic footprint. This provided detailed information on the redshifts of foreground galaxies, allowing for a nearly complete characterization of their DM contributions (although with significant uncertainty) and also the contribution from the diffuse intergalactic medium (IGM). In general, if a FRB host is located at low redshifts ($z < 0.05$), one could use just the 2MASS Redshift Catalog (Huchra et al., 2012) to perform the same analysis. However, the vast majority of localized FRBs to date fall outside the extant SDSS coverage, and therefore one would require extensive new spectroscopic observations. In this work, we explore the application of photometric redshifts combined with sparse spectroscopy to estimate the DM contributions of foreground halos, $\mathrm{DM_{halos}}$, for one such sightline: FRB 180924.

FRB 180924 was the first apparently non-repeating FRB to be discovered and localized by the Australian Square-Kilometer Array Pathfinder (ASKAP) in September 2018 (Bannister et al., 2019) with a measured $\mathrm{DM_{FRB}} = 362.16\ \mathrm{pc\,cm^{-3}}$. Its massive, moderately star-forming host galaxy ($z = z_{\mathrm{FRB}}$) is located in the footprint of the first data release of the Dark Energy Survey (DES DR1 Abbott et al., 2018). While its $\mathrm{DM_{host}}$ is uncertain, if one assumes it to be $66\ \mathrm{pc\,cm^{-3}}$ in the host rest frame (Bannister et al., 2019); uses the NE2001 model (Cordes & Lazio, 2003a) for the Milky Way disk (41 $\mathrm{pc\,cm^{-3}}$); and 50 $\mathrm{pc\,cm^{-3}}$ for the Milky Way halo gas, the remainder of the DM is attributed to the cosmic web: $\mathrm{DM_{cosmic,FRB}} \approx 220\ \mathrm{pc\,cm^{-3}}$. This is lower than the mean expected [1] $\mathrm{DM_{cosmic}}$ value at the host redshift ($\langle \mathrm{DM_{cosmic}} \rangle = 280\ \mathrm{pc\,cm^{-3}}$), suggesting either a less than average foreground matter density, or our adopted values for $\mathrm{DM_{host}}$ or $\mathrm{DM_{MW}}$ are too large. Of course, the average value is not representative of all sightlines and there is naturally some scatter (Macquart et al., 2020). For a given redshift, the distribution of $\mathrm{DM_{cosmic}}$ is skewed towards lower than average DM. This is because most of the sightlines in the universe rarely intersect any galactic halo at low impact parameter ($\lesssim 50$ kpc). In this work, we test whether the lower than average $\mathrm{DM_{cosmic}}$ is consistent with this paradigm, i.e. if there are indeed no foreground galactic halos in close proximity to it. We also outline a framework to estimate, based on photometry alone, the halo contribution to $\mathrm{DM_{FRB}}$: $\mathrm{DM_{halos}}$.

This paper is organized as follows: we describe the data collected in section 3.2, our methods in estimating $\mathrm{DM_{halos}}$in section 3.3, our results in section 3.4 and make concluding remarks in section 3.5. We assume a ΛCDM cosmology with the cosmological parameters derived from the 2015 Planck dataset (Planck Collaboration et al., 2016a) for all our calculations.

[1] Expectation value obtained by assuming a flat, ΛCDM cosmology with Planck 2015 parameters and that the diffuse gas is fully ionized. The fraction of baryons in the universe constituting diffuse gas is obtained by subtracting the fractions for the dense components: stars (Fukugita, 2004) and the ISM (Madau & Dickinson, 2014).

3.2 Data

3.2.1 Photometry

We obtained photometric data in the $grizY$ bands for all sources within $15'$ of FRB 180924 from DES DR1 (Abbott et al., 2018, 95% complete to $r = 23.35$). This was supplemented with photometry from the Wide-field Infrared Survey Explorer (WISE; Wright et al., 2010) database where available. At $z = 0.03$, $15'$ corresponds to 560 kpc in projected physical distance. This is approximately the virial radius of a 10^{13} $M_\odot$ dark matter halo with a modified NFW profile (Prochaska & Zheng, 2019). Thus we hoped to capture all galaxy halos that are less massive than this limit at $z > 0.03$. We did not find any galaxy cluster or group catalog that covers this FRB sightline either and so our analysis is blind to halos of that mass scale.

To remove stars from the photometric catalog, we used the morphology-based classifier flag `class_star_r` from the DES DR1 database. Extended objects like galaxies have flag values closer to zero while point sources tend to lie closer to unity. We excluded objects whose r-band magnitudes were less than 17 and the flag value was above 0.9. To further exclude stars, we cross matched the remaining DES objects with stars having measured parallaxes (`parallax_over_error`$>$ 1) in the main GAIA DR3 catalog (Gaia Collaboration et al., 2016, 2020). The DES (and WISE) magnitudes obtained are the elliptical aperture magnitude based on the Kron radius (i.e. the `auto_mag` columns in the main DES DR1 catalog; see Table 3.1 and 3.2).

Table 3.1: Catalog of photometry from DES for galaxies in the FRB 180924 field (Part 1).

DES ID	RA	Dec	g	r	i	z	Y
	deg	deg	mag	mag	mag	mag	mag
209914488	326.10521	-40.90023	21.62	20.54	20.14	19.85	19.81
209914542	326.10163	-40.89981	25.05	24.54	23.92	23.46	24.77
209914588	326.11102	-40.90060	23.19	22.63	22.46	22.14	23.08
209914804	326.10812	-40.90395	26.72	24.57	23.60	22.91	22.08
209914529	326.11133	-40.89956	24.38	24.29	23.57	23.61	22.95

Table 3.2: Catalog of photometry from WISE for galaxies in the FRB 180924 field (Part 2).

DES ID	W1 mag	W2 mag	W3 mag	W4 mag	$z_{\rm phot}$
209914488	16.85	16.06	11.69	8.50	0.321
209914542	...	...	...	...	0.998
209914588	...	...	...	...	0.480
209914804	16.68	15.98	12.20	8.49	1.391
209914529	...	...	...	...	0.963

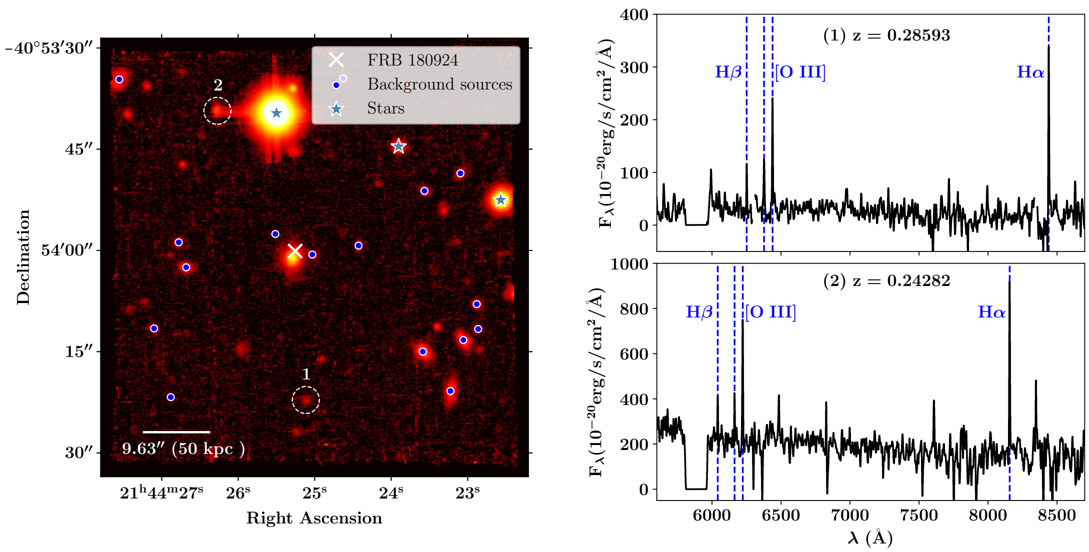

Figure 3.1: *Left:* MUSE white light image of the $1' \times 1'$ field around the host galaxy of FRB 180924. The circled objects are the two foreground galaxies and the blue dots are background sources identified using MARZ. The blue stars mark the stars in the field. The redshifts of the unmarked sources in the image could not be identified due to their spectra either being noisy or not having a clear correlation with any of the default MARZ template spectra. The white bar at the bottom represents 50 kpc at z_{host}. *Right:* The spectra of sources 1 and 2. Both galaxies show clear Hα, Hβ and [O III] doublet emission lines which help pinning their redshifts to the values noted above the spectra.

3.2.2 Spectroscopy

For the galaxies at $0.001 < z < 0.05$ along the sightline, we turned to the 2MASS survey database (Huchra et al., 2012) for spectroscopic data. This catalog contains galaxy spectra of 83% of the southern sky and is complete to $J < 13.75$ with median redshift $z = 0.053$. We determined that the galaxy in this catalog with the smallest perpendicular distance to the FRB sightline was 1.04 Mpc (15.2' angular distance) away, which is far beyond the typical virial radii of galaxy halos. We also found no galaxy within 500 kpc in NearGalCat, the updated nearby galaxy catalog of 869 galaxies within 11 Mpc of the Milky Way which is estimated to be $\sim 40\%$ complete (Karachentsev et al., 2013). Thus, we conclude the $z < 0.03$ intervening galaxy halo contribution to $\mathrm{DM}_{\mathrm{FRB}}$ is negligible if not null.

To survey galaxies close to the FRB sightline we used the MUSE integral field unit (Bacon et al., 2010a) on the Very Large Telescope (VLT). A set of 4×628 s exposures were obtained on UT 2018 November 5 from program 2102.A-5005 (PI Macquart); another set of 4×600 s exposures were obtained on UT 2019 December 6 from program 0104.A-0411 (PI Tejos). These observations were carried out in the Wide-Field Adaptive Optics (WFM-AO) mode, corresponding to a effective FoV of $1 \times 1'$ with a pixelscale of $0.2''$, and covering a wavelength range of $R \approx 4800 - 9300\,\mathrm{\AA}$ at a resolving power of $\sim 2000 - 4000$, respectively. After preliminary reduction using the EsoReflex pipeline (Freudling et al., 2013), the frames were flat-field corrected, sky-subtracted and co-added using the CubExtractor package (see Cantalupo et al., 2019, for a description). Sources in the datacube were identified from the white light image, i.e., the cube collapsed along the spectral dimension (see Figure 3.1), using the Source Extractor of Python (SEP) package (Bertin & Arnouts, 1996; Barbary, 2016). We set minimum threshold of 3 standard deviations above the sky background level and with a minimum area of 10 pixels. Their spectra were extracted from the spaxels within the elliptical apertures whose linear dimensions were twice as large as those returned by SEP. The extraction weighted the flux from the spaxels encircled by the aperture equally. Where the aperture intersected a spatial pixel, the flux from that pixel was scaled down by the fraction of the pixel area within the aperture. Redshifts were identified for each spectrum from the emission features using the Manual and Automatic Redshifting software (MARZ; Hinton et al., 2016). Out of the 72 non-stellar sources identified from the white light image, 19 had their redshifts confidently assigned. These objects are listed in Table 3.3. The remaining spectra did not have identifiable spectral features (e.g. emission lines). Further relaxing the source detection criteria for SEP increased the number of "sources" but did not increase the number of identified redshifts. From the secure redshifts, we identify two foreground sources from the datacube ($z = 0.24282$ and 0.28593; see Figure 3.1). Only the closer galaxy is detected in the DES $grizY$ imaging catalog.

We also obtained spectra of 5 galaxies using the Low Resolution Imaging Spectrograph (LRIS) installed on the Keck telescope on November 8 2020 in the longslit spectroscopy mode. These galaxies were targeted as our analysis indicated they could contribute to $\mathrm{DM_{FRB}}$(see Section 3.3.2). We used the "d560" dichroic, 600/4000 grism on the blue side and 600/7500 grating for the red side with 2×2 binning on both detectors. Three of these spectra were exposed for $\sim$ 700 s while the other two were exposed for $\sim 300\,\mathrm{s}$. We could not expose longer on account of bad weather. Of the

Table 3.3: MUSE and LRIS sources with unambiguous redshifts.

RA deg	Dec deg	Redshift	DES ID	r mag	Separation arcmin	⊥ dist. kpc
326.10947	-40.89425	0.24282	209914195	22.71	0.40	94
326.10465	-40.90616	0.28593	...	...	0.37	98
326.10538	-40.90030	0.32157	209914488	20.54	0.01	3
326.10430	-40.90017	0.38406	...	...	0.04	13
326.11117	-40.90069	0.38407	209914588	22.63	0.26	85
326.09677	-40.90579	0.46956	209914896	22.09	0.52	189
326.10631	-40.89932	0.50086	...	...	0.06	24
326.09828	-40.90417	0.53556	209914807	21.87	0.40	158
326.09607	-40.90369	0.54431	209914777	22.41	0.47	186
326.09527	-40.90323	0.54464	...	...	0.49	193
326.11480	-40.89296	0.61709	209914131	22.10	0.60	252
326.10178	-40.89980	0.75084	209914542	24.54	0.16	74
326.09534	-40.90221	0.75097	209914676	23.54	0.47	213
326.10262	-40.89292	0.86432	...	...	0.44	210
326.09819	-40.89755	0.87372	209914406	23.86	0.36	171
326.11157	-40.89967	1.03010	209914529	24.29	0.28	138
326.09623	-40.89683	1.03477	209914359	24.06	0.46	228
326.11291	-40.90321	1.43899	...	...	0.40	206
326.11201	-40.90604	2.95747	...	...	0.47	225
326.09791	-40.93261	0.07221	1.98	209916475	18.69	169

5 galaxies, one was confidently assigned a redshift using MARZ and it was determined to be a foreground source ($z = 0.07221$; 169 kpc away). We did not detect identifiable emission lines in the remaining 4 low S/N spectra.

3.3 Methods

3.3.1 Photometric analysis

We aim at estimating the DM contribution of galaxies that only have photometric redshifts, for which we require several intermediate derived quantities to then compute $\mathrm{DM}_{\mathrm{phot,halos}}$, the DM contribution of galaxies without spectroscopic redshifts in our sample. Namely, we require photometric redshifts, z_{phot}, and halo mass estimates, M_{halo}, for every galaxy.

We first estimated the posterior distribution of z_{phot} for each DES galaxy using the EAZY software package (Brammer et al., 2008). Redshifts were only computed for those galaxies which were detected in at least four of the nine filters considered (five from DES and four from WISE) and were estimated in a Bayesian framework using template spectral energy distribution (SED) fitting. We used linear combinations of the templates available in the `eazy_v1.3` set and applied magnitude priors on the r-band photometry when available (see details in Brammer et al., 2008). When fitting, the redshift was allowed to freely vary between 0.01 and 7 but the priors heavily penalized redshifts higher than 2.

The estimation of halo masses is less direct. Briefly, starting with an estimate for the galaxy's redshift based on the photometry, we fitted the available fluxes with an SED using the CIGALE software package (Noll et al., 2009; Boquien et al., 2018). We assumed, for simplicity, a delayed-exponential star-formation history with no burst population, a synthetic stellar population prescribed by Bruzual & Charlot (2003), the Chabrier (2003) initial mass function (IMF), dust attenuation models from Calzetti (2001), and dust emission templates from Dale et al. (2014), where the AGN fraction was capped at 20%. This provided an estimate of the stellar mass, M_*, of the galaxy at a given z. We then translate M_* to galactic halo mass, $M_{\rm halo}$, using the mean Stellar to Halo Mass Ratio (SHMR) described by Moster et al. (2013) at that z. For sources with spectroscopic redshifts, the galaxy redshift is fixed in the CIGALE input. We elaborate on the use of $z_{\rm phot}$ posteriors for the remaining sources in the next subsection.

The uncertainties in the M_* estimation and the SHMR relation propagate into the $\mathrm{DM}_{\rm halos}$ estimate. For each galaxy, we assumed that the $\log M_\star$ distribution at a given redshift was Gaussian with the mean and standard deviations obtained from CIGALE. Accounting for the error in the SHMR is more involved as it depended on both M_* and galaxy redshift. The SHMR is described in Equation 2 of Moster et al. (2013) with 8 parameters. We took the best fit parameters and uncertainties from their Table 1 as the mean and standard deviations of the independent normal distributions that these parameters were sampled from. For simplicity, we ignored any co-variance in these fit parameters (future work will account for this). We then produced a uniform 2D grid of redshift (between 0.03 and 0.35 spaced by 0.01) and $\log M_\star/\mathrm{M}_\odot$ (between 6 and 11 spaced by 0.005). At each grid point, we sampled the parameter distributions and produced a lookup table of the mean and standard deviations of halo masses that can be realized. Then, to quicken computation, we constructed interpolation functions that mapped the 2D grid to the mean and standard deviation of $\log M_{\rm halo}/{\rm M}_\odot$. Figure 3.2 shows the mean and standard deviations for some representative redshift and stellar mass values. The halo mass distributions were assumed to be Gaussian with the moments given by these interpolation functions.

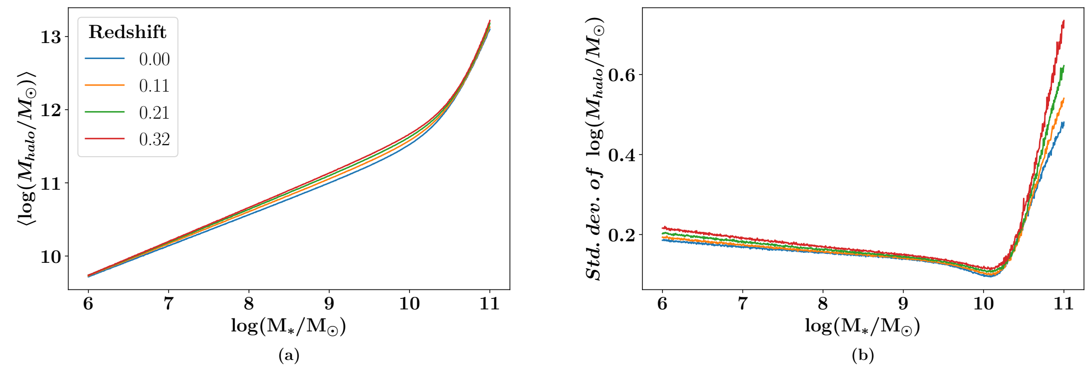

Figure 3.2: $M_{\rm halo}$ stellar to halo mass ratio (SHMR) mean and standard deviation obtained from sampling the fit parameter space from Moster et al. (2013). The SHMR relation (their eq. 2) contains 8 fit parameters and in this work, we have assumed they are independent and normally distributed. The mean and standard error of these fit parameters were obtained from their Table 1. Using these curves, interpolation functions are constructed to translate (M_*,z) pairs to $M_{\rm halo}$ distributions.

3.3.2 Halo contribution to DM

To estimate $\mathrm{DM_{halos}}$, we performed an analysis similar to the one outlined by Simha et al. (2020) for the FRB 190608 sightline. Briefly, they identified foreground galaxies based on spectroscopic redshifts and estimated halo masses from the available photometry. Then they estimated the line of sight electron number density integral for each intevening halo assuming a model for the baryonic distribution and summed the contributions to yield $\mathrm{DM_{halos}}$. We emphasize that the redshift serves as a key input to each step of the analysis. In the case of FRB 180924, we modified the procedure to leverage galaxies with $z_{\rm phot}$ as follows (see Figure 3.3 for a visual flowchart):

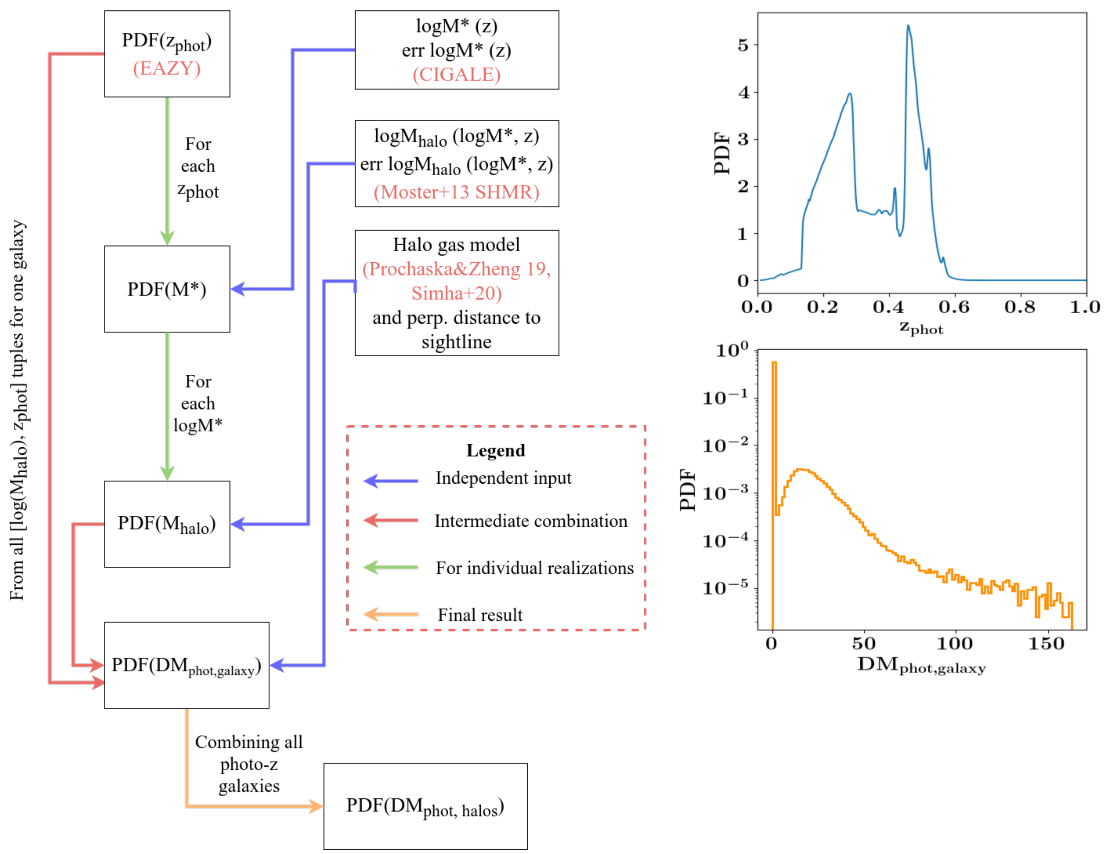

Figure 3.3: A schematic flowchart of our procedure to estimate $\mathrm{DM}_{\rm phot,halos}$. The boxes in the centre with blue arrows emanating from them represent independent inputs into the calculation. These include the stellar mass estimates, the SHMR and the halo gas model. The $z_{\rm phot}$ PDF is also an independent input and an example for one galaxy is shown on the plot on the top right. The sources of these estimates are mentioned in red lettering. The PDF of $\mathrm{DM}_{\rm phot,halos}$ is obtained in stages. First, the PDF of stellar masses at each redshift (sampled from the EAZY $z_{\rm phot}$ posterior) is obtained. Then each stellar mass and redshift tuple is translated to halo mass distributions using the Moster et al. (2013) SHMR relation. Compiling all the halo mass and redshift tuples and calculating their DM contribution (using the method outlined in Prochaska & Zheng, 2019; Simha et al., 2020), yields a PDF of DM values for each individual galaxy in our sample. An example of this is shown in the bottom right plot for the same galaxy as the $z_{\rm phot}$ PDF plot. The final PDF of $\mathrm{DM}_{\rm phot,halos}$ is estimated by sampling the galaxy DM PDFs and obtaining the distribution of the sum of these samples.

For a given galaxy:

1. We estimated the posterior distributions for $z_{\rm phot}$ and sampled them to produce 1000 realizations.

2. Separately, we allowed the galaxy redshift to vary from 0.03 to 0.35 in a linear grid (spacing 0.01) and estimated the mean and standard deviation of the stellar mass at each grid point using CIGALE.

3. Then, at each redshift realization from step 1, we sampled the $\log M_\star$ distribution (100 times) obtained using the CIGALE outputs as described in the previous sections.

4. For each stellar mass estimate, we used the 2D interpolation functions to obtain the mean and standard deviation of halo mass. Using these parameters, we produced 10 samples of halo mass values.

5. Combining all the halo mass realizations for all redshift and stellar mass pairs (i.e. $1000 \times 100 \times 10 = 10^6$ total realizations), we finally produced estimates of DM for each galaxy halo intersecting the sightline (henceforth, $\mathrm{DM}_{\rm phot,galaxy}$). $\mathrm{DM}_{\rm phot,galaxy}$ values are calculated for each tuple of $M_{\rm halo}$ and $z_{\rm phot}$ realizations as follows:

   (a) First the perpendicular distance from the FRB sightline is computed.

   (b) Then, assuming the model for electron distribution as described in Simha et al. (2020), $\mathrm{DM}_{\rm phot,galaxy}$ is estimated. We assumed that each halo extends to 1 virial radius and the fraction of halo baryons present as hot ($> 10^6$ K) gas is 0.75. This assumes that 25% of the baryons in the galaxy is in condensed forms (e.g. stars and neutral gas; see Fukugita et al., 1998). While this fraction may vary with halo properties (e.g. Behroozi et al., 2010), we emphasize that this is a relatively conservative maximal model for the CGM of galaxies, i.e. one may consider the estimates as upper limits.

Finally, using the $\mathrm{DM}_{\mathrm{phot,galaxy}}$ distributions for all galaxies in the sightline, we produced the distribution of their sum, i.e. $\mathrm{DM}_{\mathrm{phot,halos}}$.

In the fifth step we imposed some bounds on M_{halo} estimates to ensure reasonable values. Namely, the M_{halo} estimated at a particular redshift grid point may not exceed $10^{12.8}$ $\mathrm{M}_\odot$, which is nearing a typical galaxy group halo mass. Exceeding this value is allowed by the uncertainty limits from the SHMR. Therefore, we artificially capped the halo mass estimates to $10^{12.8}$ $\mathrm{M}_\odot$, i.e. any halo mass realization above this limit was set by hand to $10^{12.8}$ $\mathrm{M}_\odot$. Our $\mathrm{DM}_{\mathrm{phot,halos}}$ distribution was largely unaffected by this choice of the upper limit as an overwhelming majority of galaxies (including the ones within $2''$ to the sightline) have halo mass estimates much less than this limit. Additionally, it is often the case that the posterior distribution of z_{phot} peaks beyond the FRB host redshift, $z_{\mathrm{host}}= z_{\mathrm{FRB}}$. Even in this case there is a non-zero probability of the galactic redshift being below z_{host}. For all z_{phot} realizations beyond z_{host}, we set $\mathrm{DM}_{\mathrm{phot,galaxy}}=0\ \mathrm{pc\,cm^{-3}}$.

3.4 Results

Figure 3.4a shows the average $\mathrm{DM}_{\mathrm{phot,galaxy}}$ contributed by each of the foreground sources estimated using this method. We excluded all sources for which we

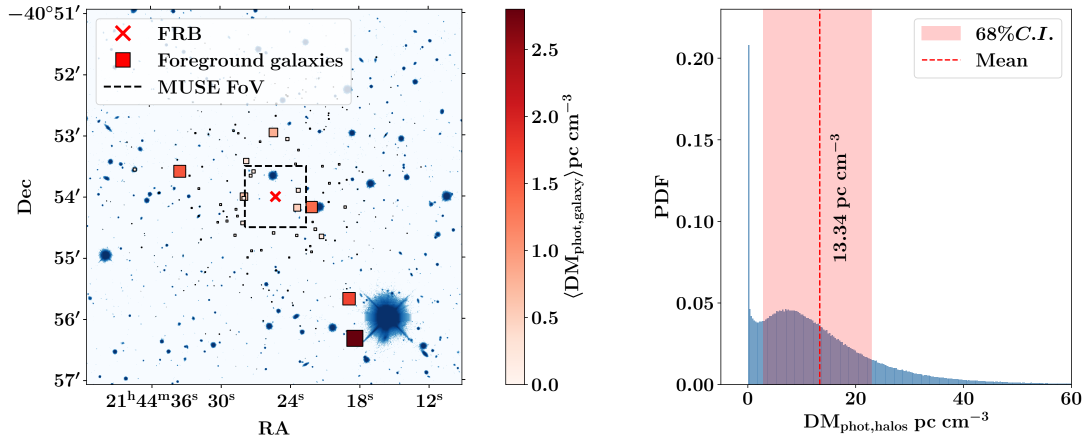

(a) (b)

Figure 3.4: (a) Locations of DES galaxies (excluding those with MUSE and LRIS redshifts) coloured by their average estimates of $\mathrm{DM_{phot,galaxy}}$. Both the colors and the sizes of the points are proportional to the mean $\mathrm{DM_{phot,galaxy}}$. The background image in blue is the DES r-band image of the field. The objects that fall within the MUSE field of view (black, dashed rectangle) do not have spectroscopic redshifts as their spectra did not have identifiable spectral features. (b) A realization of the PDF of $\mathrm{DM_{phot,halos}}$ estimated by producing 10^6 realizations of the sum of $\mathrm{DM_{phot,galaxy}}$ for all non-spectroscopic galaxies. The histogram counts are normalized to add up to unity. The large spike at 0 $\mathrm{pc\,cm^{-3}}$ is indicative of the possibility of most of these galaxies being in the background according to their z_{phot} posteriors.

have spectroscopic redshifts from MUSE or LRIS. There were $\sim$ 11000 DES galaxies in our catalog. We had expected correctly that a large fraction of these sources do not contribute to $\mathrm{DM_{halos}}$.

Based on these results, we targeted the 5 sources with highest mean $\mathrm{DM_{phot,galaxy}}$ using Keck/LRIS (§ 3.2.2 and we detected line emission from one ($z =$ 0.07221) of them, thus solidifying its redshift (listed in the last row of Table 3.3).

Figure 3.4b shows a realization of the final PDF of $\mathrm{DM_{phot,halos}}$ estimated from the 422 galaxies that have a non-zero probability of contributing to the FRB DM. Its mean value is 13 $\mathrm{pc\,cm^{-3}}$ and the 68% confidence bounds are 4 and 23 $\mathrm{pc\,cm^{-3}}$. The

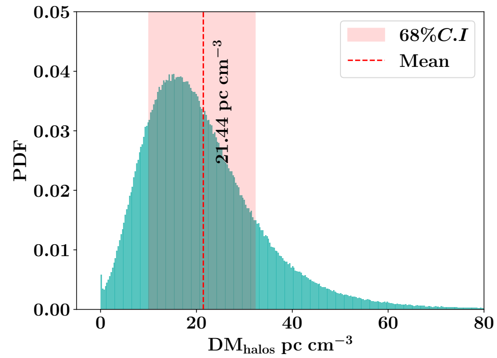

Figure 3.5: The distribution of $\mathrm{DM_{halos}}$ estimated using the full sample of foreground galaxies i.e. including galaxies with spectroscopic redshifts from MUSE and LRIS. The galaxies with spectra add 7.1 $\mathrm{pc\,cm^{-3}}$ to $\mathrm{DM_{halos}}$ on average, thus shifting the mean value from 13.34 $\mathrm{pc\,cm^{-3}}$ in Figure 3.4b to 21.44 $\mathrm{pc\,cm^{-3}}$.

spike at 0 $\mathrm{pc\,cm^{-3}}$ arises from the fact that most galaxies have their redshift posterior distributions peaking beyond the FRB redshift, i.e. the majority of these are likely to have zero contribution to $\mathrm{DM_{FRB}}$.

Our sample of foreground galaxies with spectroscopic redshifts consists of three galaxies: two from our MUSE datacube and one from our LRIS pointings. One of the MUSE galaxies (z=0.2859) does not have DES/WISE photometry. Therefore, we derived the stellar mass estimate from a pPXF (Cappellari, 2017) fit to its MUSE spectrum and assumed an error of 0.3 dex for $\log M_\star/\mathrm{M_\odot}$. From these galaxies, we estimated the mean net DM contribution of 7 $\mathrm{pc\,cm^{-3}}$with 68% confidence bounds being 3 $\mathrm{pc\,cm^{-3}}$ and 12 $\mathrm{pc\,cm^{-3}}$. The bounds were estimated by propagating the uncertainties in the stellar mass and SHMR as described previously but the redshift is fixed.

Thus, the mean $\mathrm{DM_{halos}}$ estimate, which is the sum of the estimates from the two disjoint samples is 21 $\mathrm{pc\,cm^{-3}}$ and the 68% confidence limits are 9 $\mathrm{pc\,cm^{-3}}$ and 32 $\mathrm{pc\,cm^{-3}}$. The full distribution is shown in Figure 3.5.

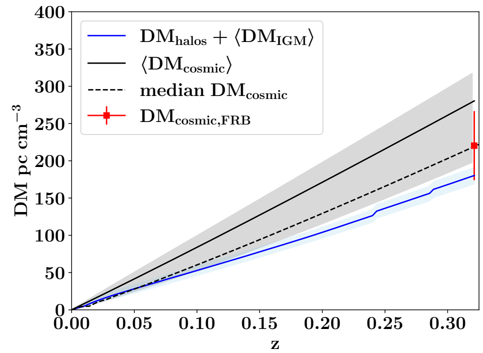

Figure 3.6: An estimate of DM_{cosmic} for the FRB 180924 sightline (blue, solid line) which is a sum of DM_{halos} from this analysis and the average diffuse IGM contribution, $\langle DM_{IGM} \rangle$. Starting from z = 0, DM_{halos} increases as one encounters halos along the sightline and the value at z_{host} is the one estimated in Figure 3.5. $\langle DM_{IGM} \rangle$ increases similarly as more matter is met on average going out towards the FRB. The blue, shaded region corresponds to the 68% confidence interval obtained from the uncertainty in DM_{halos}. The red point at 220 pc cm^{-3} is an estimate of $DM_{cosmic,FRB}$ obtained by subtracting the Milky Way and host galaxy contributions from the net DM. The error bar is the net uncertainty in this estimate and corresponds to 50 % uncertainty in each of the subtracted quantities, added in quadrature. The black, solid line is $\langle DM_{cosmic} \rangle$ described by the Macquart relation and the gray shaded region represent its scatter (1σ limits) due to the filamentary nature of the cosmic web. The black dotted line is the locus of all the median values of DM_{cosmic} obtained from the same distribution (Macquart et al., 2020).

3.5 Discussion and concluding remarks

For FRB 190608, Simha et al. (2020) estimated DM_{halos} to be between 7 pc cm^{-3} and 28 pc cm^{-3}. This corresponded to between 2% and 8% of the net DM and between 5% and 20% of DM_{cosmic}. In the case of FRB 190608, the theoretical average value, $\langle DM_{halos} \rangle$ at z_{host} is 44 pc cm^{-3}, a few times larger than the estimated DM_{halos}in that sightline. This expectation value is computed assuming ΛCDM cosmological parameters from Planck Collaboration et al. (2016a), a model for the gas density in halos (the same as we have used previously), and the Aemulus halo mass function (HMF; McClintock et al., 2019). The HMF is integrated between $10^{10.3}$ $M_\odot$

and 10^{16} $M_\odot$.

In the case of FRB 180924, the expected $\langle \mathrm{DM_{halos}} \rangle$ is 121 $\mathrm{pc\,cm^{-3}}$ because it is more distant than than FRB 190608. Compared to this, the mean value of $\mathrm{DM_{halos}}$ estimated in the previous section is just 21 $\mathrm{pc\,cm^{-3}}$ assuming the same CGM model. Thus, $\mathrm{DM_{halos}}$ is conclusively lower than average for this sightline, much like FRB 190608.

Figure 3.6 shows, with a solid blue line, the sum of our $\mathrm{DM_{halos}}$ estimate and $\langle \mathrm{DM_{IGM}} \rangle$,the average DM contribution of the diffuse IGM. We define $\langle \mathrm{DM_{IGM}} \rangle$ as $\langle \mathrm{DM_{halos}} \rangle$, as computed above, subtracted from $\langle \mathrm{DM_{cosmic}} \rangle$, i.e. the mean Macquart relation ($\langle \mathrm{DM_{IGM}} \rangle \equiv \langle \mathrm{DM_{cosmic}} \rangle - \langle \mathrm{DM_{halos}} \rangle$). Comparing it to the $\mathrm{DM_{cosmic,FRB}}$ estimate (shown as a red point with errors) we see that the two independently computed estimates are indeed consistent. Favored models of the cosmic web indicate that most FRB sightlines in the universe will have few if not zero dark matter halos intersecting them proximally (e.g. Macquart et al., 2020).i.e. if one were to connect the median values of the $\mathrm{DM_{cosmic}}$ distributions at each redshift, the resulting curve, which can be called the median Macquart relation, lies below the mean curve and is shown as the dotted, black line. Indeed, $\mathrm{DM_{cosmic,FRB}}$ is coincident with this median curve. We therefore conclude that FRB 180924 is one such sightline.

We note here that there are indeed other models of gas distribution in the CGM, some of which predict larger dispersion measures, by a factor of a few, from individual halos, (e.g. see Figure 1 of Prochaska & Zheng, 2019). If we were to use any of these models which predict systematically higher DM contributions, both $\mathrm{DM_{halos}}$ and $\langle \mathrm{DM_{halos}} \rangle$ would increase by the same factor, and therefore $\mathrm{DM_{halos}}$ for this sightline would still be lower than average. Simultaneously, our estimate for $\mathrm{DM_{cosmic}}$ in Figure 6 (the blue line) would decrease when using these models. This is because $\langle \mathrm{DM_{IGM}} \rangle$ constitutes the majority of the $\mathrm{DM_{cosmic}}$ estimate and by definition, it decreases with increasing $\langle \mathrm{DM_{halos}} \rangle$. One must be cautious when performing this exercise however. For instance, with our chosen model of halo gas distribution, we estimate $\langle \mathrm{DM_{halos}} \rangle = 121\ \mathrm{pc\,cm^{-3}}$. Since $\langle \mathrm{DM_{cosmic}} \rangle = 280\ \mathrm{pc\,cm^{-3}}$ is independent of this model, doubling $\langle \mathrm{DM_{halos}} \rangle$ would only leave $\sim 40\ \mathrm{pc\,cm^{-3}}$ for $\langle \mathrm{DM_{IGM}} \rangle$. This is low and likely unrealistic at the host redshift, especially compared to the $\mathrm{DM_{IGM}}$ estimate using the MCPM method for the FRB 190608 sightline by Simha et al. (2020). Thus, to truly estimate $\mathrm{DM_{cosmic}}$ one cannot simply use $\langle \mathrm{DM_{IGM}} \rangle$, and a detailed, semi-empirical model of the cosmic web density is required.

In summary, we have shown that photometric data can be used effectively to constrain $\mathrm{DM_{halos}}$. While the uncertainty in this endeavor is significant, one can use this as a first step in identifying targets for efficient spectroscopic follow up observations. Having full spectroscopic coverage of the field is undeniably better as the photo-z analysis can misidentify background sources as being in the foreground and vice-versa. In the near future, we intend to obtain spectra of field galaxies within a few degrees of FRB 180924 and perform a full cosmic web analysis, including a direct accounting of the diffuse IGM DM contribution. With upcoming large-scale spectroscopic surveys such as DESI, more FRB fields will have galaxies with precise redshifts and a statistical analysis of multiple FRB fields to constrain cosmic web properties such as the fraction of cosmic baryons will be enabled.

Acknowledgments:

Authors S.S., N.T., J.X.P., and K.G.L. as members of the Fast and Fortunate for FRB Follow-up team, acknowledge support from NSF grants AST-1911140 and AST-1910471. K.G.L. acknowledges support from JSPS KAKENHI Grants JP18H05868 and JP19K14755. K.W.B. acknowledges Australian Research Council (ARC) grant DP180100857. N.T. acknowledges support by FONDECYT grant 11191217. S.C. gratefully acknowledges support from Swiss National Science Foundation grant PP00P2_190092 and from the European Research Council (ERC) under the European Union's Horizon 2020 research and innovation programme grant agreement No 864361. R.M.S. acknowledges support through Australian Research Council Future Fellowship FT190100155 and Discovery Project DP180100857. The Australian Square Kilometre Array Pathfinder is part of the Australia Telescope National Facility which is managed by CSIRO. Operation of ASKAP is funded by the Australian Government with support from the National Collaborative Research Infrastructure Strategy. ASKAP uses the resources of the Pawsey Supercomputing Centre. Establishment of ASKAP, the Murchison Radio-astronomy Observatory and the Pawsey Supercomputing Centre are initiatives of the Australian Government, with support from the Government of Western Australia and the Science and Industry Endowment Fund. We acknowledge the Wajarri Yamatji as the traditional owners of the Murchison Radio-astronomy Observatory site.

Based on observations collected at the European Southern Observatory under ESO programmes 2102.A-5005 and 0104.A-0411. Spectra were also obtained at the W. M. Keck Observatory, which is operated as a scientific partnership among Caltech, the University of California, and the National Aeronautics and Space Administration (NASA). The Keck Observatory was made possible by the generous financial support of the W. M. Keck Foundation. The authors recognize and acknowledge the very significant

cultural role and reverence that the summit of Mauna Kea has always had within the indigenous Hawaiian community. We are most fortunate to have the opportunity to conduct observations from this mountain.

Chapter 4

The LRIS Red-side detector upgrade

4.1 Introduction

The Low-Resolution Imaging Spectrograph (LRIS) is a dual-beam optical spectrograph that has been in operation at the Keck I telescope since 1993. The instrument consists of two separate detector systems that receive light split by a dichroic into bluer and redder wavelengths (e.g., the D560 dichroic splits the light around 5600 Å). This allows the spectrograph to cover a wide range of visible and near-infrared wavelengths (4000Å − 11000Å) while enabling a user to separately configure the optical elements that feed into the two detector systems (i.e., gratings and prisms). LRIS is a workhorse instrument at the W. M. Keck Observatory.

In 2010, the LRIS red-side detector subsystem was upgraded to an array of two $300\mu m$-thick 2048×4096, i.e., $2k \times 4k$, Lawrence Berkeley National Laboratory (LBNL) charge-coupled device (CCD) detectors (Rockosi et al., 2010). The detectors were placed side-by-side to effectively create a $4k \times 4k$ CCD array, which covered a $6' \times 8'$ area in the sky. The configuration had a 26.4 arcsecond gap between the two detectors. The 300 μm high-resistivity silicon layer of the LBNL CCDs vastly improved the quantum efficiency, i.e. the fraction of incident photons converted to electrical charge and hence signal, ($\sim$ 1.4 times) above 7000Å compared to its much thinner ($\sim 15\mu m$) predecessor. Thus, not only was near-infrared sensitivity improved, but it also solved a different problem: fringing. Previously, as red photons were subject to multiple reflections within the thin CCD layer, it produced fringes on the image due to interference. With the thicker CCD, multiple reflections were greatly reduced due to the detector absorbing the majority of the incident photons and thus eliminating fringing.

In 2020, one of the two CCDs on the red-side detector array began facing serious charge transfer issues during readout, resulting in the complete loss of signal from half of the field-of-view. While the blue side detector was still functioning normally, multi-object spectroscopy using slitmasks was severely hampered. Thus, it was deemed necessary to replace the malfunctioning CCD array. This chapter pertains to the most recent red-side detector upgrade in 2021. As part of the team led by Prof. Constance Rockosi, I shall describe the detector characterization and software testing I performed. The upgraded LRIS red-side (Mark IV) was installed by the team of engineers and scientists at the Keck Observatory in May 2021 (Kassis et al., 2022) and has since delivered excellent observations, including for my own science goals (see Chapter 5 and 6).

4.2 Detector Characterization

4.2.1 A brief overview of the test setup

Before installing the new $500\mu m$ $4k \times 4k$ LBNL CCD into LRIS, it was necessary to characterize the detector response and test the readout electronics and control software that interacted with the CCD. To this end, Dale Sandford connected the CCD to a pre-amplifier board that connected to the Archon CCD controller, developed by the Semiconductor Technology Associates (STA). The CCD was placed inside a test dewar, i.e., a vacuum chamber, with a liquid nitrogen cooling system. The temperature was controlled using a heater inside the dewar and monitored using the temperature sensor. The Archon also controlled the shutter on the test dewar. The Archon was further connected via ethernet to a host computer, which ran the LRIS dispatcher software. The dispatcher enabled continuous monitoring of the various sensors connected to the dewar and the CCD, as well as the ability to control the CCD, shutter, and dewar heater via the Archon. I interacted exclusively with the CCD at the dispatcher software level, which was developed by Steve Allen and Dale Sandforcorrespondinger and provides control via keywords corresponding to various boolean switches and sensor readings. The electronics within the dewar could be controlled by setting the keywords to desired values. For instance, to perform a readout, a sequence of keywords was set to

1. Turn on the CCD power.
2. Configure the readout mode of the CCD (i.e. bias voltage, binning, and amplifiers used).
3. Set the exposure time and open the shutter.
4. Readout after the exposure.

Sequences of readouts were automated using bash scripts installed on the host computer, and after readout, the raw data was stored as FITS files. I tested the read noise, dark current, gain, charge transfer efficiency (CTE), and linearity of the CCD using the test setup described above. The following subsections describe the tests performed and the results obtained.

Quadrant	RN (e^-)	Std. dev in RN (e^-)
Upper Left	3.566	0.007
Upper Right	3.707	0.009
Lower Left	3.690	0.008
Lower Right	3.791	0.009

Table 4.1: Read noise measurements for the four quadrants of the LBNL 4k×4k CCD.

4.2.2 Read Noise and bias structure

A detector's Read Noise (RN) is characterized by the variance in the signal across individual pixels resulting from the signal processing circuitry on the chip. Thus, even without an illumination source, the CCD will display a non-zero variance from the electronics alone. To measure the RN, one takes a series of bias frames: zero-second exposures with the shutter closed to eliminate any charge accumulation from illumination or thermally generated electrons. Fig 4.1 shows one such bias frame read out with four amplifiers and four distinct quadrants. The read noise was estimated as the standard deviation in the pixel levels for each quadrant in each bias frame obtained. To mitigate the presence of cosmic rays in the bias, a sigma-clipped standard deviation estimator was used with data points above 3σ clipped. Table 4.1 shows the measured read noise and its variation on April 12th, 2021, before the CCD was installed in LRIS. The measurements are made in analog-to-digital units (ADUs) but can be converted to electrons (e^-) using the gain of the CCD (see next subsection).

In addition to the read noise measurement, a master bias frame was constructed by median-combining all the bias frames taken. The master frame is clear of cosmic rays and other transient features. I noted several columns with excess charge across each quadrant, the brightest of which is clearly visible in Fig. 4.1 in the lower right quadrant. I determined that the "hot" columns are not brighter than 1.2 e^- above the mean bias levels and thus can be safely subtracted without affecting any scientific data.

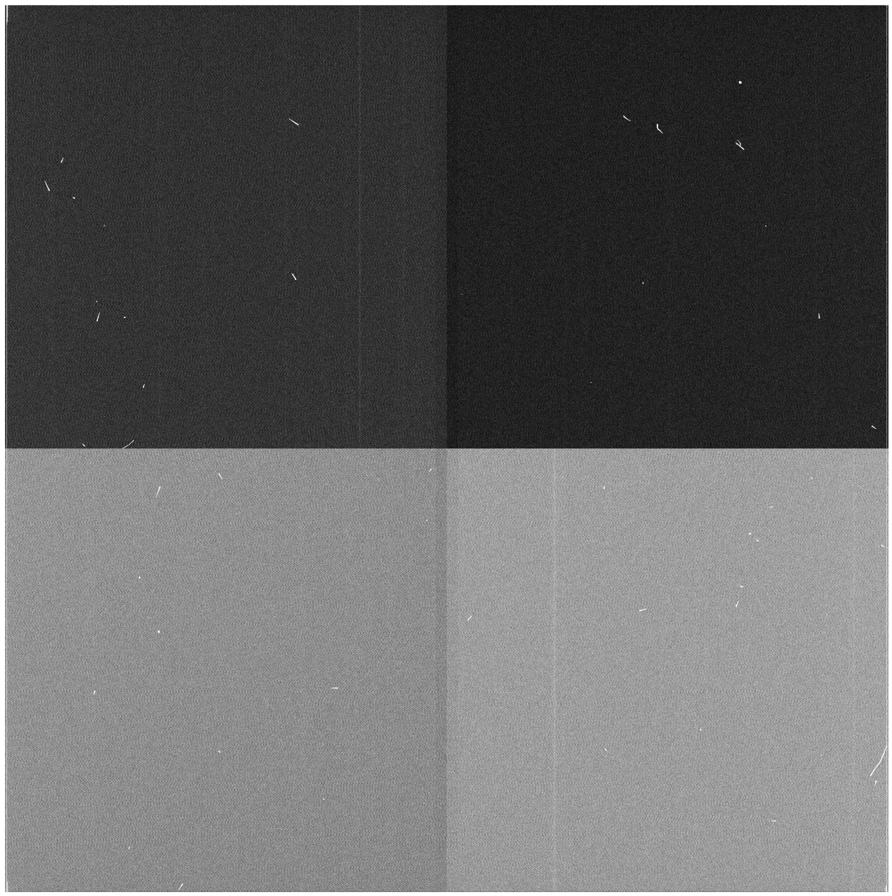

Figure 4.1: A bias frame taken with the LBNL 4x×4k CCD. The image was read out using four amplifiers and hence, the four quadrants display different bias levels. Note the bright streaks in the image due to cosmic rays incident upon the CCD during the exposure.

4.2.3 Gain and full well capacity

The camera gain, also known as the conversion factor, is the number of electrons generated per analog-to-digital unit (DN) of the CCD. The gain is a measure of

Quadrant	K e^-/ADU	Full well depth ADU	Full well depth $\times$ gain $e-$
Upper Left	1.7105 ± 0.0003	62461	106787
Upper Right	1.605 ± 0.0007	62479	100241
Lower Left	1.6405 ± 0.0006	62613	102682
Lower Right	1.6732 ± 0.0006	62581	104670

Table 4.2: Gain and full-well depth measurements for the four quadrants of the LBNL 4k×4k CCD. Here

the sensitivity of the CCD to light. The gain K is defined by (Janesick, 2001) as:

$$K = \frac{S(DN)}{\sigma_S^2(DN) - \sigma_R^2(DN)} \quad e^-/DN \tag{4.1}$$

Thus to estimate the gain, one plots a "photon-transfer curve". A series of flat frame exposures are taken with uniform illumination on the CCD with varying signal levels (i.e., increasing exposure time or changing the brightness). A median-combined bias frame is subtracted from each frame to yield the signal alone. For each signal level, two exposures are taken. As they are at the same illumination level, the difference image yields the total variance, σ_S^2 (times a factor of 1/2). Then, the variance due to read noise σ_R^2, as computed in the previous section, is subtracted from the net variance. The signal S is estimated from the mean of the two images. According to the equation 4.1 then, the gain is the slope of the plot of the signal versus the variance or if plotted in log space, the gain is exponential of the horizontal intercept of $\log(S)$ vs $\log(\sqrt{\sigma_S^2 - \sigma_R^2})$. Fig. 4.2 shows the photon-transfer curve for the CCD data from April 12th, 2021. Table 4.2 lists the measured gain values and errors estimated from the curve-fitting procedure. The full-well depth, i.e., the signal level at which the CCD saturates, was estimated to be $\sim 103000 \pm 2000e^-$ for the four quadrants.

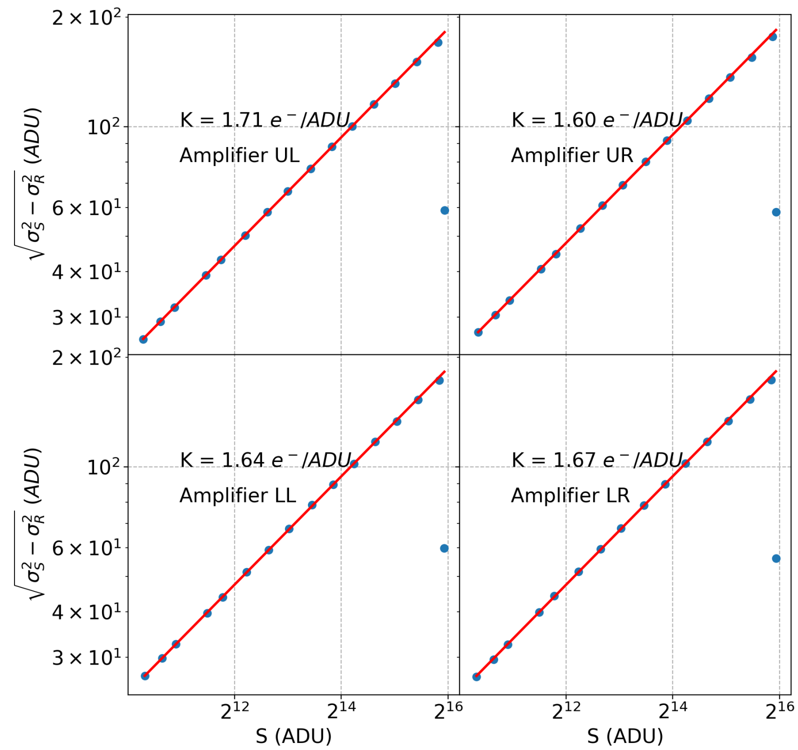

Figure 4.2: The photon-transfer curve for the LBNL 4k×4k CCD. The gain is estimated from the horizontal intercept of $\log S$ vs $\log(\sqrt{\sigma_S^2 - \sigma_R^2})$ line. The blue points represent the measurements, while the red curve is the line that best fits the data. The data point on the far right for every quadrant is at saturation and is not used in the fit.

4.2.4 Dark Current

The dark current is the charge generated by the thermal excitation throughout the CCD. We measure the current by taking a series of long exposures with the shutter closed. The dark current is then calculated by subtracting the bias level from the mean signal level in the dark frames. The dark current is a function of temperature and time and is typically expressed in electrons per pixel per second. At -105 ∘C, the dark current was measured to be $3.1 \pm 0.1e^{-}$/hour/pixel for the four quadrants. Thus, the dark current is negligible for the typical exposure times used in LRIS observations (~ 20 minutes). Higher exposure times are not recommended as a large number of pixels are affected by CRs, especially in the event of a cosmic-ray shower. Across 7 dark frames of 20 min exposure each, the fraction of pixels affected by CRs was estimated to be $\lesssim 3\%$.

4.2.5 Spectroscopic throughput

The LBNL 4k×4k CCD was successfully characterized for read noise, gain, full-well depth, and dark current. The measurements were repeated in the LRIS dewar after installation and the values obtained were consistent with those from pre-installation. The detector was successfully installed at Keck and achieved first light on April 27th, 2021 (see Fig. 4.3) and began science operations on May 7th, 2021 (see 4.4).

As the final detector characterization step, a spectroscopic standard star was observered to estimate the net spectroscopic throughput of the instrument. On May 25th, Feige 110 was observed with the 600/7500 grism, the 560D dichroic, and a 1.0 arcsecond slit. The data was reduced using the PypeIt reduction (Prochaska et al., 2020) package set to the default user parameters. To generate the throughput measurement, I

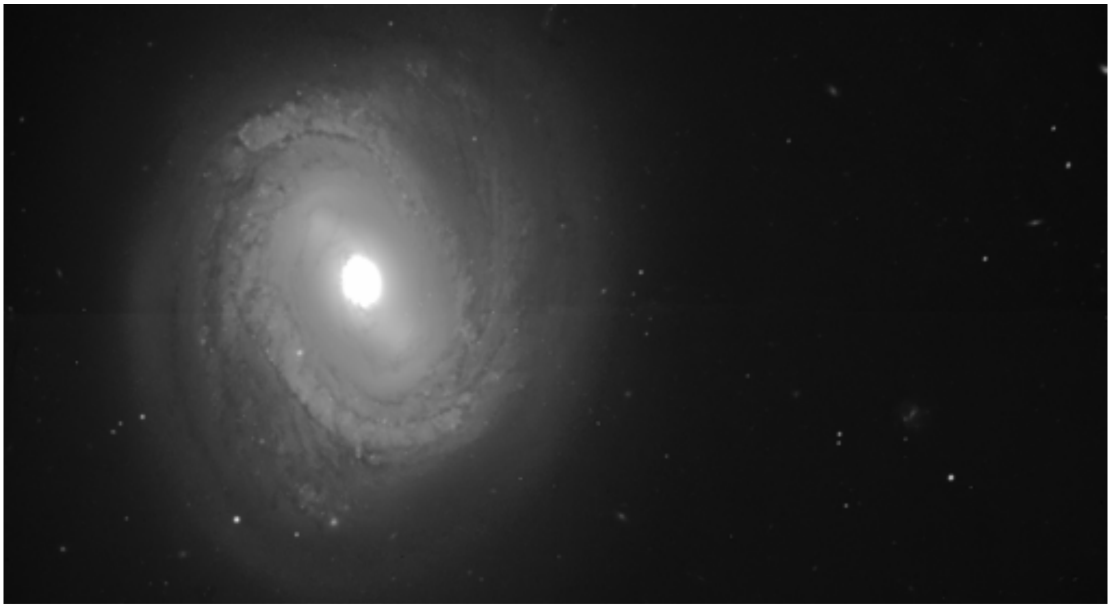

Figure 4.3: M58 as seen by LRIS-red Mark IV on April 27th, 2021. This is one of the first on-sky images obtained with the 4k×4k CCD installed in LRIS. *Image Credit: Kassis et al. (2022)*

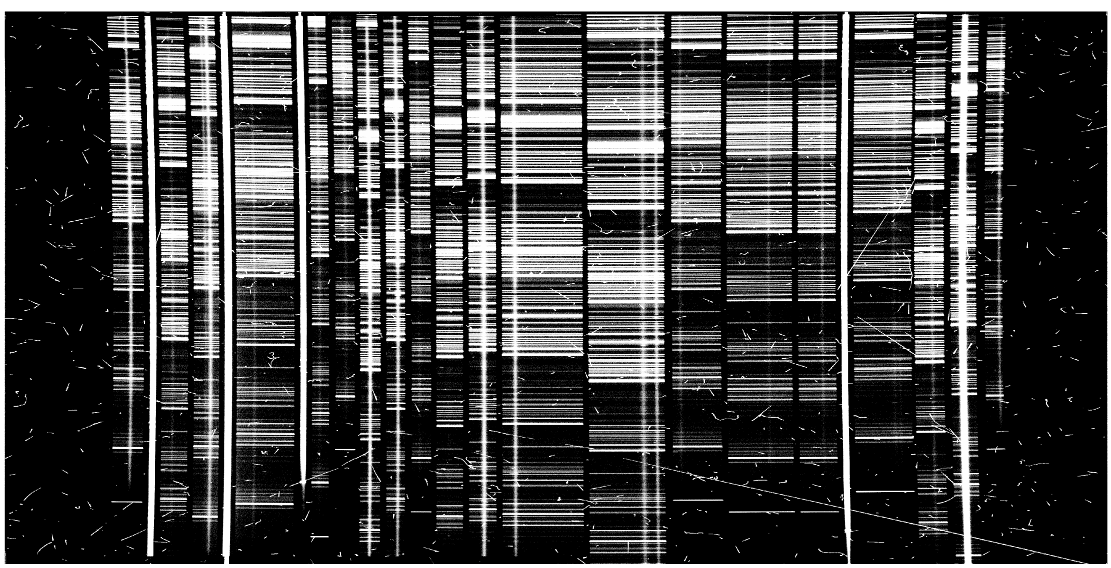

Figure 4.4: The first multi-slit spectroscopic observation obtained with the LRIS-red Mark IV. The raw file has been minimally processed: bias-subtraction, flat-fielding, and removal of the overscan regions. Note that the image contains no gap in the center as the single CCD eliminates the chip gap from LRIS red Mark III.

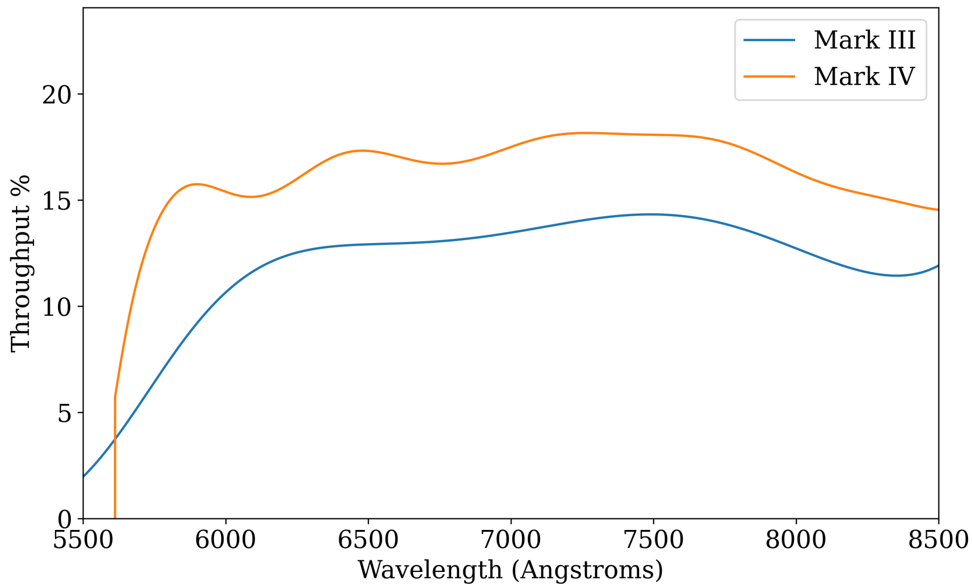

Figure 4.5: The net spectroscopic throughput of the LRIS-red spectrograph measured using PypeIt. The orange curve shows the throughput from the new Mark IV detector taken in May 2021 and the blue curve shows the throughput measure in January 2020 using the same grism (600/7500) and dichroic (560D) with the Mark III detector.

used the `pypeit_sensfunc` script with the `IR algorithm` on the 1-d spectrum produced from the reduction. Fig. 4.5 shows the net spectroscopic throughput of the LRIS-red Mark IV for Feige 110 in orange. As compared to the blue curve, which shows the throughput of the LRIS-red Mark III detector, the new detector has a higher throughput across the entire wavelength range.

Chapter 5

Searching for the sources of excess extragalactic dispersion of FRBs

Abstract

Probing the Cosmic Web with Fast Radio Bursts

by

H. S. Sunil Simha

The FLIMFLAM survey is collecting spectroscopic data of field galaxies near fast radio burst (FRB) sightlines to constrain key parameters describing the distribution of matter in the Universe. In this work, we leverage the survey data to determine the source of the excess extragalactic dispersion measure (DM), compared to the Macquart relation estimate of four FRBs: FRB20190714A, FRB20200906A, FRB20200430A, and FRB20210117A. By modeling the gas distribution around the foreground galaxy halos and galaxy groups of the sightlines, we estimate $\mathrm{DM_{halos}}$, their contribution to the FRB dispersion measures. The FRB20190714A sightline shows a clear excess of foreground halos which contribute roughly 2/3 of the observed excess DM, thus implying a sightline that is baryon-dense. FRB20200906A shows a smaller but non-negligible foreground halo contribution, and further analysis of the IGM is necessary to ascertain the true cosmic contribution to its DM. FRB20200430A and FRB20210117A show negligible foreground contributions, implying a large host galaxy excess and/or progenitor environment excess.

5.1 Introduction

With the advent of the concordance Lambda-Cold Dark Matter (Λ CDM) cosmological paradigm, there is now a comprehensive model for the large-scale structure of matter in the universe, and its formation under the influence of gravity is one of the key tests that is actively being researched. Cosmic microwave background (CMB) experiments (e.g. Bennett et al., 2013; Planck Collaboration et al., 2020) have precisely measured the contents of the universe and simulations have rendered clarity regarding the time-evolution of structure beginning from primordial fluctuations (e.g. Springel et al., 2005). In the current paradigm, dark matter forms the cosmic web, the large scale structure that includes voids, filaments, and dense halos and serves as scaffolding for the accretion of baryonic matter. Indeed, hydrodynamical simulations (e.g. Martizzi et al., 2019; Velliscig et al., 2015; Lee et al., 2021) have shown us that the ionized gas populates dark matter halos and also occupies the cosmic web filaments or the intergalactic medium (IGM), albeit in a much more diffuse state.

The low density of the IGM plasma has long challenged baryon census studies at $z \lesssim 0.5$. The Lyman alpha forest and UV absorption studies of metal ion tracers such as O VI and O VII are not sensitive to $\sim 40\%$ of the IGM baryons (i.e. the Missing-Baryon Problem; Fukugita et al., 1998; Shull et al., 2012) which reside in the hot ($\sim 10^6$ K), diffuse phase according to theory (e.g. Cen & Ostriker, 2006). With existing facilities, very long-exposure X-ray observations (multi-million seconds) are required to detect the weak absorption expected from O VII tracers of the hot phase (e.g. Nicastro et al., 2018). Alternatively, stacking the weak kinetic Sunyaev-Zeldovich signal between $\gtrsim 10^6$

galaxy pairs could reveal the gas in filaments (de Graaff et al., 2019).

In the meantime, the serendipitous discovery of the first Fast Radio Burst (FRB) in archival data (Lorimer et al., 2007) has set in motion a series of paradigm-changing discoveries. FRBs are millisecond-duration radio transients whose origins are still widely debated. With improved radio detection techniques, over the last five years multiple FRBs have been localized in the sky with sub-arcsecond accuracy (Tendulkar et al., 2017; Bannister et al., 2019; Law et al., 2020; Bhardwaj et al., 2021) and thus their distances could be confidently measured from their host galaxy redshifts ($z_{\rm FRB}$). FRBs pulses are dispersed by plasma during propagation and the extent of this effect is directly related to the integrated, line-of-sight free electron density (n_e). This effect is quantified by the FRB Dispersion Measure (DM$_{\rm FRB}$) which is defined as:

$$\mathrm{DM_{FRB}} = \int \frac{n_e}{1+z} dl \quad . \tag{5.1}$$

Here, z is the cosmological redshift and dl is the distance element along the line-of-sight. As DM$_{\rm FRB}$ is an integral quantity, it may be represented as the sum of the electron reservoirs encountered during propagation. i.e.

$$\mathrm{DM_{FRB}} = \mathrm{DM_{MW}} + \mathrm{DM_{cosmic}} + \mathrm{DM_{host}}. \tag{5.2}$$

Here, DM$_{\rm MW}$ is from the electrons within the Milky Way interstellar medium (ISM) and halo, DM$_{\rm host}$ is from the counterpart structures in the host galaxy, and DM$_{\rm cosmic}$ is from the plasma in intervening halos and the diffuse IGM in the foreground, i.e. $\mathrm{DM_{cosmic}} = \mathrm{DM_{halos}} + \mathrm{DM_{IGM}}$. Macquart et al. (2020) were the first to estimate DM$_{\rm cosmic}$ for a sample of localized FRBs and showed that it is correlated with $z_{\rm FRB}$. This was as expected of the current paradigm of cosmological expansion and the fraction of ionized baryons in the universe [1]. This proved directly that the “Missing” Baryons were not just found, but also that $\mathrm{DM_{FRB}}$ could viably probe the diffuse plasma in the Universe. The community has largely adopted the moniker of the “Macquart relation” to refer to the average $\mathrm{DM_{cosmic}}$, i.e. $\langle \mathrm{DM_{cosmic}} \rangle$versus z_{FRB}.

While the mean Macquart relation is well described by cosmology (e.g. Inoue, 2004), there is expected to be scatter about $\mathrm{DM_{cosmic}}$ at any given redshift due to the inhomogeneity of cosmic structure. For example, some FRB sightlines may intersect the gas-rich environments of intra-galaxy cluster media while others may primarily intersect cosmic voids. Furthermore, galaxy feedback can influence the variance in gas density by distributing gas further out of gravitational wells (e.g. Prochaska & Zheng, 2019). Indeed, as we shall show in the subsequent section, one identifies a number of FRBs where estimates for $\mathrm{DM_{cosmic}}$ from nominal assumptions on $\mathrm{DM_{host}}$ imply $\mathrm{DM_{cosmic}} > \langle \mathrm{DM_{cosmic}} \rangle$. However, it is not evident *a priori* if the excess arises from foreground structure (i.e. intervening halos and IGM overdensities) or from an atypical host and progenitor environment. Our previous work (Simha et al., 2020, 2021) has introduced a methdology to estimate the contribution from foreground halos. Here, we apply our analysis to four FRB sightlines with apparently high $\mathrm{DM_{cosmic}}$ values. Future application of such analyses on a statistical sample of FRBs can inform us on the distribution of ionized gas within dark matter halos (e.g. McQuinn, 2014b; Prochaska & Zheng, 2019; Lee et al., 2022; Connor & Ravi, 2022; Cook et al., 2023; Ravi et al., 2023; Wu & McQuinn, 2023).

To this end, we leverage the redshifts of galaxies collected as part of the

[1]Estimated by leveraging observational constraints on denser baryon reservoirs in the form of stars, remnants and neutral gas (e.g. Fukugita, 2004; Macquart et al., 2020).

FRB Line-of-Sight Ionization Measurement From Lightcone AAOmega Mapping (FLIMFLAM) survey (Lee et al., 2022). This redshift survey aims to study the foreground matter distribution along ~ 30 FRB sightlines. The key results expected from the survey include constraints accurate to $\sim 10\%$ on (1) the fraction of baryons in the universe in the diffuse IGM; and (2) the fraction of baryons residing in circum-galactic halos that are in the ionized phase. In this redshift survey, spectroscopic redshifts and photometry of foreground galaxies within ~ 1 degree of an FRB sightline are used to generate bespoke models of the line-of-sight ionized matter density tailored to individual lines-of-sight, which can then be compared with the DM from the FRB. Key reservoirs of said matter include intervening dark matter halos and the diffuse intergalactic medium (IGM). In this work, with a subset of the spectroscopic data collected, we investigate four excess $\mathrm{DM}_{\mathrm{cosmic}}$ sightlines: FRB20190714A, FRB20200430A, FRB20200906A and FRB20210117A. These fields were targeted with the wide-field Anglo-Australian Telescope (AAT)/AAOmega and the Keck/LRIS and DEIMOS spectrographs.

This manuscript is outlined as follows: Section 5.2 describes the data collection and reduction, while Section 5.3 describes our intervening-galaxy-halo DM estimation procedure. Section 5.4 describes the results and Section 5.5 discusses their implications. Throughout this work, unless otherwise specified, we assume a ΛCDM cosmology with Planck 2018 cosmological parameters (Planck Collaboration et al., 2020).

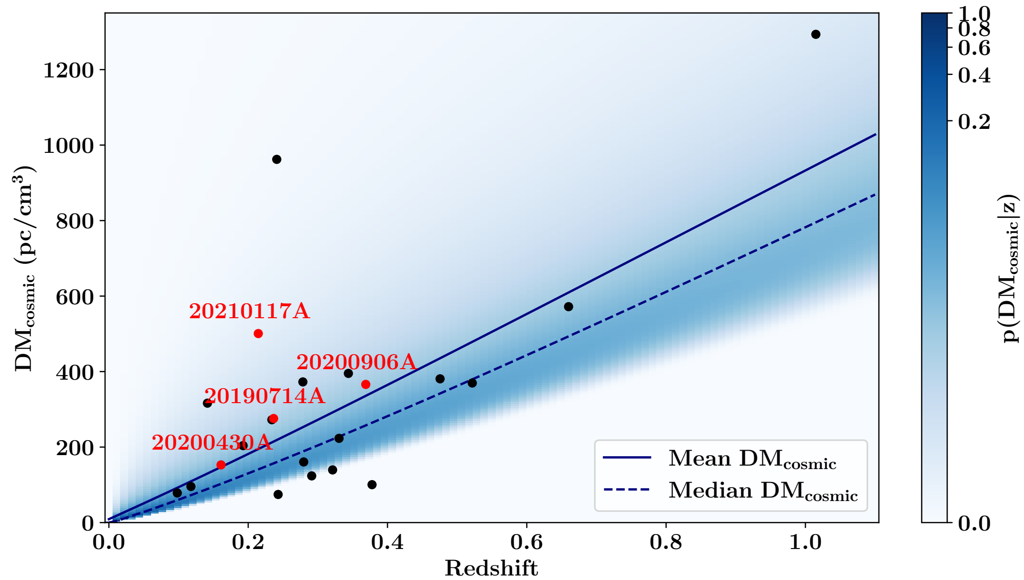

Figure 5.1: An updated Macquart relation plot including published well-localized FRBs from CRAFT at $z \lesssim 1$. The solid line is the mean $\langle \mathrm{DM_{cosmic}} \rangle$ from a universe with the ΛCDM cosmology, a.k.a. the Macquart relation. The blue shading represents $p(\mathrm{DM_{cosmic}}|z)$, the PDF of $\mathrm{DM_{cosmic}}$ at each redshift given the variance in the matter density along a random sightline in the universe from intervening halos and the gas in the cosmic web filaments. Note the median of the distribution (dashed line) lies lower than the mean, implying that most sightlines are expected to have few intervening foreground halos that contribute significantly to $\mathrm{DM_{cosmic}}$. The data points are estimates $\mathrm{DM_{cosmic}^{est}}$ for FRBs from the CRAFT survey. These are the observed $\mathrm{DM_{FRB}}$ corrected for the Milky Way contribution and an assumed host contribution of $\overline{\mathrm{DM_{host}}} = 186\ \mathrm{pc\,cm^{-3}}$ in the rest frame. The sightlines examined in this work are marked in red, all of which have $\mathrm{DM_{cosmic}^{est}} > \langle \mathrm{DM_{cosmic}} \rangle$. Of the other notably high $\mathrm{DM_{cosmic}^{est}}$ sources, FRB20190520B ($z_{\mathrm{FRB}} \sim 0.23$) at $\sim 1000\ \mathrm{pc\,cm^{-3}}$ will be analyzed in a future work.

5.2 Data

5.2.1 Sample selection

As described in the introduction, structure in the cosmic web is expected to produce a significant scatter in the Macquart relation due to sightline-to-sightline variation in the column density of intervening gas (Macquart et al., 2020). Figure 5.1 is an updated plot showing the Macquart relation and data from the sample of CRAFT-localized FRBs published to date (Macquart et al., 2019; Bhandari et al., 2019; Qiu et al., 2019; James et al., 2022a). The DM values shown in the plot correspond to estimates of the cosmic dispersion measures,

$$\mathrm{DM}_{\mathrm{cosmic}}^{\mathrm{est}} = \mathrm{DM}_{\mathrm{FRB}} - \mathrm{DM}_{\mathrm{MW}} - \overline{\mathrm{DM}_{\mathrm{host}}}/(1+z), \tag{5.3}$$

where $\mathrm{DM}_{\mathrm{MW}}$ is estimated as the sum of the ISM contribution ($\mathrm{DM}_{\mathrm{MW,ISM}}$) taken from the NE2001 model (Cordes & Lazio, 2003b), and the halo contribution ($\mathrm{DM}_{\mathrm{MW,halo}}$) which is assumed to be 40 $\mathrm{pc\,cm^{-3}}$. We do note that there is evidence pointing to a highly variable Milky Way halo contribution, $\mathrm{DM}_{\mathrm{MW,halo}}$. i.e. $\sigma(\mathrm{DM}_{\mathrm{MW,halo}}) \sim 100\ \mathrm{pc\,cm^{-3}}$. For example, Das et al. (2021) use X-ray absorption lines in quasar spectra from gas within the Milky Way CGM and constrain $\mathrm{DM}_{\mathrm{MW,halo}}$ along numerous sightlines. Though we did not find a matching absorption sightline from their dataset within 3 degrees of our FRBs we acknowledge the possibility of large $\mathrm{DM}_{\mathrm{MW,halo}}$. Studies such as Cook et al. (2023) and Ravi et al. (2023) involving low $\mathrm{DM}_{\mathrm{FRB}}$ sightlines ($\lesssim 100\ \mathrm{pc\,cm^{-3}}$) place tighter constraints ($\mathrm{DM}_{\mathrm{MW,halo}} = 28-111\ \mathrm{pc\,cm^{-3}}$). In this context, we concede our assumption for $\mathrm{DM}_{\mathrm{MW,halo}}$ is probably low but has little impact on our qualitative findings. Furthermore, for Figure 5.1, we assume a median host contribution of $\overline{\mathrm{DM}_{\mathrm{host}}} = 186\ \mathrm{pc\,cm^{-3}}$ (James et al., 2022b). A primary goal of this paper is to distinguish between these two scenarios, i.e. the excess arising from the foreground or the FRB host, along individual sightlines.

The blue shading visualizes the expected probability density of $\mathrm{DM}_{\mathrm{cosmic}}$ at each redshift, $p(\mathrm{DM}_{\mathrm{cosmic}}|z)$, with an assumed feedback parameter $F = 0.31$ (Macquart et al., 2020; McQuinn, 2014b). The long, low-probability tail in $p(\mathrm{DM_{cosmic}}|z)$ to high $\mathrm{DM_{cosmic}}$ values is due to massive halos of galaxy clusters and groups, which occasionally intersect a sightline. One sees that a sizable fraction of the FRB sample lies above the Macquart relation, and a subset have $\mathrm{DM^{est}_{cosmic}}$ values at or beyond the 80th percentile of the expected distribution at their redshifts. Naively, assuming that our ansatz for $\overline{\mathrm{DM_{host}}}$is correct, one would expect only 20% (i.e. ~ 4) of the sightlines on average above the 80th percentile for the sample size shown in the figure. However, we find 11.

The FRBs with $\mathrm{DM^{est}_{cosmic}} > \langle \mathrm{DM_{cosmic}} \rangle$ may arise from higher host contributions than the assumed average (i.e. $\mathrm{DM_{host}} > \overline{\mathrm{DM_{host}}}$), or a larger than average foreground contribution to $\mathrm{DM_{cosmic}}$, or both. Of the 11 FRBs with this apparent excess in $\mathrm{DM_{cosmic}}$, 6 have been targeted in the FLIMFLAM survey and have both shallow, wide-field ($m_r < 20$ mag within 1.1 deg radius around the FRB) AAT/AAOmega spectroscopy, plus deeper, narrow-field spectra ($m_r < 23$ within ∼5 arcmin radius) using the Keck/LRIS and Keck/DEIMOS instruments. One field, FRB20190608A was previously studied by Simha et al. (2020) using redshift data from SDSS and KCWI integral-field unit observations. In a separate paper, we will use a slightly different methodology to analyze the foreground contribution to the well-studied high-DM source FRB20190520B (Lee et al., in prep). In this work, we present the foreground analysis of the other four fields: FRB20190714A, FRB20200430A, FRB20200906A and FRB20210117A. All of these have $\mathrm{DM^{est}_{cosmic}}$ near or beyond the 80th percentile in $p(\mathrm{DM_{cosmic}}|z)$ as listed in Table 5.1.

Table 5.1: Sample of excess DM sightlines in this work.

FRB	RA deg	Dec deg	Redshift	DM_{FRB} $pc\,cm^{-3}$	$\langle DM_{cosmic}\rangle$ $pc\,cm^{-3}$	DM^{est}_{cosmic} $pc\,cm^{-3}$	Percentile
FRB20190714A	183.97971	-13.02100	0.2365	504.1	205	275	88
FRB20200430A	229.70642	12.37675	0.1610	380.0	137	152	81
FRB20200906A	53.49617	-14.08318	0.3688	577.8	326	366	82
FRB20210117A	339.97929	-16.15142	0.2145	731.0	185	502	97

Notes: $\langle DM_{cosmic}\rangle$ is the mean DM_{cosmic} at the FRB redshift. DM^{est}_{cosmic} is the estimated DM_{cosmic} value for the FRB based on DM_{FRB} and an assumed $\overline{DM_{host}} = 186$ $pc\,cm^{-3}$. Percentile is the percentage of FRBs expected to have $DM_{cosmic} < DM^{est}_{cosmic}$ at the FRB redshift.

5.2.2 Spectroscopic target selection

Field galaxies within a radius of 1.1 degrees of the sightlines were targeted using the fiber-fed AAOmega spectrograph on the 3.9m Anglo-Australian Telescope (AAT) at Siding Spring, Australia. For two fields (FRB20190714A and FRB20210117A), the fiber configurations were designed to target sources with $m_r < 19.4$ mag that were well-resolved in the Pan-STARRS imaging, i.e. distinct from point sources. For fields FRB20200430Aand FRB20200906A, the target criterion is $m_r < 19.2$ mag and $m_r < 19.8$ mag respectively that were well-resolved in DECam imaging from archival DESI Legacy Imaging Surveys data (Dey et al., 2019). Due to unfavorable weather conditions, we were unable to observe the full roster of fiber configurations generated for FRB20200430A, and so this field has sparser wide-field coverage than intended. We therefore supplement our spectroscopic data on this field from the SDSS database. Each fiber configuration was observed for ~ 1 hr in the 1x1 binning mode with the 570 nm dichroic, which split the light into red and blue components. The red camera used the 385R grating blazed at 720nm while the blue camera used the 580V grating and the blaze is set to 485nm. The red and blue spectra were reduced, coadded and combined using the 2dFDR version 6.2 based on python 2.7 kindly provided by the OzDES group (Yuan et al., 2015; Childress et al., 2017). We used the MARZ (Hinton et al., 2016) software to determine redshifts, which cross-correlates the input spectra with a set of templates and determines the best redshift. This was followed by a visual inspection to confirm the redshifts, with adjustments as necessary. Figure 5.2 shows the histogram of redshifts obtained from the AAT for the fields analyzed in this paper. The spectroscopic success rate of the survey, which is defined as the fraction of the number of targets with secure redshifts relative to the total number of the targets that were observed, is around 90%.

In addition, the FRB fields were targeted with the Keck DEIMOS and LRIS spectrographs in the multi-object spectroscopy mode. We used Pan-STARRS r-band imaging to select $m_r < 23$ mag galaxies (i.e. as before, rejecting point sources) within ~ 5 arcmin of the sightline. To further limit sources to $z \lesssim 0.3$, we rejected sources that satisfy these color criteria based on our analysis of mock galaxy photometry (Lee et al., 2022):

$$\begin{aligned} g - r &> 0 \\ r - i &> 0.7 \\ i &> 20.5 \end{aligned} \tag{5.4}$$

With LRIS, multi-object slitmask-based spectroscopy of the target galaxies was performed. Our configuration was as follows: 600/7500 grating for the red side, 600/4000 grism for the blue side and the 560D dichroic. All raw frames were binned 2x2. The LRIS observations were obtained only for the fields of FRB20190714A and FRB20200430A during a previous run and not all objects in the field could be covered due to limited time. The galaxies that were omitted were subsequently targeted with DEIMOS. All LRIS/DEIMOS spectra were reduced with v1.2 of the PypeIt package (Prochaska et al., 2020) package. We set a detection threshold of 3σ above the noise floor for object identification and forced detection for fainter objects using the slitmask information stored in the metadata of the raw frames. Our DEIMOS observations were obtained on a later run with the 600ZD grating and GG455 order blocking filter and

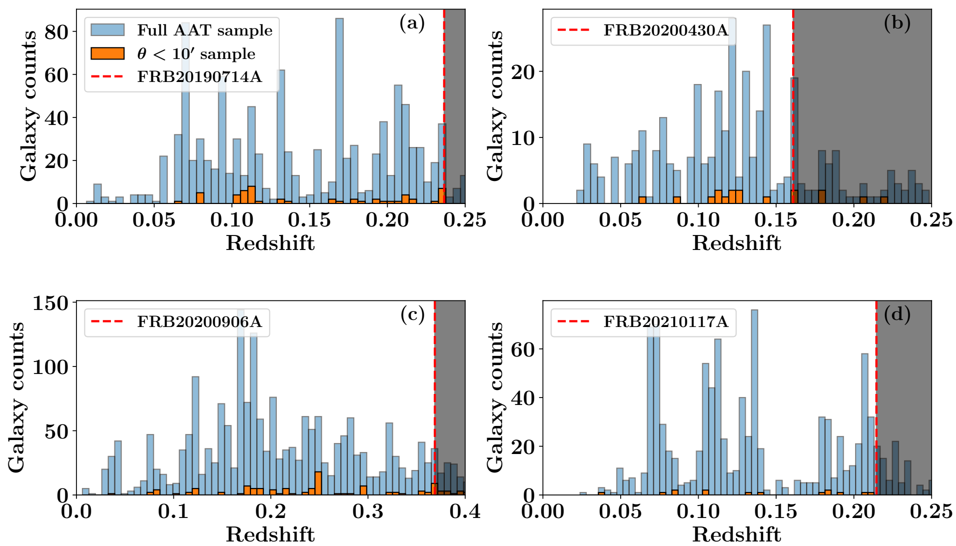

Figure 5.2: Histogram of galaxy redshifts obtained from the AAOmega spectrograph in the four fields. The full 1.1 degree radius sample is shown in blue and the subset of galaxies within 10 arcmin is shown in orange. The FRB redshift is marked by the dashed red line, and the shaded region represents background galaxies that are not relevant to this study

1x1 binning. Each mask configuration was observed for ~ 50 min. Together, 95% of the candidate galaxies within 5 arcmin of the FRB were targeted.

We ignored the serendipitous spectra, i.e. spectra of non-targeted sources captured in our slits, as they generally had no discernible features for redshift assignment. We did not flux-calibrate the spectra as this is not necessary for redshift estimation from line features.

As with the AAT spectra, all reduced spectra from Keck were processed via MARZ (Hinton et al., 2016) to determine redshifts, followed by a visual inspection. As with the AAT data, $> 90\%$ of the targeted Keck spectra had good redshift assignments.

In the case of FRB20190714A, Marnoch (2023, in prep.,) present a MUSE

IFU pointing of 0.67 hours with the Wide Field Mode (WFM) covering the $1' \times 1'$ area around the FRB sightline. Of the 61 galaxies extracted from the stacked white light image (i.e. the image averaged over the spectral dimension), 7 were identified to be foreground sources.

The reduced spectra with their assigned redshifts are made available via Zenodo [2].

5.2.3 Photometric data

To estimate foreground galaxy properties such as stellar mass, we fit the publicly available flux measurements with a spectral energy distribution (SED) model. To this end, we used the *grizy* photometry from the Pan-STARRS (Kaiser et al., 2010) catalog, *W1*, *W2*, *W3*, and *W4* from the WISE All-Sky source catalog (Wright et al., 2010) and supplemented with the *YJHKs* photometry from the VISTA Hemisphere Survey (VHS) catalog (Arnaboldi et al., 2007) where available. The details regarding the SED fitting procedure are elucidated in the following section.

5.3 DM halo analysis

In this section, we describe the methodology implemented to estimate the dispersion measure contributed from the halo of a galaxy or group of galaxies, $\mathrm{DM_{halo}}$. We refer to the summed quantity along a given sightline as $\mathrm{DM_{halos}}$.

[2]Available at this Zenodo DOI: 10.5281/zenodo.7991632

5.3.1 Individual Halos

Once spectroscopic redshifts were assigned, the available photometry was fit with an SED using CIGALE (Noll et al., 2009). We assumed a delayed-exponential star formation history with no burst population, a synthetic stellar population prescribed by Bruzual & Charlot (2003), the Chabrier (2003) initial mass function (IMF), dust attenuation models from Calzetti (2001), and dust emission templates from Dale et al. (2014), where the AGN fraction was capped at 20%. This provided an estimate of the stellar mass, M_*, of the foreground galaxy at a given redshift $z_{\rm fg}$.

We then translate M_* to galactic halo mass, $M_{\rm halo}$, using the mean stellar-to-halo mass relation (SHMR) described by Moster et al. (2013) at that $z_{\rm fg}$. Subsequently, $\mathrm{DM}_{\rm halo}$ was estimated using the Prochaska & Zheng (2019) modified NFW halo profile model. We assumed that the total amount of baryons in the halo traces the cosmic mean (Ω_b/Ω_m). We assumed the halo gas extends to one virial radius (r_{vir}) and that 75% of the baryons are in the hot, ionized phase in the halo. This assumes that 25% of the baryons in the galaxy are in condensed forms (e.g. stars and neutral gas; see Fukugita et al., 1998). While this fraction may vary with halo properties (e.g. Behroozi et al., 2010) or assumptions on galaxy feedback (Sorini et al., 2022; Ayromlou et al., 2022), we emphasize that this is a relatively conservative maximal model for the CGM of galaxies, i.e. one may consider the DM estimates as upper limits. Adopting this CGM model, we then integrate the dispersion measure of the gas at the observed impact parameter $R_\perp$ of the galaxy from the sightline determined from its redshift $z_{\rm fg}$ and the angular offset.

The uncertainties in the M_* estimation and the SHMR relation propagate into the $\mathrm{DM_{halos}}$ estimate. For each galaxy, we assumed that the $\log M_*$ distribution at a given redshift was Gaussian with the mean and standard deviations obtained from CIGALE. Accounting for the error in the SHMR is more involved as it depends on both M_* and galaxy redshift. The SHMR is described in Equation 2 of Moster et al. (2013) with 8 parameters. We took the best fit parameters and uncertainties from their Table 1 as the mean and standard deviations of the independent normal distributions that these parameters were sampled from. We ignored any co-variance in these fit parameters. From the $\log M_*$ distributions, 1000 samples are drawn and the SHMR parameter space is sampled 1000 times for each $\log M_*$ realization. Thus, for every galaxy, we produce 10^6 $\log M_{\mathrm{halo}}$ realizations, and subsequently, $\mathrm{DM_{halo}}$ estimates. The mean and variance from these individual distributions are used when drawing our conclusions for the sightlines.

5.3.2 Galaxy group contributions

It is important to account for galaxy groups or clusters, since the overall halo mass is typically much larger than the sum of the putative member masses if estimated individually. This results in DM contributions much greater than that estimated for individual group members. To search for galaxy groups within the FLIMFLAM spectroscopic catalog, we make use of an anisotropic friends-of-friends (FoF) group finder that has previously been applied to SDSS galaxy survey data (Tago et al. 2008; but see also Tempel et al. 2012,Tempel et al. 2014). This finder assumes a transverse linking length, $d_{\mathrm{LL},\perp}$, which varies as a function of redshift, z, in the following way:

$$d_{\mathrm{LL},\perp}(z) = d_{\mathrm{LL},0}[1 + a \arctan(z/z_*)], \tag{5.5}$$

where $d_{\mathrm{LL},0}$ is the linking length at the initial redshift, whereas a and z_* are parameters governing the redshift evolution. This redshift-dependent linking length allows one, in principle, to account for the declining completeness of the galaxies with increasing redshift in a flux-limited spectroscopic survey. The line-of-sight linking length, $d_{\mathrm{LL},\parallel}$, is then set as a fixed multiple of $d_{\mathrm{LL},\perp}$; the ratio $d_{\mathrm{LL},\parallel}/d_{\mathrm{LL},\perp}$ is another free parameter for the group finder. To determine the appropriate values for these free parameters, we ran the group finder on the FLIMFLAM catalogs and manually iterated the free parameters of the group finder, while visually inspecting the resulting groups from the FLIMFLAM catalog in both the transverse and line-of-sight dimensions at each iteration. Our criteria was to ensure the selection is not so permissive as to include cosmic web filament structures as part of the identified groups, while simultaneously not being so stringent as to omit the more massive groups at the high-redshift end where the data is typically sparser. We arrived at the following values for the group-finding in this paper: $d_{\mathrm{LL},\perp} = 0.2\,h^{-1}\,\mathrm{Mpc}$, $a = 0.75$, $z_* = 0.1$, and $d_{\mathrm{LL},\parallel}/d_{\mathrm{LL},\perp} = 10$.

To limit ourselves to reasonably robust groups, we select for a minimum richness of $N_{\mathrm{gal}} \geq 5$. Furthermore, we apply the same modified NFW profile model; limited still to one virial radius but scaled up to the group mass estimated as our fiducial model. In addition to the coordinates and redshift of each group center, the code also provides a halo mass estimate by applying the virial theorem on the projected group radius and velocity dispersion[3].

[3]The group catalogs generated for our fields are available at this Zenodo DOI: 10.5281/zenodo.7991632

5.3.3 Halo Contributions

While our analysis can provide estimates of $\mathrm{DM_{halos}}$ for individual sightlines, it is useful to compare them against a mean cosmic contribution from halos for any random sightline up to z_{FRB}. One may produce a theoretical estimate of this as follows.

Adopting the halo mass function (HMF, using the implementation of McClintock et al. (2019)) and restricting ourselves to $M_{\mathrm{halo}} < 10^{16}$ $\mathrm{M_\odot}$, we can estimate the total number of halos of each mass bin expected to intersect within 1 r_{vir} of each sightline. Using our baryon distribution model described in section 5.3, this can be translated to the average $\mathrm{DM_{halos}}$ along the sightline, i.e. $\langle \mathrm{DM_{halos}} \rangle$.

$\langle \mathrm{DM_{halos}} \rangle$ monotonically increases with the halo mass up to which the HMF is integrated over (see Figure 5.3) but plateaus near $M_{\mathrm{halo}} \approx 10^{15}\mathrm{M_\odot}$. This presumably reflects the low average probability of intersecting such massive, but rare, halos. Changing the model parameters that influence $\mathrm{DM_{halo}}$ have similar effect on $\langle \mathrm{DM_{halos}} \rangle$. e.g. increasing the assumed fraction of ionized baryons in the halo scales up both $\mathrm{DM_{halo}}$ and $\langle \mathrm{DM_{halos}} \rangle$ by the same factor.

5.4 Results

The analysis described above was applied to each galaxy in each field, resulting in probability distributions for the $\mathrm{DM_{halos}}$ contribution of individual galaxies and groups. The $\mathrm{DM_{halos}}$ value is then the straight sum along each sightline. Our findings from the analysis for each sightline described above are presented in this section.

Figure 5.4 is a visual summary of the individual fields. It highlights stars,

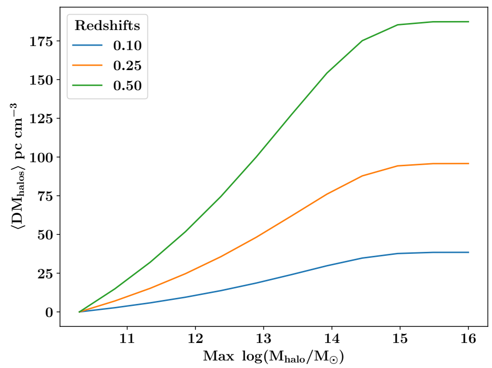

Figure 5.3: Cumulative estimate of $\langle \mathrm{DM_{halos}} \rangle$ as a function of the maximum halo mass that can contribute to $\mathrm{DM_{halos}}$. $\langle \mathrm{DM_{halos}} \rangle$ is computed assuming the halo mass function corresponding to our adopted cosmology (McClintock et al., 2019), integrated to the given maximum M_{halo} from the same minimum $M_{\mathrm{halo}} = 10^{10.3}\,\mathrm{M_\odot}$. The halo gas model has the same modified NFW profile described previously, extending to one virial radius with 75% of the halo baryons in the hot, ionized phase.

background objects and foreground objects within $\lesssim 3$ arcmin of the FRBs on the r-band image of the field from Pan-STARRS. The foreground objects are colored by the average $\mathrm{DM_{halo}}$ contribution estimated for each of them.

5.4.1 FRB20190714A

Examining Figure 5.4, one notes multiple galaxies in the foreground field of FRB20190714A including several within $\approx 30''$. These galaxies lie primarily at two redshifts: $z = 0.10$ and 0.21 and have estimated halo masses that yield significant $\mathrm{DM_{halo}}$ contributions. The galaxy with the smallest impact parameter (J121554.90-130121.95) was found in the VLT/MUSE datacube and has a redshift of 0.08, yielding a projected perpendicular distance of $R_\perp = 11\,\mathrm{kpc}$ (Marnoch, 2023, in prep.). Even though its mass estimate indicates it is a dwarf galaxy ($M_* = 10^{8.5}\ \mathrm{M_\odot}$), its close proximity to the sightline leads to a substantial $\mathrm{DM_{halo}}$ contribution of $25\,\mathrm{pc\,cm^{-3}}$.

Table 5.2: Foreground galaxies contributing to $\mathrm{DM_{halos}}$.

FRB	RA deg	Dec deg	z_{fg}	$R_{\perp}$ kpc	$\log(\mathrm{M_*/M_\odot})$	$\log(\mathrm{M_{halo}/M_\odot})$	$\mathrm{DM_{halo}}$ $\mathrm{pc\,cm^{-3}}$	$\sigma(\mathrm{DM_{halo}})$ $\mathrm{pc\,cm^{-3}}$
FRB20190714A	184.01105	-13.03391	0.1044	236	10.6	12.2	16.6	16.3
FRB20190714A	183.97902	-13.02895	0.2119	102	10.1	11.7	21.9	10.4
FRB20190714A	183.97876	-13.02276	0.0802	11	8.2	10.7	25.1	4.2
FRB20190714A	183.97849	-13.02450	0.2141	47	9.6	11.4	31.4	20.4
FRB20190714A	183.99997	-13.02000	0.1042	140	10.8	12.4	42.7	29.5
FRB20200430A	229.71715	12.36691	0.1448	135	9.7	11.4	4.8	2.9
FRB20200430A	229.68695	12.36605	0.1109	163	10.5	11.9	21.0	15.0
FRB20200430A	229.69376	12.36773	0.0619	67	10.3	11.8	41.0	12.1
FRB20200906A	53.53467	-14.07823	0.1761	417	11.0	13.1	2.2	5.1
FRB20210117A	339.96901	-16.11978	0.1827	378	10.5	12.0	1.4	4.4
FRB20210117A	339.94438	-16.15251	0.2085	424	10.9	12.8	1.6	4.2

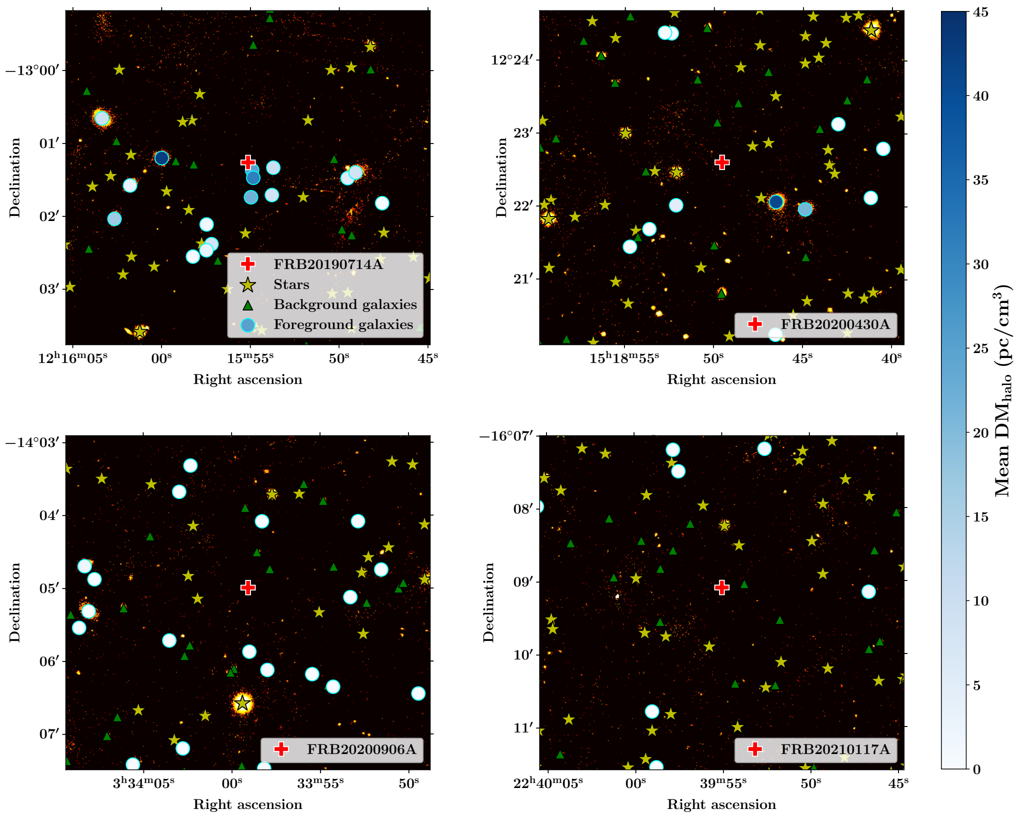

Figure 5.4: Zoomed-in ($5' \times 5'$) illustration of the fields and results for the four FRB sightlines: (a) FRB20190714A, (b) FRB20200430A, (c) FRB20200906A, and (d) FRB20210117A. The background shows Pan-STARRS r-band images. In each image, the red crosses mark the location of the FRB, the green triangles mark the background galaxies and the yellow stars mark the point sources that were ignored from spectroscopic targeting. The blue circles mark the foreground galaxies, with the color scaled according to the estimated DM_{halo} value.

While the projected separation is ~ 10 times larger than the half-light radius (~ 1 kpc as measured from our MUSE data) this is well within the estimated virial radius of the dwarf galaxy (90 kpc).

The wide-field data from Keck/DEIMOS and LRIS show 110 foreground galaxies, and of these 17 show non-zero DM_{halo} contributions. Table 5.2 lists the foreground

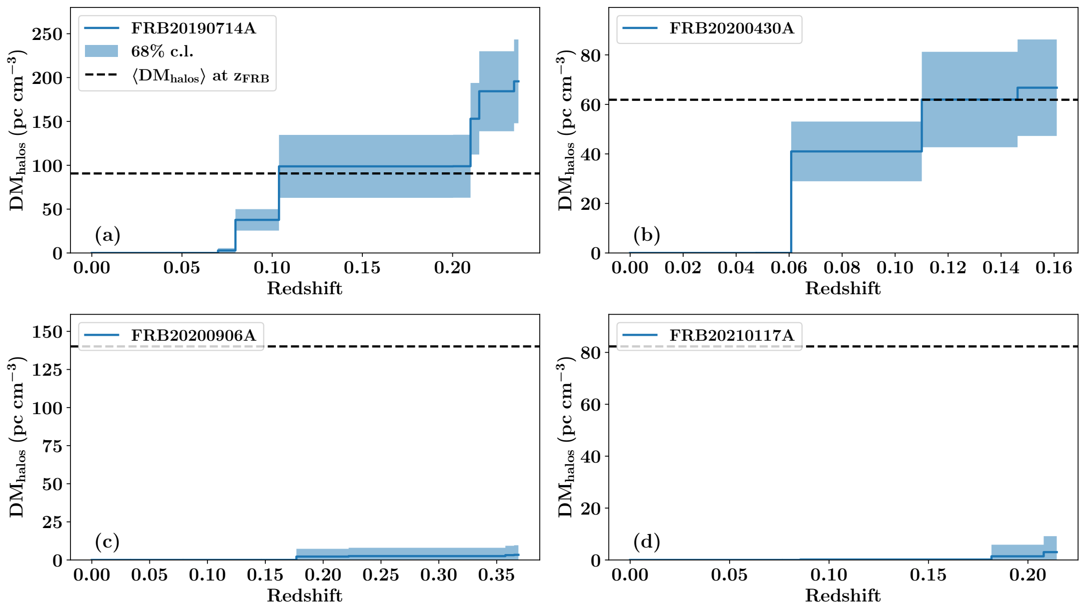

Figure 5.5: Empirical evaluation of $\mathrm{DM_{halos}}$ for the FRB sightlines as a function of redshift. The blue curve presents the cumulative estimation of $\mathrm{DM_{halos}}$ from $z = 0$, which increases monotonically as foreground halos are encountered along the sightline. The blue shading represents 68% confidence limits on the $\mathrm{DM_{halos}}$ estimate, which is the running quadrature sum of the individual 1-sigma limits of the DM distributions for the individual galaxies. The black dashed lines represent estimates for $\langle\mathrm{DM_{halos}}\rangle$ assuming the our adopted halo mass function (up to $M_{\rm halo} = 10^{16}$ $\mathrm{M_\odot}$) and the adopted halo gas distribution model used to calculate $\mathrm{DM_{halos}}$. While the FRB20190714A sightline clearly exceeds the average expectation, both FRB20210117A and FRB20200906A are barely in excess of $\mathrm{DM_{halos}} = 0\,\mathrm{pc\,cm^{-3}}$. FRB20200430A exhibits a $\mathrm{DM_{halos}}$ value consistent with $\langle\mathrm{DM_{halos}}\rangle$.

galaxies and their mean $\mathrm{DM_{halo}}$ contributions [4].

We do not find any group contribution when applying our fiducial halo gas model, which truncates at the virial radius, to the groups identified in this field. If, however, one extended the model to two virial radii we estimate one of the groups would give a $50\,\mathrm{pc\,cm^{-3}}$ contribution. This group is centered at RA/Dec of (184.1382405, −13.0107427) and $z = 0.111$. The FRB sightline is at a transverse distance of 1.16

[4]The full galaxy catalogs with their halo masses and $\mathrm{DM_{halo}}$ estimates for our fields are available at this Zenodo DOI: 10.5281/zenodo.7991632

Mpc. With 20 member galaxies and a halo mass of $10^{13.9}\mathrm{M}_\odot$, this group may potentially contribute to $\mathrm{DM}_{\mathrm{cosmic}}$. We do not include this contribution in our $\mathrm{DM}_{\mathrm{halos}}$ estimate but discuss the implications of doing so in Section 5.5.

Figure 5.5a presents the cumulative sum of $\mathrm{DM}_{\mathrm{halos}}$ with redshift and shows a total value of $200 \pm 45\,\mathrm{pc\,cm^{-3}}$. This exceeds by over $100\,\mathrm{pc\,cm^{-3}}$ the average estimated $\langle\mathrm{DM}_{\mathrm{halos}}\rangle$ for the FRB redshift using the methodology described in Section 5.3.3. For this FRB, we infer that its $\mathrm{DM}_{\mathrm{cosmic}}^{\mathrm{est}}$ exceeds $\langle\mathrm{DM}_{\mathrm{cosmic}}\rangle$ owing to an excess of foreground structure. We return to this conclusion in the following section.

5.4.2 FRB20200430A

While FRB20200430A has the least significant excess value of $\mathrm{DM}_{\mathrm{cosmic}}^{\mathrm{est}}$ in our sample, we estimate that the foreground galaxies in the field of FRB20200430A contribute significantly to $\mathrm{DM}_{\mathrm{halos}}$, similar to FRB20190714A. Specifically, we estimate $\mathrm{DM}_{\mathrm{halos}} = 65 \pm 20\,\mathrm{pc\,cm^{-3}}$ which is comparable to $\langle\mathrm{DM}_{\mathrm{halos}}\rangle$ at $z_{\mathrm{FRB}} = 0.161$ (Fig. 5.5b).

We do not find any group contribution to $\mathrm{DM}_{\mathrm{halos}}$ for this sightline; the closest group lies at 4.6 Mpc transverse distance with a mass of only $10^{13}\,\mathrm{M}_\odot$. At over $\sim$10 virial radii from the sightline, this group has no plausible influence on the observed $\mathrm{DM}_{\mathrm{halos}}$.

Gordon et al. (2023) estimate the stellar mass of the host to be $10^{9.3}\,\mathrm{M}_\odot$ and the SFR to be 0.11 $\mathrm{M}_\odot$/yr. They identify the host as being on the star-forming main sequence. Heintz et al. (2020) do not detect any distinct host morphology from Keck imaging. The localization region reported in their work is comparable to the size of the galaxy and thus it is not possible to obtain robust constraints on the host ISM constribution to $\mathrm{DM}_{\mathrm{host}}$.

5.4.3 FRB20200906A

Although this field exhibits a large number of foreground galaxies within $10'$ of the FRB including nearly 20 within $5'$ of the sightline, we estimate their contributions $\mathrm{DM}_{\mathrm{cosmic}}$ to be nearly negligible. Many of these galaxies also have high estimated halo masses but their individual contributions are generally $\mathrm{DM}_{\mathrm{halo}} \lesssim 1\ \mathrm{pc\,cm^{-3}}$ (Table 5.2). This results from the the large physical impact parameters; only one has $R_\perp < 200\,\mathrm{kpc}$ from the sightline.

We estimate no group contribution to $\mathrm{DM}_{\mathrm{halos}}$ for this field, with the closest group being 860 kpc away with a mass of $10^{11.7}\mathrm{M}_\odot$ ($z = 0.04$). This comparatively low-mass halo was detected as a group only by virtue of its low redshift (and hence small distance modulus).

Gordon et al. (2023) estimate the stellar mass of the host to be $10^{10.3}\ \mathrm{M}_\odot$ and the SFR to be 5.4 $\mathrm{M}_\odot$/yr. They identify the host as also being on the star-forming main sequence. Gordon et al. (2023) and Bhandari et al. (2022) show that the localization region is on the outskirts of the galactic disk which might imply a low host ISM contribution to $\mathrm{DM}_{\mathrm{host}}$. A higher resolution study using an IFU might yield better constraints on $\mathrm{DM}_{\mathrm{host}}$(e.g. Chittidi et al., 2021).

5.4.4 FRB20210117A

From our sample of four FRBs with $\mathrm{DM}_{\mathrm{cosmic}}^{\mathrm{est}} > \langle\mathrm{DM}_{\mathrm{cosmic}}\rangle$, FRB20210117A is the most extreme outlier with more than $380\,\mathrm{pc\,cm^{-3}}$ in excess of the average value at the $z_{\mathrm{FRB}} = 0.2145$. Remarkably, as is evident from Figure 5.4b, we do not find any foreground halos in close proximity to the sightline. As such, the total $\mathrm{DM}_{\mathrm{halos}}$ estimate is very small (Figure 5.5b). The galaxy with the largest $\mathrm{DM}_{\mathrm{halo}}$ estimate (1.6 $\mathrm{pc\,cm^{-3}}$) is over 400 kpc away and has a halo mass of $10^{12.8}\mathrm{M}_{\odot}$. Given the uncertainties in halo masses, $\mathrm{DM}_{\mathrm{halos}}$ is even consistent with 0, i.e. no intersections within one virial radius of any foreground halo.

Not surprisingly, we also find no contribution from the galaxy groups identified in this field. The closest group lies at a distance of 2 Mpc.

5.5 Discussion

In the previous section we presented our analysis of the foreground matter distribution along four sightlines, with a focus on $\mathrm{DM}_{\mathrm{halos}}$. We now discuss the implications of these results. The primary motivation of this paper was to explore the origin of apparent excesses in $\mathrm{DM}_{\mathrm{cosmic}}$ along FRB sightlines. To place our results in this context, we construct an empirical model $\mathrm{DM}_{\mathrm{cosmic}}^{\mathrm{model}}$ for the four sightlines based on our findings. Specifically, we define

$$\mathrm{DM}_{\mathrm{cosmic}}^{\mathrm{model}} = \mathrm{DM}_{\mathrm{halos}} + \langle\mathrm{DM}_{\mathrm{IGM}}\rangle \tag{5.6}$$

where $\langle\mathrm{DM}_{\mathrm{IGM}}\rangle$ is given by

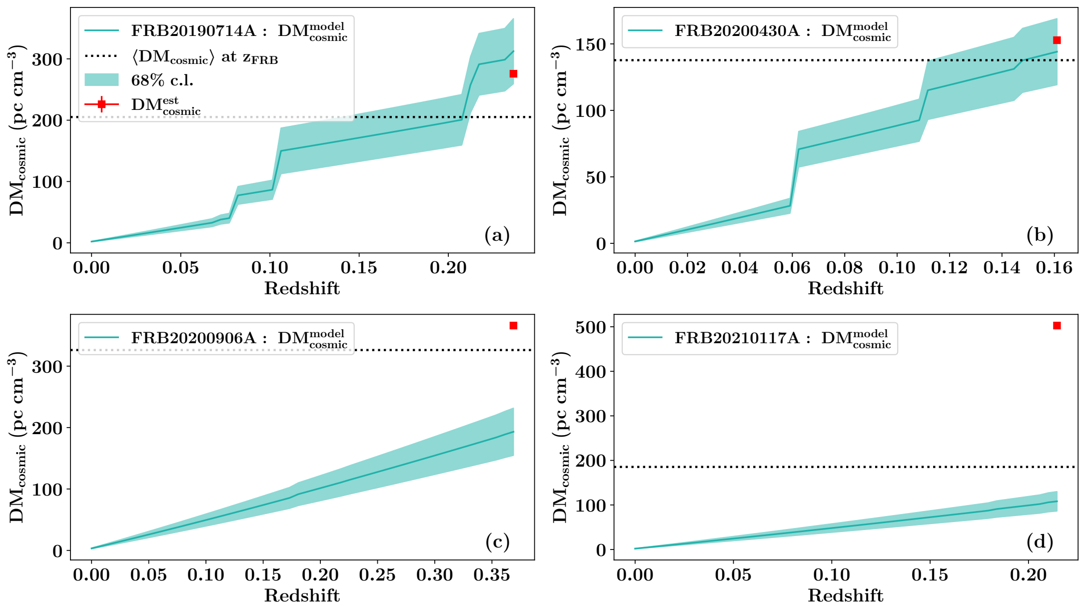

Figure 5.6: Estimates of $\mathrm{DM}_{\mathrm{cosmic}}$ for the FRB sightlines as a function of redshift. The solid, teal curve is $\mathrm{DM}^{\mathrm{model}}_{\mathrm{cosmic}}$, a sum of $\mathrm{DM}_{\mathrm{halos}}$, i.e. the solid, blue curve from Figure 5.5 and an estimate of the average IGM contribution to $\mathrm{DM}_{\mathrm{cosmic}}$ (see text for details). The dotted line shows $\langle\mathrm{DM}_{\mathrm{cosmic}}\rangle$ at z_{FRB} in each subplot. The shading around the solid curve represents a 68% confidence limit which includes an assumed 20% uncertainty for $\langle\mathrm{DM}_{\mathrm{IGM}}\rangle$ in quadrature with the uncertainties from Figure 5.5. The red point is an estimate of $\mathrm{DM}_{\mathrm{cosmic}}$ for each FRB taken from Figure 5.1, i.e. by subtracting the assumed host and Milky Way contributions.

$$\langle\mathrm{DM}_{\mathrm{IGM}}\rangle = \langle\mathrm{DM}_{\mathrm{cosmic}}\rangle - \langle\mathrm{DM}_{\mathrm{halos}}\rangle \tag{5.7}$$

with $\langle\mathrm{DM}_{\mathrm{halos}}\rangle$ calculated as described in Section 5.3.3 and all quantities are evaluated at z_{FRB}. In future analyses the FLIMFLAM survey will estimate $\mathrm{DM}_{\mathrm{IGM}}$ for individual fields with the cosmic web reconstruction algorithm ARGO (Ata et al., 2015), which is a Bayesian estimator for the matter density field given the foreground galaxy halo masses and 3D locations (i.e. their sky position and redshifts).

Our $\mathrm{DM}^{\mathrm{model}}_{\mathrm{cosmic}}$ estimate assumes the uncertainty in $\mathrm{DM}_{\mathrm{halos}}$ (Table 5.3) and a 20% statistical uncertainty in $\langle\mathrm{DM}_{\mathrm{IGM}}\rangle$ based on numerical simulations (e.g. Lee et al., 2022) We also emphasize that the assumed CGM model used to estimate $\mathrm{DM_{halos}}$ impacts $\langle\mathrm{DM_{halos}}\rangle$ and therefore $\langle\mathrm{DM_{IGM}}\rangle$ through Equation 5.7. This sensitivity to the CGM model (here a systematic error) lies central to correlating $\mathrm{DM_{FRB}}$ against galactic halos and large-scale structure to constrain properties of halo gas and the baryonic content of the IGM (Lee et al., 2022; Rafiei-Ravandi et al., 2021). In the current analysis, however, the CGM model has less impact for decreases in $\mathrm{DM_{halos}}$ and will be compensated by an increase in $\langle\mathrm{DM_{IGM}}\rangle$.

Figure 5.6 presents cumulative estimates for $\mathrm{DM_{cosmic}^{model}}$ with redshift for each field. These are compared with $\langle\mathrm{DM_{cosmic}}\rangle$ at z_{FRB} and our values for $\mathrm{DM_{cosmic}^{est}}$ using Equation 5.3. As one may have anticipated, $\mathrm{DM_{cosmic}^{model}}$ for the two fields with large $\mathrm{DM_{halos}}$ values (FRB20190714A, FRB20200430A) are consistent with $\mathrm{DM_{cosmic}^{est}}$ (see also Table 5.3). For these two FRBs, we have empirical confirmation of the theoretical paradigm for $\mathrm{DM_{cosmic}}$, i.e. that its intrinsic scatter tracks the incidence of foreground structure. These results lend further confidence for future analyses leveraging $\mathrm{DM_{FRB}}$ to resolve the cosmic web. Furthermore, the FRB20190714A sightline likely intersects the group environment of a galaxy group at a transverse distance of 1.16 Mpc, potentially implying an additional 50 $\mathrm{pc\,cm^{-3}}$ attributed to foreground structure. Indeed, this can commensurately reduce the inferred $\mathrm{DM_{host}}$. We intend to further examine the field in our future work. Compared to the previously studied sightlines of FRB20190608A (Simha et al., 2020) and FRB20180924B (Simha et al., 2021), FRB20190714A is the first that shows a significantly large contribution from foreground halos. As mentioned previously, such sightlines are expected to be rare (e.g. McQuinn, 2014b).

On the other hand, the $\mathrm{DM_{cosmic}^{model}}$ estimates for FRB20200906A and

FRB20210117A do not even meet the average $\langle \mathrm{DM}_{\mathrm{cosmic}} \rangle$ for these sources, much less the apparent excess implied by $\mathrm{DM}^{\mathrm{est}}_{\mathrm{cosmic}}$. The shortfalls are $\approx 200\,\mathrm{pc\,cm^{-3}}$ and $\approx 425\,\mathrm{pc\,cm^{-3}}$ respectively. Even accounting for uncertainty in our $\mathrm{DM}_{\mathrm{halos}}$ and $\mathrm{DM}_{\mathrm{IGM}}$ estimates, one cannot account for these differences within the $\sim 1\sigma$ uncertainties. This suggests the observed excess is due to a higher than average $\mathrm{DM}_{\mathrm{host}}$ component; we estimate the rest-frame $\mathrm{DM}_{\mathrm{host}}$ values to be $\approx 422\,\mathrm{pc\,cm^{-3}}$ and $\approx 665\,\mathrm{pc\,cm^{-3}}$ respectively. These sightlines are remarkably similar to that reported by Niu et al. (2022) for FRB20190520B, implying a relatively low $\mathrm{DM}_{\mathrm{cosmic}}$ compared to $\mathrm{DM}_{\mathrm{host}}$ for these sightlines. Future detection of such sightlines might be key to unraveling the likely progenitor scenarios and in investigating how $\mathrm{DM}_{\mathrm{host}}$ depends on host galaxy properties. The $\mathrm{DM}_{\mathrm{host}}$values for FRB20190714A and FRB20200430A are 140 $\mathrm{pc\,cm^{-3}}$ and 196 $\mathrm{pc\,cm^{-3}}$ respectively.

We may further assess the likelihood of this conclusion as follows. Adopting a lognormal PDF for $\mathrm{DM}_{\mathrm{host}}$ with the parameters estimated by James et al. (2022b), the fraction of FRBs with $\mathrm{DM}_{\mathrm{host}}$ values in excess of these estimates are 18% and 9% respectively. The large $\mathrm{DM}_{\mathrm{host}}$ values can be attributed to a combination of the local progenitor environment and the host ISM.

One may search for signatures of a high $\mathrm{DM}_{\mathrm{host}}$ value from detailed studies of the host galaxies. FRB20210117A arises in a low-mass (dwarf) galaxy with a low star-formation rate (Bhandari et al., 2023; Gordon et al., 2023). It is offset from the galaxy center by $\approx 3\,\mathrm{kpc}$ which exceeds the half-light radius. In these regards, there is nothing apparent in the host properties nor its inferred halo that would suggest such a large $\mathrm{DM}_{\mathrm{host}}$ value. Bhandari et al. (2023) propose a possible scenario involving the

FRB progenitor being embedded in the outflows of a hyper-accreting black hole and note that long-term, short-cadence observations of the FRB polarization may constrain such a model should the FRB be observed to repeat.

FRB20200906A on the other hand arises from a high mass, high star formation rate galaxy and is coincident with the disk of the host (see Figure 1 of Gordon et al., 2023). This implies a fraction of the $\mathrm{DM_{host}}$ arises from the host ISM. For example, Chittidi et al. (2021) estimated for FRB20190608B $\sim 90\ \mathrm{pc\,cm^{-3}}$ for the host ISM contribution from the local Hα line emission measure. While Gordon et al. (2023) report a slightly lower star formation rate for the host of FRB20200906A than for FRB20190608B, one can visually discern a higher disk inclination for the former, and speculate a comparable if not higher $\mathrm{DM_{host}}$ for the ISM component. A dedicated optical follow-up study of the host with an integral-field unit, especially if one can resolve $\lesssim$ 1kpc around the FRB, could help place upper limits on the ISM contribution. As for the halos of all the four FRB host galaxies, if we applied our galaxy halo gas model and computed $\mathrm{DM_{halo}}$ as analyzed above, we estimate a contribution of $\lesssim 35\ \mathrm{pc\,cm^{-3}}$ each.

As mentioned previously, a full IGM reconstruction analysis is necessary for a complete understanding of the foreground matter density, e.g. as done for FRB20190608B (Simha et al., 2020). While we have established two of our fields have $\mathrm{DM_{cosmic}^{model}} \sim \mathrm{DM_{cosmic}^{est}}$, it is possible that the IGM reconstruction may reveal $\mathrm{DM_{IGM}} > \langle\mathrm{DM_{IGM}}\rangle$ and therefore lay tighter constraints on $\mathrm{DM_{host}}$. With ~ 30 sightlines, the FLIMFLAM survey will perform such an analysis and render, as a useful by-product, a posterior distribution for $\mathrm{DM_{host}}$. This distribution can serve as a prior to future

FRB-based IGM tomography work as well as to constrain FRB progenitor channels.

5.6 Conclusions

To summarize, we analyzed the galaxies in the foreground of four localized FRBs, whose estimated cosmic dispersion measure $\mathrm{DM}_{\mathrm{cosmic}}^{\mathrm{est}}$ significantly exceeds the average at z_{FRB}. Implementing the methodology detailed in Section 5.3, we estimated the DM contribution of foreground galactic and group halos, $\mathrm{DM}_{\mathrm{halos}}$, as summarized in Table 5.3. For two fields, we found a high incidence of halos at close impact parameters to the sightline, such that the $\mathrm{DM}_{\mathrm{halos}}$ estimate matches or exceeds the average cosmic expectation value, $\langle \mathrm{DM}_{\mathrm{halos}} \rangle$. For the other two fields, the $\mathrm{DM}_{\mathrm{halos}}$ estimate is less than $5\,\mathrm{pc\,cm^{-3}}$ owing to the absence of foreground halos near the sightline. Our results reinforce the paradigm that FRBs can effectively probe foreground matter overdensities. That being said, one must exercise caution in accounting for plasma in the host galaxy and immediate FRB progenitor environment when studying matter distribution along the sightline. Combined with Simha et al. (2020) we conclude FRBs with apparent high $\mathrm{DM}_{\mathrm{cosmic}}$ arise from both higher than average foreground structure and inferred higher host contributions, with nearly equal probability.

Thus the FLIMFLAM survey is ramping up efforts towards data collection and analysis. Future results are expected to lay robust constraints on the parameters describing foreground matter distributions as well as constrain $\mathrm{DM}_{\mathrm{host}}$ statistically.

Acknowledgements

We thank Elmo Tempel for kindly providing his group-finding software, and Chris Lidman for assistance with the OzDES data reduction pipeline for AAOmega. Authors S.S., J.X.P., and N.T., as members of the Fast and Fortunate for FRB Follow-up team, acknowledge support from NSF grants AST-1911140, AST-1910471 and AST-2206490. N.T. and L.B. acknowledge support by FONDECYT grant 11191217. We acknowledge generous financial support from Kavli IPMU that made FLIMFLAM possible. Kavli IPMU is supported by World Premier International Research Center Initiative (WPI), MEXT, Japan. Based on data acquired at the Anglo-Australian Telescope, under programs A/2020B/04, A/2021A/13, and O/2021A/3001. We acknowledge the traditional custodians of the land on which the AAT stands, the Gamilaraay people, and pay our respects to elders past and present.

Table 5.3: Summary of DM contributions along the excess DM sightlines

FRB	Redshift	$\langle \mathrm{DM_{halos}} \rangle$ $\mathrm{pc\,cm^{-3}}$	$\mathrm{DM_{halos}}$ $\mathrm{pc\,cm^{-3}}$	$\sigma(\mathrm{DM_{halos}})$ $\mathrm{pc\,cm^{-3}}$	$\mathrm{DM^{est}_{cosmic}}$ $\mathrm{pc\,cm^{-3}}$	$\mathrm{DM^{model}_{cosmic}}$ $\mathrm{pc\,cm^{-3}}$	$\sigma(\mathrm{DM^{model}_{cosmic}})$ $\mathrm{pc\,cm^{-3}}$
FRB20190714A	0.2365	92	195	47	275	312	53
FRB20200430A	0.1610	63	66	19	152	144	24
FRB20200906A	0.3688	142	3	4	366	193	38
FRB20210117A	0.2145	83	3	4	502	108	21

Chapter 6

FLIMFLAM and Beyond

6.1 Motivation for FLIMFLAM

In the previous chapters, I have described the framework for FRBs to probe the gas within intervening halos and the diffuse IGM. In short, a foreground spectroscopic survey is required to identify intervening halos and determine the underlying density field from a cosmic-web reconstruction. One can model the gas within halos and the cosmic web filaments contributing to an FRB dispersion measure. However, key model parameters are poorly constrained. Chiefly,

1. $f_{\rm gas}$: the baryon fraction retained by halos after being subject to galactic feedback processes. [1]

2. $f_{\rm igm}$: the baryon fraction of the universe within the cosmic web filaments of IGM.

Single sightlines cannot constrain the two free model parameters simultaneously. Furthermore, estimating $\rm DM_{host}$ for any given sightline is difficult. In a

[1] This was referred to as $f_{\rm hot}$ in the previous chapters, but here I use the notation from (Lee et al., 2022) and subsequent FLIMFLAM collaboration papers.

sister publication of Simha et al. (2020, i.e., Chapter 2), (Chittidi et al., 2021) describe the observational effort required to model the host galaxy ISM contribution for FRB20190608B. Often, the error ellipse of the FRB is comparable to the host galaxy size in optical bands, which implies a high degree of uncertainty in any empirical $\mathrm{DM_{host}}$ estimation. A statistical analysis of several sightlines is required to constrain the above-mentioned model parameters and to treat $\mathrm{DM_{host}}$ systematically.

Thus motivated, as mentioned previously in Chapter 5, the **F**RB **L**ine-of-Sight **I**onization **M**easurement with **F**oreground **L**ightcone **A**AOmega **M**apping (FLIMFLAM) survey was conceived to constrain the baryon fractions within halos and the IGM respectively. In this chapter, I shall first describe the survey and our results from the first data release (henceforth: FFDR1). The text in the following sections is partially extracted from the works of Khrykin et al. (2024b) and Huang et al. 2024 (in prep), which I have co-authored. Subsequently, I shall describe the prospects for similar analysis in the era of deeper wide-field spectroscopic surveys such as DESI and 4MOST and the upcoming large sample of FRBs with arcsecond or better localization from several radio experiments, chiefly CHIME/FRB.

6.2 Observations

6.2.1 FRB sightlines

FRB	R.A. (deg)	Decl. (deg)	Redshift	Wide-field data	Narrow-field data	DM_{FRB} (pc cm^{-3})	Ref.
20211127A	199.8088	−18.8381	0.0469	6dF	AAT	234.83	Deller et al. (in prep)
20211212A	157.3507	+01.3605	0.0713	SDSS	AAT	206.00	Deller et al. (in prep)
20190608A	334.0199	−07.8982	0.1178	SDSS, 6dF	SDSS, KCWI, MUSE	339.50	Macquart et al. (2020)
20200430A	229.7066	+12.3761	0.1608	SDSS, AAT	LRIS, DEIMOS, MUSE	380.10	Heintz et al. (2020)
20191001A	323.3516	−54.7477	0.2340	AAT	AAT, MUSE, GMOS-S	506.92	Bhandari et al. (2020)
20190714A	183.9795	−13.0207	0.2365	AAT	LRIS, DEIMOS, MUSE	504.70	Heintz et al. (2020)
20180924B	326.1052	−40.9000	0.3212	AAT	AAT, MUSE	362.40	Bannister et al. (2019)
20200906A	053.4956	−14.0833	0.3688	AAT	LRIS, DEIMOS, MUSE	577.80	Bhandari et al. (2020)

Table 6.1: List of FRBs in the FLIMFLAM Data Release 1 as used in this work. From left to right the columns show: the ID of a given FRB, right ascension and declination in equatorial J2000 coordinates, spectroscopic redshift, survey or instrument used to acquire wide and narrow-field spectroscopic foreground distribution of galaxies, and overall observed DM_{FRB}, as well as the references for these estimates.

We selected FRB sightlines to include within the FLIMFLAM survey based on the following criteria:

1. localized to a host galaxy with high **Probabilistic Association of Transients to their Hosts (PATH)** posterior probability ($P(O|x) > 0.95$; c.f. Aggarwal et al. 2021);

2. located in regions of the sky with relatively low dust extinction ($E_{\mathrm{B-V}} \lesssim 0.06$); and

3. not believed to have a very large ($\gg 100$ pc cm^{-3}) host contribution to the FRB DM (e.g. Simha et al. 2023; Lee et al. 2023). The FRB 20210117A sightline was excluded based on this criteria as its host galaxy is estimated to contribute ~ 600 pc cm^{-3} in the rest frame. However, this was not known a priori and was only discovered after the analysis. Thus, data was still collected for this field.

Our FRBs are derived from the Commensal Real-time ASKAP Fast Transients (CRAFT) Survey conducted on the Australian Square Kilometre Array Pathfinder (ASKAP) radio telescope. These were then followed up with optical facilities by both the CRAFT and the Fast and Fortunate for FRB Follow-up (F^4) collaborations[2] to identify the host galaxies and their redshift. At the time of observation (2020-2022) for FFDR1, these sightlines listed in Table 6.1 represented the majority of known localized FRBs that fulfilled the criteria above.

[2]https://sites.google.com/ucolick.org/f-4

6.2.2 Survey design and data acquisition

Fig. 6.1 illustrates the survey, as designed by (Lee et al., 2022), consisting of three sub-components: wide-field, narrow-field, and integral field unit (IFU) spectroscopy. Here, I summarize the details of target selection and observations from Huang et al. 2024 (in prep.). First, we collect all available photometry from public catalogs for sources within a 1.2 deg radius of an FRB sightline. Our sources include: Pan-STARRS (Kaiser et al., 2010), DES (Abbott et al., 2018), DECaLS (Dey et al., 2019), NSC (Nidever et al., 2021), WISE (Wright et al., 2010) and VISTA (Arnaboldi et al., 2007). Targets for spectroscopic follow-up are selected from these catalogs.

The "wide" survey targets $r \lesssim 20$ foreground objects within the 1.05° radius field-of-view (FoV) of the AAT/AAOmega fiber-fed spectrograph (Smith et al., 2004) combined with the 2dF fiber positioning system (Lewis et al., 2002). Where available, we augmented our wide field data with publicly available spectroscopy from the Sloan Digital Sky Survey (SDSS; Almeida et al., 2023) and the 6-degree Field (6dF; Jones et al., 2009) spectroscopic surveys.

The narrow-field observations utilized AAT/AAOmega ($r \lesssim 21.5$ within 2.5 arcmin), the Low-Resolution Imaging Spectrograph (LRIS; Rockosi et al., 2010; Kassis et al., 2022) and the DEep Imaging Multi-Object Spectrograph (DEIMOS; Faber et al., 2003) at the W. M. Keck Observatory for targets visible from Mauna Kea. For southern fields, the Gemini Multi-Object Spectrograph (GMOS; Hook et al., 2004) at the Gemini South Telescope was used. Keck and Gemini observations were performed using slitmasks to obtain multiple spectra efficiently. For the Keck and Gemini targets, color cuts were applied to select $z \lesssim 0.5$ sources preferentially.

Finally, the IFU observations were conducted through the Multi-Unit Spectroscopic Explorer (MUSE; Bacon et al., 2010b) at the Very Large Telescope (VLT) and the Keck Cosmic Web Imager (KCWI; Morrissey et al., 2018b) at Keck to target fainter $r \lesssim 23$, nearby (within $1'$) galaxies. Including low redshift ($z \lesssim 0.1$) sightlines that have foreground spectroscopic coverage in existing surveys, the final data release shall contain ~ 20 sightlines.

The raw data from each instrument is reduced using their respective pipelines: 2dfdr (AAO software team, 2015) for AAOmega, PypeIt (Prochaska et al., 2020) for DEIMOS, LRIS and GMOS, EsoReflex with Zap for MUSE (Freudling et al., 2013), and KCWIDRP for KCWI data cubes (Morrissey et al., 2018a). Each pipeline produces raw 1D spectra, which are subsequently fed into the MARZ redshifting package (Hinton et al., 2016) for redshift estimation. MARZ cross correlates the input spectra with templates and automatically estimates the redshift corresponding to the highest cross-correlation value among all template spectra. MARZ then assigns a redshift quality flag (QOP) value between 1 and 4 for the galaxies, with 3 and 4 being secure redshift estimates. Stars are assigned QOP 6. All redshifts are manually vetted by at least two members of the FLIMFLAM team.

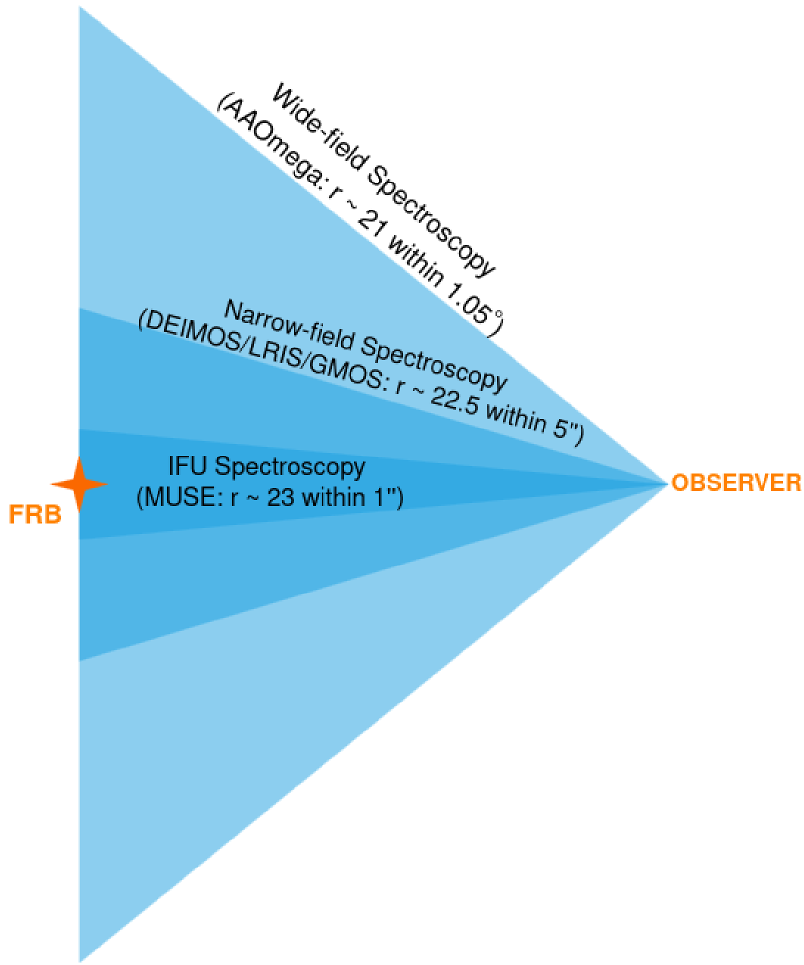

Figure 6.1: The FLIMFLAM survey design. The wide-field spectroscopy is conducted with the AAT/AAOmega, while the narrow-field observations are conducted with the Keck/DEIMOS and Gemini/GMOS. The IFU observations are conducted with the VLT/MUSE and Keck/KCWI.

6.3 DM Modeling

Having obtained the redshifts, we model the net DM contributions from the foreground halos and the cosmic web. For each FRB i:

$$\mathrm{DM}_{\mathrm{model},i} = \mathrm{DM}_{\mathrm{MW},i} + \mathrm{DM}_{\mathrm{igm,i}} + \mathrm{DM}_{\mathrm{halos,i}} + \mathrm{DM}_{\mathrm{host},i}, \tag{6.1}$$

Here, I refer the reader to Section 5.2.1 in Chapter 5 for modeling the Milky Way and halo contribution. Next, the host galaxy contribution is modeled as two subcomponents:

$$\mathrm{DM}_{\mathrm{host},i} = \frac{\mathrm{DM}^{unk}_{\mathrm{host},i} + \mathrm{DM}^{halo}_{\mathrm{host},i}}{1 + z_{\mathrm{FRB}}} \tag{6.2}$$

The first component, $\mathrm{DM}^{unk}_{\mathrm{host},i}$ represents the DM contribution from the host ISM and the progenitor environment in its rest frame. As this cannot be estimated from our data, we allow this to be a free parameter within our model. The remainder, $\mathrm{DM}^{halo}_{\mathrm{host},i}$ is the DM contribution from the host halo, which is modeled the same way as other intervening halos with the exception that the FRB is assumed to originate from the center. Hence, only half the halo is intersected. Thus, we compute the halo DM from our model, assuming an impact parameter of 0 kpc and dividing by 2.

To estimate $\mathrm{DM}_{\mathrm{halos,i}}$, we follow the same framework described in section 5.3 of Chapter 5. However, for the FLIMFLAM analysis, we allow $f_{\mathrm{gas}}$to vary as a free parameter.

$\mathrm{DM}_{\mathrm{igm,i}}$ is estimated from a foreground cosmic web map. In Chapter 2, we used the MCPM algorithm to reconstruct the cosmic web filaments along the FRB sightline. For FLIMFLAM, however, we use the ARGO framework instead. As I shall describe below, ARGO is a Bayesian density estimator that offers the advantage of generating multiple realizations of dark matter density consistent with the observed spatial distribution of foreground galaxies. This allows us to determine the uncertainty in the cosmic web density along the FRB sightline. The `ARGO` numerical algorithm (Ata et al., 2015, 2017), is based on works by Kitaura & Enßlin (2008), Jasche et al. (2010), and Kitaura et al. (2010). In what follows, we outline the main properties of the `ARGO` reconstructions used in this work and refer the reader to a more detailed description given in the manuscripts above, as well as the work of Lee et al. (2022), where the multi-tracer extension is described.

6.3.1 Density Reconstruction and $\mathrm{DM}_{\mathrm{IGM}}$ Estimation

`ARGO` is a fully Bayesian inference algorithm that applies a Hybrid Monte Carlo technique (HMC; Duane et al., 1987; Neal, 2011) to reconstruct the evolved cosmic matter density fields given the observed redshift-space distribution of galaxies on the light-cone. Once the galaxy survey selection functions and galaxy bias are considered, the code depends only on the assumed cosmological and structure formation models. In addition, our version of `ARGO` adopts a prescription from Ata et al. (2021) that allows combining information from multiple individual spectroscopic surveys.

Before running `ARGO`, first, for a given FRB field, we set up a rectangular comoving reconstruction volume with cell sizes of $1.875\,h^{-1}$ Mpc, where the X axis is aligned with the line-of-sight direction to the FRB. Each volume contains $N_{\mathrm{y}} = N_{\mathrm{z}} = 100$ cells along the Y and Z axes, respectively, representing the dimensions perpendicular to the line-of-sight. Our fields are narrow enough that we can adopt the flat-sky approximation and assume that the plane of the sky is always perpendicular to the line of sight. The number of cells along the X-axis is adjusted depending on the comoving distance between the observer and an FRB, given by

$$d_{\mathrm{com}} = \frac{c}{H_0} \int_0^{z_{\mathrm{spec}}} \frac{\mathrm{d}z}{\sqrt{\Omega_{\mathrm{M}}\,(1+z)^3 + \Omega_\lambda}}. \tag{6.3}$$

Similar to Lee et al. (2022), we exclude the first 50 h^{-1}Mpc along the X-axis direction due to decreased ARGO performance at nearby comoving distances, where the lightcone distribution of galaxies becomes very narrow, and the reconstructions would be noisy. For the first $50\,h^{-1}$ Mpc of the path, we apply the mean cosmic $\langle \mathrm{DM_{IGM}} \rangle$ value. In addition, we extend the X-axis beyond the line-of-sight position of a given FRB to avoid any potential boundary effects in the reconstructions near the FRB location.

To simplify the $\mathrm{DM_{igm}}$ estimation at later stages of our analysis, the center of the coordinate system of the ARGO volume is chosen in such a way that an FRB is located at Cartesian coordinates $p = \{\mathrm{X_{frb}}, \mathrm{Y} = 0, \mathrm{Z} = 0\}$. To place an FRB at these coordinates, we need to adopt a transformation between the on-sky and the corresponding Cartesian coordinates provided by

$$\mathrm{X} = d_{\mathrm{com}} \cos\alpha \cos\delta,$$

$$\mathrm{Y} = d_{\mathrm{com}} \sin\alpha \cos\delta,$$

$$\mathrm{Z} = d_{\mathrm{com}} \sin\delta,$$

where $\alpha,\ \delta$ are the right ascension and declination coordinates of the FRB, and d_{com} is given by Equation 6.3. However, the FRB coordinate vector is not yet aligned with the above coordinate system of the ARGO volume. Thus, we further estimate the rotation matrix used to rotate the observed FRB frame to the correct ARGO coordinate system.

6.3.1.1 ARGO inputs

ARGO is fed the catalog of halos: 3D locations in the coordinate system previously described and the halo masses. We include galaxy and group/cluster halos in our catalog as described in section 5.3 of Chapter 5. In addition, `ARGO` is fed the angular and radial selection functions (ASF/RSF) of the various wide-field surveys, listed in Table 6.1. These are measures of survey completeness as a function of angular position on the sky and redshift, respectively. It is crucial to incorporate this information to accurately determine, e.g., whether a given underdensity of galaxies within the survey volume is due to a cosmic void or lack of observations within that region.

For the FRB fields that contain SDSS survey data, we follow the strategy outlined in Ata et al. (2021) and extract the ASF in the 10×10 deg^2 region around the position of the FRB from the publicly available `MANGLE` outputs[3] (Hamilton & Tegmark, 2004; Swanson et al., 2008). For the FRB fields containing 6dF survey data, we apply the ASF estimation algorithm in Ata et al. (2021) by comparing the final 6dF DR3 galaxy catalog (Jones et al., 2009) with the map of 6dF on-sky pointings and stellar masks (communicated privately), again over a 10×10 deg^2 field around the FRB. Similarly, the ASF of the AAT survey data is calculated by comparing the number of galaxies with good-quality redshifts to the lists of the selected targets for AAOmega observations combined with the corresponding stellar masks.

Finally, to estimate the RSF in each field, we compute the distribution of observed galaxies in the `ARGO` reconstruction volumes as a function of comoving distance from the observer, in bins of 10 h^{-1} Mpc.

[3]https://space.mit.edu/~molly/mangle/download/data.html

6.3.1.2 From ARGO reconstructions to $\mathrm{DM_{IGM}}$

Fig. 6.2 shows a set of dark matter overdensity δ_m fields rendered by ARGO within the 3D grids covering the foregrounds of each FRB. We follow the steps below to convert the sightline overdensity fields to estimates of $\mathrm{DM_{IGM}}$.

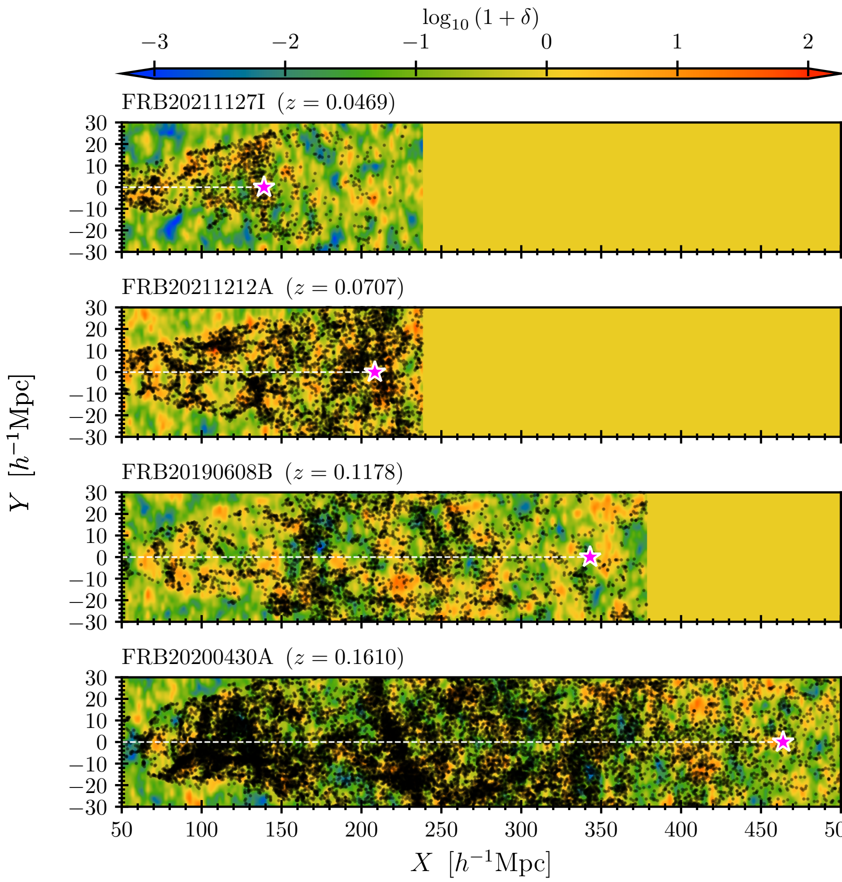

Figure 6.2: An example of the ARGO reconstructions for four FRB fields in the FLIMFLAM DR1 sample. The black points represent the locations of individual foreground galaxies, and the background color scale represents the reconstructed dark matter overdensity. *Image credit: Khrykin et al. (2024b)*

The equation defining $\mathrm{DM_{IGM}}$ is:

$$\mathrm{DM_{IGM}} = \int \frac{n_{e,\mathrm{igm}}(s)}{1+z(s)} \mathrm{d}s, \tag{6.4}$$

Where $n_{e,\mathrm{igm}}$ is the number density of free electrons in the IGM along the sightline. For each FRB field in our sample, we estimate $\mathrm{DM_{IGM}}$ directly from the `ARGO` density reconstructions, adopting the discretized version of Equation (6.4) as follows:

$$\mathrm{DM_{IGM}^{argo}} = \bar{n}_{e,\mathrm{bar}}\left(\bar{z}\right) \sum_{s} \left(1 + \delta_{m,s}^{\mathrm{sm}}\right) l_s \left(1 + z_s\right)^{-1}, \tag{6.5}$$

where l_s is the path length to the cell s of the `ARGO` reconstruction volume along the FRB line-of-sight, z_s is the corresponding redshift of the cell, $\delta_{m,s}^{\mathrm{sm}}$ is the smoothed matter overdensity (Fig. 6.2). The smoothing length is $R = 0.7\,h^{-1}\,\mathrm{Mpc}$, which was found by Lee et al. (2022) to allow dark matter-only N-body simulations with $1.875\,h^{-1}\,\mathrm{Mpc}$ grid cells to match the global $\mathrm{DM_{IGM}}$ distribution in cosmological hydrodynamical simulations. We define $\bar{n}_{e,\mathrm{bar}}\left(\bar{z}\right)$ as the mean cosmic density of electrons at the median redshift $\bar{z}$ traversed by the ensemble of FRB paths, defined as:

$$\bar{n}_{e,\mathrm{bar}}\left(\bar{z}\right) = \Omega_b \bar{\rho}_c\left(\bar{z}\right) \left[\frac{m_{\mathrm{He}}\left(1-Y\right) + 2Y m_{\mathrm{H}}}{m_{\mathrm{He}} m_{\mathrm{H}}}\right], \tag{6.6}$$

where m_{H} and m_{He} are the atomic masses of hydrogen and helium atoms, respectively; $Y_{\mathrm{He}} = 0.243$ is the cosmic mass fraction of doubly ionized helium, $\Omega_b = 0.044$ is the cosmic baryon density, and $\bar{\rho}_c\left(\bar{z}\right)$ is the critical density of the Universe. As written, $\bar{n}_{e,\mathrm{bar}}$ assumes that all baryons in the Universe are ionized and reside in the IGM. We can further introduce f_{igm}, the fraction of all cosmic baryons residing in the IGM, which will be one of the free parameters in our analysis. Thus,

$$\bar{n}_{e,\mathrm{igm}} \equiv f_{\mathrm{igm}}\, \bar{n}_{e,\mathrm{bar}} \tag{6.7}$$

is the actual mean number density of free electrons in the IGM as constrained by our data. To tie together Equations 6.4, 6.5, 6.6, and 6.7 with the current limited data set, we will constrain $f_{\rm igm}$ as a free parameter assuming a fixed redshift of $\bar{z} \simeq 0.20$ which is approximately the median redshift probed by the DR1 FRB sightlines. Finally, the median $\rm DM_{igm,i}$ from all the `ARGO` realizations is chosen as the best model estimate for the IGM contribution for each field.

6.4 Parameter inference and results from FFDR1

Combining the various DM components from the previous section, we now have a model of the FRB DM for each sightline. The model has three free parameters: $f_{\rm gas}$, $f_{\rm igm}$, and $\mathrm{DM}^{unk}_{{\rm host},i}$. The sightlines are jointly analyzed using a Bayesian MCMC framework.

6.4.1 Likelihood and Priors

We assume that the joint likelihood function $\mathcal{L}_{\rm frb}\left(\mathrm{DM}_{\rm frb}|\Theta\right)$ for 8 FRBs in our sample (see Table 6.1) is well-described by a Gaussian

$$\ln \mathcal{L}\left(\mathrm{DM}_{\rm frb}|\Theta\right) \propto -\frac{1}{2}\sum_{i}^{N_{\rm frb}}\left[\frac{\left(\mathrm{DM}_{{\rm model},i}\left(\Theta\right)-\mathrm{DM}_{{\rm frb},i}\right)^2}{\sigma_i^2}\right], \tag{6.8}$$

where $\Theta = \{f_{\rm igm}, f_{\rm gas}, \langle \mathrm{DM}^{unk}_{{\rm host},i}\rangle\}$ represents our model parameters, $\mathrm{DM}_{{\rm model},i}$ is the model dispersion measure, described in details in the previous section, and the model variance σ_i^2 is estimated by combining in quadrature uncertainties on the individual components of the total $\mathrm{DM}_{{\rm model},i}$, given by

$$\sigma_i^2 = \left(\sigma_{\mathrm{igm},i}^{\mathrm{argo}}\right)^2 + \left(\sigma_{\mathrm{halos},i}\right)^2 + \left(\sigma_{\mathrm{host}}^{\mathrm{unk}}\right)^2 + \left(\sigma_{\mathrm{host},i}^{\mathrm{halo}}\right)^2 + \left(\sigma_{\mathrm{MW},i}\right)^2, \tag{6.9}$$

we omit the uncertainty on the observed $\mathrm{DM_{FRB}}$ because it is negligible compared to other considered uncertainties. For a given value of $\langle \mathrm{DM}_{\mathrm{host}}^{\mathrm{unk}} \rangle$, we assume a log-normal distribution such that the corresponding variance $(\sigma_{\mathrm{host}}^{\mathrm{unk}})^2$ is described by

$$\left(\sigma_{\mathrm{host}}^{\mathrm{unk}}\right)^2 = \left(e^{\sigma_*^2} - 1\right) e^{\left(2\mu + \sigma_*^2\right)}, \tag{6.10}$$

where $\mu \equiv \langle \mathrm{DM}_{\mathrm{host},i}^{unk} \rangle$, and we use the best-fit value $\sigma_* = 1.23$ from James et al. (2022a)[4]

(Khrykin et al., 2024b) describe four priors used for the parameter inference. Here, I shall only describe the results from using the fiducial priors:

1. A flat prior on f_{igm}, i.e. $\pi(f_{\mathrm{igm}}) = [0.0, 1.0)$.

2. A flat prior on the logarithm of $\mathrm{DM}_{\mathrm{host},i}^{unk}$, i.e. $\pi(\log(\mathrm{DM}_{\mathrm{host},i}^{unk})) = [0.0, 6.0)$. This is consistent with previous analysis by James et al. (2022a).

3. A flat prior in f_{gas}, i.e. $\pi(f_{\mathrm{gas}}) = [0.0, 1.0)$.

An additional prior is placed on the universe's baryon fraction of diffuse gas, f_d. f_d was originally defined in eqn. 1.4. In the context of the model parameters, f_d is a function of $f_{\mathrm{igm}}$and f_{gas}:

$$f_d = f_{\mathrm{igm}} + f_{\mathrm{cgm}} + f_{\mathrm{icm}} \tag{6.11}$$

[4] James et al. (2022a) reported the standard deviation of the log-normal $\mathrm{DM_{host}}$ distribution in $\log_{10}$ units ($\sigma = 0.53$). We rescaled it by a factor of $1/\log_{10} e$ in order to convert to the natural logarithm units.

Here, f_{icm} is the baryon fraction within the intra-cluster medium (ICM) of massive halos $M_{\mathrm{halo}} > 10^{14}\mathrm{M}_{\odot}$ while f_{cgm} is the gas fraction within lower mass halos. Both are functions of f_{gas} and are pre-computed for our MCMC sampling by integrating halo gas mass for the Aemulus halo mass function (McClintock et al., 2019) over their respective mass ranges. For the ICM, a fixed value of $f_{\mathrm{gas,ICM}}$=0.8 is chosen, consistent with current measurements within clusters (Gonzalez et al., 2013; Chiu et al., 2018).

6.4.2 Results

The posterior probability distributions of the model parameters were estimated using the `emcee` MCMC sampler (Foreman-Mackey et al., 2013). For the fiducial priors, the best-fit parameter estimates and the 1σ errors are:

$$
\begin{aligned}
f_{\mathrm{igm}} &= 0.59^{+0.11}_{-0.10}, \\
f_{\mathrm{gas}} &= 0.55^{+0.26}_{-0.29}, \\
\mathrm{DM}^{unk}_{\mathrm{host},i} &= 69^{+28}_{-19}\ \mathrm{pc\,cm^{-3}}.
\end{aligned}
\tag{6.12}
$$

Fig. 6.3 visualizes the joint posterior distributions. As is evident from the distributions, our sample of FRBs has limited sensitivity to f_{gas} as the 95% confidence intervals cover the entire range of prior values allowed. Based on the most probable f_{gas}, we can use the previously computed lookup table for f_{cgm} and estimate that the baryon fraction within galaxy and group halos is $f_{\mathrm{cgm}} = 0.20^{+0.10}_{-0.11}$.

Based on the $\mathrm{DM}^{unk}_{\mathrm{host},i}$ estimate, we can infer the mean $\mathrm{DM}_{\mathrm{host}}$ for the FRBs in our sample by adding the average halo DM of the host galaxies to $\mathrm{DM}^{unk}_{\mathrm{host},i}$. We estimate $\langle \mathrm{DM}_{\mathrm{host}} \rangle = 90\mathrm{pc\,cm^{-3}}$ with comparable uncertainties. Our mean value is lower than the estimates from James et al. (2022a); Baptista et al. (2023) ($135 \pm 50 \mathrm{pc\,cm^{-3}}$) although still consistent within their uncertainty limits. It must be noted that, unlike the aforementioned works, we excluded FRBs with large host DMs within our sample, and thus, we believe our $\mathrm{DM_{host}}$ values are therefore skewed lower. Finally, our f_{igm} estimate is consistent with the values obtained by Khrykin et al. (2024a) from simulating various feedback scenarios in the `SIMBA` cosmological hydrodynamical simulations (Davé et al., 2019). While we cannot rule out any model of feedback based on our initial results, we look to our second data release with $\sim$ 20 sightlines to produce more stringent constraints.

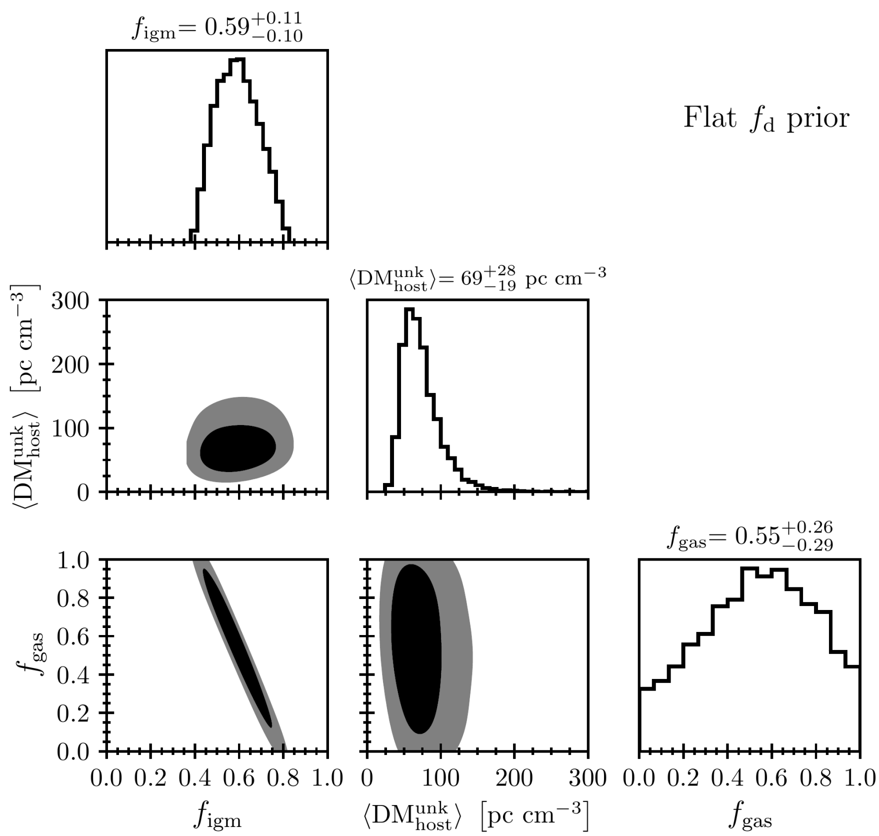

Figure 6.3: The joint posterior distributions of the model parameters using the fiducial 'flat f_d prior.' The dark contours are 68% confidence intervals, and the lighter regions correspond to 95%. *Image credit: Khrykin et al. (2024b)*

6.5 FLIMFLAM in the era of large spectroscopic surveys

Our results from FFDR1 demonstrate the potential of FRBs to constrain the distribution of baryons within the universe. As of the writing of this manuscript, several FRB detection experiments are underway worldwide, which will result in a sharp increase in FRB localization rates. For example, the Canadian Hydrogen Intensity Mapping Experiment (CHIME) is building outrigger antennas to perform very long baseline interferometry spanning almost the entire North American continent. Lanman et al. (2024) already report the successful localization of pulsars to a few arcseconds with their first outrigger scope. The full system will produce 1-3 sub-second localizations daily (internal comm.). The Australian Square Kilometre Array Pathfinder (ASKAP) has upgraded their hardware backend and will produce several FRB localizations weekly (a.k.a. the CRACO upgrade; internal comm.). Several other FRB localization experiments are online or will be operating soon (e.g., MeerTRAP, DSA-110, RealFAST, BURSTT). Within the next few years, we expect to have a sample of hundreds of FRBs with arcsecond or better localizations and host redshifts. This represents a substantially larger sample of sightlines to work with and expand the statistical power and scope of the FLIMFLAM-style cosmic baryon analysis.

However, to leverage as many sightlines in the FLIMFLAM framework, one needs a sizeable spectroscopic follow-up campaign that covers a significant fraction of the sky, e.g. $\sim 30\%$ of 4π steradians. Fortunately, several wide-field spectroscopic surveys are also in progress, chief among which is the Dark Energy Spectroscopic Instrument (DESI) Survey (DESI Collaboration et al., 2016). DESI is a 5-year survey aiming to obtain optical spectra of millions of galaxies and quasars. The survey is expected to cover 14,000 square degrees of the sky and provide redshifts for galaxies up to $z \sim 1.5$. Specifically, its Bright Galaxy Survey (BGS) sample of galaxies will be a magnitude-limited ($r < 19.5$) catalog of redshifts with $> 80\%$ fiber assignment efficiency and $> 95\%$ redshift success rate (Hahn et al., 2023) and thus provides the ideal substitute for the FLIMFLAM AAT spectroscopic campaign. The first DESI data release (DESI DR1) is anticipated in 2025, with its footprint overlapping significantly with CHIME. Indeed, roughly 55% of all ~ 500 FRBs in the CHIME/FRB catalog (CHIME/FRB Collaboration et al., 2021) within the imaging footprint of DESI. This convergence of wide-field spectroscopic surveys and large-scale FRB localizations presents a unique opportunity to study the cosmic baryon distribution.

I use mock lightcone catalogs in the following sections to perform a Fisher matrix forecast of the FLIMFLAM analysis in the DESI era with ~ 300 sightlines.

6.5.1 Mock FRB and foreground catalogs

For the mock FRB and foreground galaxy sample, I shall use the semi-analytic lightcone catalogs employed by Lee et al. (2022) from (Henriques et al., 2015) based on the Millenium N-body Cosmological Simulations (Springel, 2005). The observations are simulated using 24 of the 1 degree radius lightcones that contain galaxies up to $z = 1.2$ with halo masses $> 10^{10}\mathrm{M}_{\odot}$. Lee et al. (2022) further provide `ARGO` reconstructions for the complete volumes of 6 of the 24 lightcones. Using the mock FRBs from these 6, I sample the $\mathrm{DM}_{\mathrm{IGM}}$ distribution as a function of the FRB redshift. Then, I estimate the distribution of $\mathrm{DM}_{\mathrm{IGM}}$ vs. z using the `scipy` implementation of the Gaussian kernel density estimator (KDE). From this distribution, I can generate estimates of $\mathrm{DM_{IGM}}$ for any FRB in the remaining 18 lightcones without `ARGO` reconstructions. FRB hosts are selected randomly by choosing a halo with mass $> 3 \times 10^{10} \mathrm{M}_\odot$ at $0.05 < z < 0.25$ [5] from one of the 24 lightcones. Each host is at least 1.2 arcmin away from other simulated hosts to minimize any correlations between sightlines.

6.5.2 Model parameters

The greater sample size ~ 300 sightlines is conducive to more sophisticated modeling of the baryon distribution along FRB sightlines. For instance, one can leverage the larger sample to constrain gas within halos of various mass bins separately. In FFDR1 f_{gas} for group and clusters halos, $f_{\mathrm{gas,ICM}}$ is fixed at 0.8. However, we can explore allowing this parameter to vary freely in the DESI era. More generally, f_{gas} can be an independent variable for any number of mass bins or a parametric function of halo mass. Here, I explore the scenario of allowing independent f_{gas} values for three halo mass bins: galaxies ($M_{\mathrm{halo}} < 10^{13} \mathrm{M}_\odot$), galaxy groups ($10^{13} < M_{\mathrm{halo}} < 10^{14} \mathrm{M}_\odot$) and galaxy clusters $M_{\mathrm{halo}} > 10^{14} \mathrm{M}_\odot$.

6.5.3 Fisher matrix forecast

The Fisher matrix is computed for a given model prediction $F(\Theta)$ where Θ is the vector of model parameters, e.g. $\{\theta_1, \theta_2, \theta_3 ...\}$. For FLIMFLAM, F_i is the prediction for the extragalactic DM of the i^{th} FRB, i.e., $\mathrm{DM_{model,i}} = \mathrm{DM_{halos,i}} + \mathrm{DM_{igm,i}} + \mathrm{DM}^{unk}_{\mathrm{host},i}/(1 + z_i)$ for an ensemble of FRBs and the full Fisher matrix is the sum of the

[5] 0.25 is the median redshift of the BGS sample as verified by the DESI survey validation observations, i.e., the one-percent survey. See Hahn et al. (2023) for further details.

individual matrices $\Sigma_i F_i$. The Fisher matrix is defined as:

$$F_{jk} = \sum_{i=1}^{N_{\rm FRB}} \frac{\partial F_i}{\partial \theta_j} \frac{\partial F_i}{\partial \theta_k} \frac{1}{\sigma_i^2} \tag{6.13}$$

where

$$\sigma_i^2 = \left(\sigma_{{\rm igm},i}^{\rm argo}\right)^2 + \left(\sigma_{{\rm halos},i}\right)^2 + \left(\sigma_{\rm host}^{\rm unk}\right)^2 \tag{6.14}$$

is the variance of the model prediction for the i^{th} FRB. The Fisher matrix is then inverted to obtain the covariance matrix of the model parameters. Here, the host halo DM is subsumed into $\mathrm{DM}_{\rm halos,i}$. There are 5 model parameters, i.e. $\Theta = \{f_{\rm gas,gal}, f_{\rm gas,grp}, f_{\rm gas,clu}, f_{\rm igm}, \langle \mathrm{DM}_{{\rm host},i}^{unk} \rangle\}$. The partial derivatives are calculated as follows:

$$\begin{aligned} \frac{\partial F_i}{\partial f_{\rm gas,X}} &= \frac{\partial \mathrm{DM}_{\rm halos,i}}{\partial f_{\rm gas,X}} = \mathrm{DM}_{\rm halos,i}(f_{\rm gas,X} = 1); \mathrm{for} X \in \{\mathrm{gal,grp,clu}\} \\ \frac{\partial F_i}{\partial f_{\rm igm}} &= \frac{\partial \mathrm{DM}_{\rm igm,i}}{\partial f_{\rm igm}} = \mathrm{DM}_{\rm halos,i}(f_{\rm igm} = 1) \\ \frac{\partial F_i}{\partial \langle \mathrm{DM}_{{\rm host},i}^{unk} \rangle} &= \frac{1}{(1+z_i)} \end{aligned} \tag{6.15}$$

$\partial F_i / \partial f_{\rm gas,X}$ are computed within the mass ranges of each X; e.g., galaxy halos do not contribute to the derivative for cluster or group gas fraction. I use the same modified NFW profile for the halo DM as in FFDR1, and the IGM uncertainties are based on 10 `ARGO` reconstructions. The Fisher matrix is computed for 312 FRB sightlines [6]. Unifrm flat priors are chosen for all model parameters with the following ranges: $f_{\rm gas,X} \in [0.0, 1.0]\ \forall X \in \{gal, grp, clu\}$, $f_{\rm igm} \in [0.0, 1.0]$, $\langle \mathrm{DM}_{{\rm host},i}^{unk} \rangle \in [0, 200]$. With uniform priors, the resulting posteriors are independent constraints on the partition of

[6] a multiple of the 24 (lightcones).

baryons in the universe. The true value of each parameter is set as follows: $f_{\rm gas,gal} = 0.2$, $f_{\rm gas,grp} = 0.4$, $f_{\rm gas,clu} = 0.6$, $f_{\rm igm} = 0.8$, $\langle {\rm DM}^{unk}_{{\rm host},i} \rangle = 100 {\rm pc\,cm^{-3}}$.

Fig. 6.4 visualizes the final covariance matrix for the five model parameters computed from the Fisher forecast analysis. Firstly, $f_{\rm igm}$ is very well-constrained with $\sim 5\%$ relative uncertainty. This alone can provide a powerful constraint on the feedback processes within galaxies as investigated by Khrykin et al. (2024a). Indeed, it can be used to discern between the fiducial SIMBA simulations and a scenario where AGN feedback is turned off. Furthermore, different simulations predict a different halo mass dependence of $f_{\rm gas}$ and thus, an extended FLIMFLAM analysis further reinforces the distinction between AGN and stellar feedback models.

6.6 Thesis summary and conclusions

In the last six years, I have witnessed the rapid development of the study of FRBs, from their first localizations to distant galaxies to their use as powerful cosmological probes of ionized matter and the cosmic baryon distribution. In this thesis, I have presented work I have led or contributed substantially to FRB as cosmological probes.

1. Chapter 2 describes the work I led on the first end-to-end analysis of the FRB20190608A sightline to predict the FRB DM through foreground optical observations. This established the spectroscopic analysis framework for the analysis of the cosmic baryon distribution. The cosmic DM along the sightline was modeled as contributions from individual halos and the diffuse IGM. The IGM gas was reconstructed using galaxy redshifts and masses.

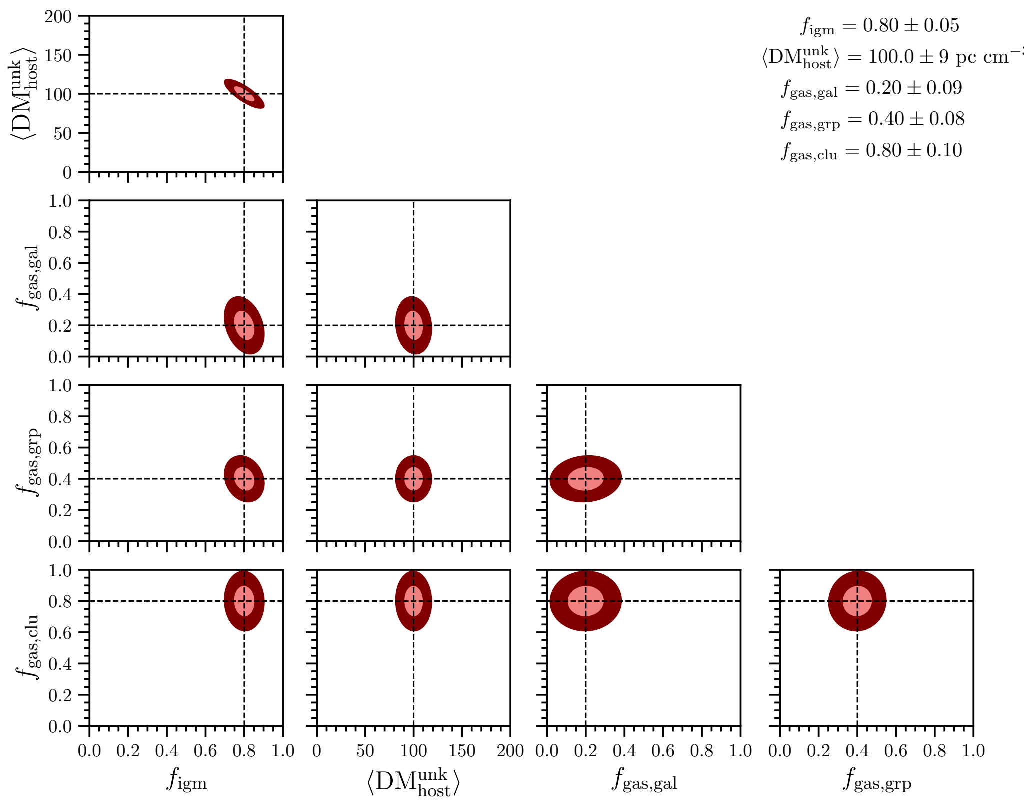

Figure 6.4: The Fisher matrix forecast for the extended set of model parameters as with 312 FRB sightlines. The individual parameter constraints are shown in the top left above the corner plot.

2. Chapter 3 describes an extension to the analysis above with photometric redshifts and provides a method to place reasonable constraints on $\mathrm{DM}_{\mathrm{halos}}$ in the case of limited spectroscopic data.

3. Chapter 4 describes instrumentation work I performed for LRIS on the Keck I telescope. The upgraded detector system was subsequently used for multi-object spectroscopy of foreground galaxies along FRB sightlines.

4. Chapter 5 describes the analysis of $\mathrm{DM}_{\mathrm{halos}}$ using the foreground spectroscopic data along sightlines with excess $\mathrm{DM}_{\mathrm{cosmic}}$ compared to the average. This study established that the foreground structure along the sightlines could account for the excess in half the sample. At the same time, the other half showed clear evidence of the excess in the host galaxy/progenitor environment. Along with work by Lee et al. (2023); Connor et al. (2023), this result added to the sample of excess DM FRB sightlines. It showed that the majority (5/7 at the time of the abovementioned results) of such sightlines show foreground DM excess as opposed to the host.

5. Finally, chapter 6 describes the FLIMFLAM survey, which represents a comprehensive analysis of the distribution of baryons in the universe using several FRB sightlines. The survey extends the analysis from Chapter 2 in fitting for the baryons fractions in halos and the IGM as independent parameters to produce the first direct constraints on these previously unknown quantities. I forecast the results of such an analysis in the era of large-scale spectroscopic surveys and show that they imply powerful constraints on galactic feedback models. These results

are expected within the next three years and will form the basis of my work as a postdoctoral researcher.

In the distant future, it is unclear what direction the field of FRBs as cosmological probes will take. However, I am confident that they will continue to provide unique constraints on the ionized baryons in the universe. With several thousand FRBs, one can conceivably constrain halo radial gas profile shape parameters (e.g., the mass-dependence of halo concentration; see Shao et al., 2023) with a FLIMFLAM-like analysis. FRBs can yield new constraints in conjunction with other probes of matter, such as X-ray emission from hot gas, the Sunyayev-Zeldovich effect, and quasar absorption lines. For instance, combining the radial pressure profile of clusters from the SZ-effect with density profiles from FRBs can produce temperature profiles in cluster halos and thus inform models of shock heating as diffuse gas from cosmic web filaments accretes onto clusters (see Fujita et al., 2017).

I look forward to the future of FRB cosmology and am excited to be at its forefront.

Bibliography

AAO software team. 2015, 2dfdr: Data reduction software, Astrophysics Source Code Library, record ascl:1505.015

Abbott, T. M. C., Abdalla, F. B., Allam, S., et al. 2018, ApJS, 239, 18, doi: 10.3847/1538-4365/aae9f0

Aggarwal, K., Budavári, T., Deller, A. T., et al. 2021, ApJ, 911, 95, doi: 10.3847/1538-4357/abe8d2

Almeida, A., Anderson, S. F., Argudo-Fernández, M., et al. 2023, ApJS, 267, 44, doi: 10.3847/1538-4365/acda98

Arnaboldi, M., Neeser, M. J., Parker, L. C., et al. 2007, The Messenger, 127, 28

Ata, M., Kitaura, F.-S., Lee, K.-G., et al. 2021, MNRAS, 500, 3194, doi: 10.1093/mnras/staa3318

Ata, M., Kitaura, F.-S., & Müller, V. 2015, MNRAS, 446, 4250, doi: 10.1093/mnras/stu2347

Ata, M., Kitaura, F.-S., Chuang, C.-H., et al. 2017, MNRAS, 467, 3993, doi: 10.1093/mnras/stx178

Ayromlou, M., Nelson, D., & Pillepich, A. 2022, arXiv e-prints, arXiv:2211.07659, doi: 10.48550/arXiv.2211.07659

Bacon, R., Accardo, M., Adjali, L., et al. 2010a, in Ground-based and Airborne Instrumentation for Astronomy III, ed. I. S. McLean, S. K. Ramsay, & H. Takami, Vol. 7735, International Society for Optics and Photonics (SPIE), 773508, doi: 10.1117/12.856027

Bacon, R., Accardo, M., Adjali, L., et al. 2010b, in Ground-based and Airborne Instrumentation for Astronomy III, ed. I. S. McLean, S. K. Ramsay, & H. Takami, Vol. 7735, International Society for Optics and Photonics (SPIE), 773508, doi: 10.1117/12.856027

Bahcall, J. N., & Spitzer, Lyman, J. 1969, ApJL, 156, L63, doi: 10.1086/180350

Bannister, K. W., Deller, A. T., Phillips, C., et al. 2019, Science, 365, 565, doi: 10.1126/science.aaw5903

Baptista, J., Prochaska, J. X., Mannings, A. G., et al. 2023, arXiv e-prints, arXiv:2305.07022, doi: 10.48550/arXiv.2305.07022

Barbary, K. 2016, Journal of Open Source Software, 1, 58, doi: 10.21105/joss.00058

Basu, A., & Roy, S. 2013, MNRAS, 433, 1675, doi: 10.1093/mnras/stt845

Behroozi, P. S., Conroy, C., & Wechsler, R. H. 2010, ApJ, 717, 379, doi: 10.1088/0004-637X/717/1/379

Behroozi, P. S., Wechsler, R. H., & Wu, H.-Y. 2013, ApJ, 762, 109, doi: 10.1088/0004-637X/762/2/109

Bennett, C. L., Larson, D., Weiland, J. L., et al. 2013, ApJS, 208, 20, doi: 10.1088/0067-0049/208/2/20

Bertin, E., & Arnouts, S. 1996, A&AS, 117, 393, doi: 10.1051/aas:1996164

Bhandari, S., Bannister, K. W., James, C. W., et al. 2019, MNRAS, 486, 70, doi: 10.1093/mnras/stz804

Bhandari, S., Sadler, E. M., Prochaska, J. X., et al. 2020, ApJL, 895, L37, doi: 10.3847/2041-8213/ab672e

Bhandari, S., Heintz, K. E., Aggarwal, K., et al. 2022, AJ, 163, 69, doi: 10.3847/1538-3881/ac3aec

Bhandari, S., Gordon, A. C., Scott, D. R., et al. 2023, ApJ, 948, 67, doi: 10.3847/1538-4357/acc178

Bhardwaj, M., Kirichenko, A. Y., Michilli, D., et al. 2021, ApJL, 919, L24, doi: 10.3847/2041-8213/ac223b

Boquien, M., Burgarella, D., Roehlly, Y., et al. 2018, VizieR Online Data Catalog, J/A+A/622/A103

Brammer, G. B., van Dokkum, P. G., & Coppi, P. 2008, ApJ, 686, 1503, doi: 10.1086/591786

Bruzual, G., & Charlot, S. 2003, MNRAS, 344, 1000, doi: 10.1046/j.1365-8711.2003.06897.x

Bryan, G. L., & Norman, M. L. 1998, ApJ, 495, 80, doi: 10.1086/305262

Burchett, J. N., Elek, O., Tejos, N., et al. 2020, ApJL, 891, L35, doi: 10.3847/2041-8213/ab700c

Burchett, J. N., Tripp, T. M., Prochaska, J. X., et al. 2019, ApJL, 877, L20, doi: 10.3847/2041-8213/ab1f7f

Calzetti, D. 2001, PASP, 113, 1449, doi: 10.1086/324269

Cantalupo, S., Pezzulli, G., Lilly, S. J., et al. 2019, MNRAS, 483, 5188, doi: 10.1093/mnras/sty3481

Cappellari, M. 2017, MNRAS, 466, 798, doi: 10.1093/mnras/stw3020

Cen, R., & Ostriker, J. P. 1999, ApJ, 514, 1, doi: 10.1086/306949

—. 2006, ApJ, 650, 560, doi: 10.1086/506505

Chabrier, G. 2003, PASP, 115, 763, doi: 10.1086/376392

Chatterjee, S., Law, C. J., Wharton, R. S., et al. 2017, Nature, 541, 58, doi: 10.1038/nature20797

Chen, H.-W., & Tinker, J. L. 2008, ApJ, 687, 745, doi: 10.1086/591927

Childress, M. J., Lidman, C., Davis, T. M., et al. 2017, Monthly Notices of the Royal Astronomical Society, 472, 273, doi: 10.1093/mnras/stx1872

CHIME/FRB Collaboration, Amiri, M., Andersen, B. C., et al. 2021, ApJS, 257, 59, doi: 10.3847/1538-4365/ac33ab

Chittidi, J. S., Simha, S., Mannings, A., et al. 2020, arXiv e-prints, arXiv:2005.13158. https://arxiv.org/abs/2005.13158

—. 2021, ApJ, 922, 173, doi: 10.3847/1538-4357/ac2818

Chiu, I., Mohr, J. J., McDonald, M., et al. 2018, MNRAS, 478, 3072, doi: 10.1093/mnras/sty1284

Cole, S., Lacey, C. G., Baugh, C. M., & Frenk, C. S. 2000, MNRAS, 319, 168, doi: 10.1046/j.1365-8711.2000.03879.x

Connor, L., & Ravi, V. 2022, Nature Astronomy, 6, 1035, doi: 10.1038/s41550-022-01719-7

Connor, L., Ravi, V., Catha, M., et al. 2023, ApJL, 949, L26, doi: 10.3847/2041-8213/acd3ea

Cook, A. M., Bhardwaj, M., Gaensler, B. M., et al. 2023, ApJ, in press

Cordes, J. M., & Lazio, T. J. W. 2003a, ArXiv Astrophysics e-prints

—. 2003b, ArXiv Astrophysics e-prints

Dale, D. A., Helou, G., Magdis, G. E., et al. 2014, ApJ, 784, 83, doi: 10.1088/0004-637X/784/1/83

Das, S., Mathur, S., Gupta, A., Nicastro, F., & Krongold, Y. 2021, MNRAS, 500, 655, doi: 10.1093/mnras/staa3299

Davé, R., Anglés-Alcázar, D., Narayanan, D., et al. 2019, MNRAS, 486, 2827, doi: 10.1093/mnras/stz937

Davé, R., Cen, R., Ostriker, J. P., et al. 2001, ApJ, 552, 473, doi: 10.1086/320548

Day, C. K., Deller, A. T., Shannon, R. M., et al. 2020, MNRAS, 497, 3335, doi: 10.1093/mnras/staa2138

de Graaff, A., Cai, Y.-C., Heymans, C., & Peacock, J. A. 2019, A&A, 624, A48, doi: 10.1051/0004-6361/201935159

Deng, W., & Zhang, B. 2014a, ApJL, 783, L35, doi: 10.1088/2041-8205/783/2/L35

—. 2014b, ApJL, 783, L35, doi: 10.1088/2041-8205/783/2/L35

DESI Collaboration, Aghamousa, A., Aguilar, J., et al. 2016, arXiv e-prints, arXiv:1611.00036, doi: 10.48550/arXiv.1611.00036

Dey, A., Schlegel, D. J., Lang, D., et al. 2019, AJ, 157, 168, doi: 10.3847/1538-3881/ab089d

Duane, S., Kennedy, A. D., Pendleton, B. J., & Roweth, D. 1987, Physics Letters B, 195, 216, doi: 10.1016/0370-2693(87)91197-X

Eckert, D., Jauzac, M., Shan, H., et al. 2015, Nature, 528, 105, doi: 10.1038/nature16058

Elek, O., Burchett, J. N., Prochaska, J. X., & Forbes, A. G. 2021, TVCG, 27. https://github.com/CreativeCodingLab/Polyphorm

Faber, S. M., Phillips, A. C., Kibrick, R. I., et al. 2003, in Society of Photo-Optical Instrumentation Engineers (SPIE) Conference Series, Vol. 4841, Instrument Design and Performance for Optical/Infrared Ground-based Telescopes, ed. M. Iye & A. F. M. Moorwood, 1657–1669, doi: 10.1117/12.460346

Fan, X., Carilli, C. L., & Keating, B. 2006, ARA&A, 44, 415, doi: 10.1146/annurev.astro.44.051905.092514

Foreman-Mackey, D., Hogg, D. W., Lang, D., & Goodman, J. 2013, PASP, 125, 306, doi: 10.1086/670067

Freudling, W., Romaniello, M., Bramich, D. M., et al. 2013, A&A, 559, A96, doi: 10.1051/0004-6361/201322494

Fujita, Y., Akahori, T., Umetsu, K., Sarazin, C. L., & Wong, K.-W. 2017, ApJ, 834, 13, doi: 10.3847/1538-4357/834/1/13

Fukugita, M. 2004, Symposium - International Astronomical Union, 220, 227–232, doi: 10.1017/S0074180900183287

Fukugita, M., Hogan, C. J., & Peebles, P. J. E. 1998, ApJ, 503, 518, doi: 10.1086/306025

Gaia Collaboration, Brown, A. G. A., Vallenari, A., et al. 2020, arXiv e-prints, arXiv:2012.01533. https://arxiv.org/abs/2012.01533

Gaia Collaboration, Prusti, T., de Bruijne, J. H. J., et al. 2016, A&A, 595, A1, doi: 10.1051/0004-6361/201629272

Gonzalez, A. H., Sivanandam, S., Zabludoff, A. I., & Zaritsky, D. 2013, ApJ, 778, 14, doi: 10.1088/0004-637X/778/1/14

Gordon, A. C., Fong, W.-f., Kilpatrick, C. D., et al. 2023, arXiv e-prints, arXiv:2302.05465. https://arxiv.org/abs/2302.05465

Hahn, C., Wilson, M. J., Ruiz-Macias, O., et al. 2023, AJ, 165, 253, doi: 10.3847/1538-3881/accff8

Hamilton, A. J. S., & Tegmark, M. 2004, MNRAS, 349, 115, doi: 10.1111/j.1365-2966.2004.07490.x

Heintz, K. E., Prochaska, J. X., Simha, S., et al. 2020, ApJ, 903, 152, doi: 10.3847/1538-4357/abb6fb

Henley, D. B., & Shelton, R. L. 2013, ApJ, 773, 92, doi: 10.1088/0004-637X/773/2/92

Henriques, B. M. B., White, S. D. M., Thomas, P. A., et al. 2015, MNRAS, 451, 2663, doi: 10.1093/mnras/stv705

Hinshaw, G., Branday, A. J., Bennett, C. L., et al. 1996, ApJL, 464, L25, doi: 10.1086/310076

Hinton, S. R., Davis, T. M., Lidman, C., Glazebrook, K., & Lewis, G. F. 2016, Astronomy and Computing, 15, 61, doi: 10.1016/j.ascom.2016.03.001

Hook, I. M., Jørgensen, I., Allington-Smith, J. R., et al. 2004, PASP, 116, 425, doi: 10.1086/383624

Huchra, J. P., Macri, L. M., Masters, K. L., et al. 2012, ApJS, 199, 26, doi: 10.1088/0067-0049/199/2/26

Inoue, S. 2004, MNRAS, 348, 999, doi: 10.1111/j.1365-2966.2004.07359.x

James, C. W., Prochaska, J. X., Macquart, J. P., et al. 2022a, MNRAS, 509, 4775, doi: 10.1093/mnras/stab3051

James, C. W., Ghosh, E. M., Prochaska, J. X., et al. 2022b, arXiv e-prints, arXiv:2208.00819. https://arxiv.org/abs/2208.00819

Janesick, J. R. 2001, Scientific charge-coupled devices (SPIE Press)

Jasche, J., Kitaura, F. S., Li, C., & Enßlin, T. A. 2010, MNRAS, 409, 355, doi: 10.1111/j.1365-2966.2010.17313.x

Jones, D. H., Read, M. A., Saunders, W., et al. 2009, MNRAS, 399, 683, doi: 10.1111/j.1365-2966.2009.15338.x

Kaiser, N., Burgett, W., Chambers, K., et al. 2010, in Society of Photo-Optical Instrumentation Engineers (SPIE) Conference Series, Vol. 7733, Ground-based and Airborne Telescopes III, ed. L. M. Stepp, R. Gilmozzi, & H. J. Hall, 77330E, doi: 10.1117/12.859188

Karachentsev, I. D., Makarov, D. I., & Kaisina, E. I. 2013, AJ, 145, 101, doi: 10.1088/0004-6256/145/4/101

Kassis, M. F., Allen, S., Alvarez, C., et al. 2022, in Society of Photo-Optical Instrumentation Engineers (SPIE) Conference Series, Vol. 12184, Ground-based and Airborne Instrumentation for Astronomy IX, ed. C. J. Evans, J. J. Bryant, & K. Motohara, 1218405, doi: 10.1117/12.2628630

Kauffmann, G., White, S. D. M., & Guiderdoni, B. 1993, MNRAS, 264, 201, doi: 10.1093/mnras/264.1.201

Keating, L. C., & Pen, U.-L. 2020, MNRAS, 496, L106, doi: 10.1093/mnrasl/slaa095

Khrykin, I. S., Sorini, D., Lee, K.-G., & Davé, R. 2024a, MNRAS, 529, 537, doi: 10.1093/mnras/stae525

Khrykin, I. S., Ata, M., Lee, K.-G., et al. 2024b, arXiv e-prints, arXiv:2402.00505, doi: 10.48550/arXiv.2402.00505

Kitaura, F. S., & Enßlin, T. A. 2008, MNRAS, 389, 497, doi: 10.1111/j.1365-2966.2008.13341.x

Kitaura, F.-S., Jasche, J., & Metcalf, R. B. 2010, MNRAS, 403, 589, doi: 10.1111/j.1365-2966.2009.16163.x

Kuntz, K. D., & Snowden, S. L. 2000, ApJ, 543, 195, doi: 10.1086/317071

Lanman, A. E., Andrew, S., Lazda, M., et al. 2024, arXiv e-prints, arXiv:2402.07898, doi: 10.48550/arXiv.2402.07898

Law, C. J., Butler, B. J., Prochaska, J. X., et al. 2020, ApJ, 899, 161, doi: 10.3847/1538-4357/aba4ac

Lee, J., Shin, J., Snaith, O. N., et al. 2021, ApJ, 908, 11, doi: 10.3847/1538-4357/abd08b

Lee, K.-G., Ata, M., Khrykin, I. S., et al. 2022, ApJ, 928, 9, doi: 10.3847/1538-4357/ac4f62

Lee, K.-G., Khrykin, I. S., Simha, S., et al. 2023, ApJL, 954, L7, doi: 10.3847/2041-8213/acefb5

Lewis, I. J., Cannon, R. D., Taylor, K., et al. 2002, MNRAS, 333, 279, doi: 10.1046/j.1365-8711.2002.05333.x

Li, Y., Zhang, B., Nagamine, K., & Shi, J. 2019, ApJL, 884, L26, doi: 10.3847/2041-8213/ab3e41

Lim, S. H., Mo, H. J., Lu, Y., Wang, H., & Yang, X. 2017, MNRAS, 470, 2982, doi: 10.1093/mnras/stx1462

Lim, S. H., Mo, H. J., Wang, H., & Yang, X. 2020, ApJ, 889, 48, doi: 10.3847/1538-4357/ab63df

Lorimer, D. R., Bailes, M., McLaughlin, M. A., Narkevic, D. J., & Crawford, F. 2007, Science, 318, 777, doi: 10.1126/science.1147532

Macquart, J.-P., & Koay, J. Y. 2013, ApJ, 776, 125, doi: 10.1088/0004-637X/776/2/125

Macquart, J. P., Shannon, R. M., Bannister, K. W., et al. 2019, ApJL, 872, L19, doi: 10.3847/2041-8213/ab03d6

Macquart, J. P., Prochaska, J. X., McQuinn, M., et al. 2020, Nature, 581, 391, doi: 10.1038/s41586-020-2300-2

Madau, P., & Dickinson, M. 2014, ARA&A, 52, 415, doi: 10.1146/annurev-astro-081811-125615

Marnoch, L. 2023, ApJ, in prep

Martizzi, D., Vogelsberger, M., Artale, M. C., et al. 2019, MNRAS, 486, 3766, doi: 10.1093/mnras/stz1106

Mather, J. C., Cheng, E. S., Cottingham, D. A., et al. 1994, ApJ, 420, 439, doi: 10.1086/173574

McClintock, T., Rozo, E., Becker, M. R., et al. 2019, ApJ, 872, 53, doi: 10.3847/1538-4357/aaf568

McQuinn, M. 2014a, ApJL, 780, L33, doi: 10.1088/2041-8205/780/2/L33

—. 2014b, ApJL, 780, L33, doi: 10.1088/2041-8205/780/2/L33

McQuinn, M., Lidz, A., Zaldarriaga, M., et al. 2009, ApJ, 694, 842, doi: 10.1088/0004-637X/694/2/842

Morrissey, P., Matuszewski, M., Martin, D. C., et al. 2018a, ApJ, 864, 93, doi: 10.3847/1538-4357/aad597

—. 2018b, ApJ, 864, 93, doi: 10.3847/1538-4357/aad597

Moster, B. P., Naab, T., & White, S. D. M. 2013, MNRAS, 428, 3121, doi: 10.1093/mnras/sts261

Neal, R. 2011, in Handbook of Markov Chain Monte Carlo, 113–162, doi: 10.1201/b10905

Nevalainen, J., Tempel, E., Ahoranta, J., et al. 2019, A&A, 621, A88, doi: 10.1051/0004-6361/201833109

Nicastro, F. 2016, in XMM-Newton: The Next Decade, ed. J.-U. Ness, 27, doi: 10.48550/arXiv.1611.03722

Nicastro, F., Kaastra, J., Krongold, Y., et al. 2018, Nature, 558, 406, doi: 10.1038/s41586-018-0204-1

Nidever, D. L., Dey, A., Fasbender, K., et al. 2021, AJ, 161, 192, doi: 10.3847/1538-3881/abd6e1

Niu, C. H., Aggarwal, K., Li, D., et al. 2022, Nature, 606, 873, doi: 10.1038/s41586-022-04755-5

Noll, S., Burgarella, D., Giovannoli, E., et al. 2009, A&A, 507, 1793, doi: 10.1051/0004-6361/200912497

Petroff, E., Barr, E. D., Jameson, A., et al. 2016, PASA, 33, e045, doi: 10.1017/pasa.2016.35

Pillepich, A., Springel, V., Nelson, D., et al. 2018, MNRAS, 473, 4077, doi: 10.1093/mnras/stx2656

Planck Collaboration, Ade, P. A. R., Aghanim, N., et al. 2014, A&A, 571, A1, doi: 10.1051/0004-6361/201321529

—. 2016a, A&A, 594, A13, doi: 10.1051/0004-6361/201525830

Planck Collaboration, Aghanim, N., Arnaud, M., et al. 2016b, A&A, 594, A22, doi: 10.1051/0004-6361/201525826

Planck Collaboration, Aghanim, N., Akrami, Y., et al. 2020, A&A, 641, A6, doi: 10.1051/0004-6361/201833910

Prochaska, J., Hennawi, J., Westfall, K., et al. 2020, The Journal of Open Source Software, 5, 2308, doi: 10.21105/joss.02308

Prochaska, J. X., Weiner, B., Chen, H. W., Mulchaey, J., & Cooksey, K. 2011, ApJ, 740, 91, doi: 10.1088/0004-637X/740/2/91

Prochaska, J. X., & Zheng, Y. 2019, MNRAS, 485, 648, doi: 10.1093/mnras/stz261

Prochaska, J. X., Macquart, J.-P., McQuinn, M., et al. 2019, Science, 366, 231, doi: 10.1126/science.aay0073

Qiu, H., Bannister, K. W., Shannon, R. M., et al. 2019, MNRAS, 486, 166, doi: 10.1093/mnras/stz748

Rafiei-Ravandi, M., Smith, K. M., Li, D., et al. 2021, ApJ, 922, 42, doi: 10.3847/1538-4357/ac1dab

Ravi, V., Catha, M., Chen, G., et al. 2023, aas, in press

Rockosi, C., Stover, R., Kibrick, R., et al. 2010, in Ground-based and Airborne Instrumentation for Astronomy III, ed. I. S. McLean, S. K. Ramsay, & H. Takami, Vol.

7735, International Society for Optics and Photonics (SPIE), 77350R, doi: 10.1117/12.856818

Rykoff, E. S., Rozo, E., Busha, M. T., et al. 2014, ApJ, 785, 104, doi: 10.1088/0004-637X/785/2/104

Scholz, P., Spitler, L. G., Hessels, J. W. T., et al. 2016, ApJ, 833, 177, doi: 10.3847/1538-4357/833/2/177

Shao, M. J., Anbajagane, D., & Chang, C. 2023, MNRAS, 523, 3258, doi: 10.1093/mnras/stad1620

Shull, J. M., Smith, B. D., & Danforth, C. W. 2012, ApJ, 759, 23, doi: 10.1088/0004-637X/759/1/23

Simha, S., Burchett, J. N., Prochaska, J. X., et al. 2020, ApJ, 901, 134, doi: 10.3847/1538-4357/abafc3

Simha, S., Tejos, N., Prochaska, J. X., et al. 2021, ApJ, 921, 134, doi: 10.3847/1538-4357/ac2000

Simha, S., Lee, K.-G., Prochaska, J. X., et al. 2023, ApJ, 954, 71, doi: 10.3847/1538-4357/ace324

Smith, G. A., Saunders, W., Bridges, T., et al. 2004, in Society of Photo-Optical Instrumentation Engineers (SPIE) Conference Series, Vol. 5492, Ground-based Instrumentation for Astronomy, ed. A. F. M. Moorwood & M. Iye, 410–420, doi: 10.1117/12.551013

Somerville, R. S., & Primack, J. R. 1999, MNRAS, 310, 1087, doi: 10.1046/j.1365-8711.1999.03032.x

Sorini, D., Davé, R., Cui, W., & Appleby, S. 2022, MNRAS, 516, 883, doi: 10.1093/mnras/stac2214

Spitler, L. G., Cordes, J. M., Hessels, J. W. T., et al. 2014, ApJ, 790, 101, doi: 10.1088/0004-637X/790/2/101

Springel, V. 2005, MNRAS, 364, 1105, doi: 10.1111/j.1365-2966.2005.09655.x

Springel, V., Frenk, C. S., & White, S. D. M. 2006, Nature, 440, 1137, doi: 10.1038/nature04805

Springel, V., White, S. D. M., Jenkins, A., et al. 2005, Nature, 435, 629, doi: 10.1038/nature03597

Suresh, J., Bird, S., Vogelsberger, M., et al. 2015, MNRAS, 448, 895, doi: 10.1093/mnras/stu2762

Swanson, M. E. C., Tegmark, M., Hamilton, A. J. S., & Hill, J. C. 2008, MNRAS, 387, 1391, doi: 10.1111/j.1365-2966.2008.13296.x

Tacconi, L. J., Genzel, R., & Sternberg, A. 2020, arXiv e-prints, arXiv:2003.06245. https://arxiv.org/abs/2003.06245

Tago, E., Einasto, J., Saar, E., et al. 2008, A&A, 479, 927, doi: 10.1051/0004-6361:20078036

Tanimura, H., Aghanim, N., Kolodzig, A., Douspis, M., & Malavasi, N. 2020, A&A, 643, L2, doi: 10.1051/0004-6361/202038521

Tanimura, H., Hinshaw, G., McCarthy, I. G., et al. 2019, MNRAS, 483, 223, doi: 10.1093/mnras/sty3118

Tempel, E., Kipper, R., Saar, E., et al. 2014, A&A, 572, A8, doi: 10.1051/0004-6361/201424418

Tempel, E., Tago, E., & Liivamägi, L. J. 2012, A&A, 540, A106, doi: 10.1051/0004-6361/201118687

Tendulkar, S. P., Bassa, C. G., Cordes, J. M., et al. 2017, ApJL, 834, L7, doi: 10.3847/2041-8213/834/2/L7

Thornton, D., Stappers, B., Bailes, M., et al. 2013, Science, 341, 53, doi: 10.1126/science.1236789

Tumlinson, J., Thom, C., Werk, J. K., et al. 2013, ApJ, 777, 59, doi: 10.1088/0004-637X/777/1/59

Velliscig, M., Cacciato, M., Schaye, J., et al. 2015, MNRAS, 453, 721, doi: 10.1093/mnras/stv1690

Werk, J. K., Prochaska, J. X., Tumlinson, J., et al. 2014, ApJ, 792, 8, doi: 10.1088/0004-637X/792/1/8

Werner, N., Finoguenov, A., Kaastra, J. S., et al. 2008, A&A, 482, L29, doi: 10.1051/0004-6361:200809599

White, S. D. M., & Frenk, C. S. 1991, ApJ, 379, 52, doi: 10.1086/170483

White, S. D. M., & Rees, M. J. 1978, MNRAS, 183, 341, doi: 10.1093/mnras/183.3.341

Wilde, M. C., Werk, J. K., Burchett, J. N., et al. 2021, ApJ, 912, 9, doi: 10.3847/1538-4357/abea14

Wright, E. L., Eisenhardt, P. R. M., Mainzer, A. K., et al. 2010, AJ, 140, 1868, doi: 10.1088/0004-6256/140/6/1868

Wu, X., & McQuinn, M. 2023, ApJ, 945, 87, doi: 10.3847/1538-4357/acbc7d

Yang, X., Mo, H. J., van den Bosch, F. C., et al. 2007, ApJ, 671, 153, doi: 10.1086/522027

Yoshino, T., Mitsuda, K., Yamasaki, N. Y., et al. 2009, PASJ, 61, 805, doi: 10.1093/pasj/61.4.805

Yuan, F., Lidman, C., Davis, T. M., et al. 2015, Monthly Notices of the Royal Astronomical Society, 452, 3047, doi: 10.1093/mnras/stv1507